Ministero dell'Istruzione,
dell'Università e della Ricerca

UNIVERSITY OF SALERNO

Department of Civil Engineering

Research Doctorate
in
Risk and Sustainability
in Civil, Architectural and Environmental Engineering Systems

XXXIV Cycle (a.y. 2021-2022)

Monitoring freshwater environments by satellite data

Carmela Cavallo

Supervisor
Prof. Eng. Maria Nicolina Papa

Coordinator
Prof. Eng. Fernando Fraternali

PON
RICERCA
E INNOVAZIONE
2014 - 2020

UNIONE EUROPEA

Ministero dell'Università
e della Ricerca

This thesis was produced during the PhD in Risk and Sustainability in Civil, Architectural and Environmental Engineering Systems - XXXIV cycle, with the support of a scholarship funded with resources from the PON (National Operational Program) “Research and Innovation 2014-2020 - Innovative Doctorates with industrial characterization”.

To my father…

Contents

1. Introduction

Freshwater environments, despite covering only 0.08% of the Earth's surface and accounting for only 0.01% of all the water on our planet, are among the ecosystems with the highest density of animal and plant life. Unfortunately, they are some of the most threatened habitats in the world and are experiencing an unprecedented decline in biodiversity (IPBES 2019). More than 3000 species of freshwater fish are at risk of extinction immediately or in the near future, and for more than 80 species, it is now too late. Climate change, occurring on a global scale, together with human-induced impacts and pressures are the main causes of degradation, destruction and fragmentation of natural habitats. Although the biodiversity of freshwater environments is particularly threatened, investments in both research and conservation of freshwater biodiversity are far behind those of terrestrial and marine ecosystems (Aventino et al., 2021). The objectives set by 2020 to ensure the conservation, restoration and sustainable use of freshwater ecosystems have only been partially met and it is hoped that in the next decade the restoration measures will be such as to reverse the steep trends of loss of biodiversity.

The conservation and/or restoration of natural habitats are essential elements in preserving the biodiversity of a given area; it is by protecting natural environments that the conservation of living communities is guaranteed, preventing the extinction of different species. The availability of habitats in freshwater environments is closely linked to many aspects of river hydro-morphology such as the duration and extent of flooded areas, the presence and type of vegetation, the flow depth and velocity and their variability in time and space, the sediment type and mobility, the longitudinal, lateral and vertical connectivity etc. In river environments, hydro-morphological quality plays a central role in biological and physico-chemical quality, and habitat availability is closely influenced by the hydro-morphology of the river and its evolution over time. A river with a high hydro-morphological quality is able to provide habitats for different water-related species. This is one of the principles on which the requirements of the water framework directive (2000/60 CE) on the assessment of the ecological quality status of rivers are based. It is therefore clear that one of the elements on which to act to maintain biodiversity, and more generally the ecological quality of rivers, is to preserve or restore a good hydro-morphological quality. One of the fundamental elements is therefore the understanding of the cause and effect relationship between biological and hydro-morphological quality and the identification of the hydro-morphological aspects on which to act as a priority. As is well known, the understanding of the state and evolutionary trajectories of the hydro-morphology of a river is based primarily on continuous monitoring programs that are able to effectively and completely document the past evolutionary trends and present status.

Satellite data are powerful, cost-efficient and still under-exploited monitoring tools, that can be used to identify the hydro-morphological characteristics of rivers, monitor and track hydro-morphological evolution over time, and to quantify the duration and extent of flooded areas, at different spatial and temporal scales.

The main idea of the research work is to investigate how different kinds of satellite data can be exploited to achieve a better description of freshwater environments at adequate space scales and with high temporal resolution, with the aim of providing a key tool in the management and protection of freshwater ecosystems. For this reason, three different case studies were developed: wetland, reaches of a perennial river of the main network and reaches of non-perennial rivers of the minor network.

The first research question underlying this work was to understand whether, to what extent, and with what reliability medium-resolution multispectral satellite data can be used to describe the dynamics of water and vegetation in wetland environments. To do this a simple classification method was developed to monitor wetland land cover and therefore to map the temporal succession of flooding and drying and the vegetation dynamic. This knowledge is the basis for understanding the relationship between the dynamics of flooding, its duration, extent and spatial continuity and the availability of habitat. The selected study case was the wetland of Albufera in Spain that is one of the most important protected areas in Europe due to the presence of numerous species of migratory birds.

The second research question focused on the possibility of exploiting medium-resolution multispectral satellite data to monitor the evolution of river morphology over time. Wet channel dynamics over time and information on morphological changes occurred in the past were extracted. The satellite dataset used made it possible to extend the analysis to the last 35 years. The case study focused on two reaches of the Italian Po River.

The third research question is related to the possibility of using multispectral data from ESA's Sentinel-2 mission to characterize the hydrological regime of non-perennial rivers. An innovative tool was developed, capable of reconstructing the daily occurrence of different flow phases. The study cases were three rivers of Cilento National Park (South Italy).

This work is organized in five parts. In the first part, after a brief introduction of the advantages and problems associated with the various types of satellite sensors, the multispectral and Synthetic Aperture Radar (SAR) data used in this work are presented, detailing the main characteristics and the pre-processing chains that must be performed to make the data suitable for the observations. The second part offers an overview of the state of the art on the remote monitoring of wetlands and river environments.

The third part is dedicated to the application of multi-temporal data in the monitoring of the Albufera wetland in Spain. This study proposes a classification method for monitoring the wetland land cover as well as the temporal succession and spatial variation of flooding and drying. The fourth part deals with the exploiting multi-temporal data to monitor the hydro-morphological evolution of two reaches of the Italian Po River over a period of about 35 years. In this case study, the potential of satellite data in monitoring hydro-morphological changes before and after river restoration was also evaluated. Finally, the fifth part considers the challenging use, for the first time, of this type of data as a tool for monitoring the hydrological regime of non-perennial rivers.

2. Remote sensing datasets and processing

Remote sensing is a technical-scientific discipline that allows to identify, measure, and analyse the qualitative and quantitative characteristics of a specific object placed at a distance, based on electromagnetic energy measurements, emitted, reflected or diffused by the surface under examination. The data acquisition takes place thanks to remote sensors mounted on platforms, such as: drones, airplanes and satellites that allow to detect the electromagnetic energy coming from the scene in question and to convert it into information.

A significant advantage of satellite remote sensing, compared to other remote platforms, is the possibility to monitor wide areas with various spatial and temporal resolutions. Moreover, some satellite archives provide time series longer than 40 years. The longest global-coverage time series is provided by the Landsat program, that has been active since 1972, and the NOAA (National Oceanic and Atmospheric Administration) satellites, which acquired data from 1979 to 2019. The wide use of satellite data is also favoured by the free distribution policy adopted by some space agencies (e.g., the Copernicus program of the European Space Agency), as well as research and education programmes set up by private companies (e.g., Planet, Esri). Based on the functionality of the sensor used for the measurement of electromagnetic radiation, two main types of remote sensing are distinguished: active remote sensing and passive remote sensing.

Passive remote sensing makes use of passive sensors that detect the natural energy that can be emitted or reflected by the observed object. In passive remote sensing systems, the most common source of energy is the sun which irradiates the earth's surface with a continuous range of electromagnetic radiation. Sensors of this type by carrying out the measurement in different spectral channels centered on certain wavelengths of the electromagnetic spectrum. They range from the visible (0.4 µm - 0.7 µm) to the infrared (0.7 µm - 1 mm) and the thermal infrared (10.6 µm - 12.51 µm). The sensors that use this type of detection are, for example, the panchromatic (1 band), multispectral (10 bands) and hyperspectral (100 bands) sensors.

The main drawback of passive sensor is the inability to observe the Earth's surface in the presence of clouds; consequently, long periods without observation may occur in areas with frequent precipitation. On the other hand, however, in most cases, the optical data does not require long and complicated pre-processing steps. They are corrected radiometrically and geometrically by the various space agencies and can be used directly in the classification. The only pre-elaboration that in some cases must be carried out by the user is the atmospheric correction. Furthermore, by combining the red, green and blue (RGB) bands, it is possible to obtain true-colour images that can be easily interpreted even by non-expert users.

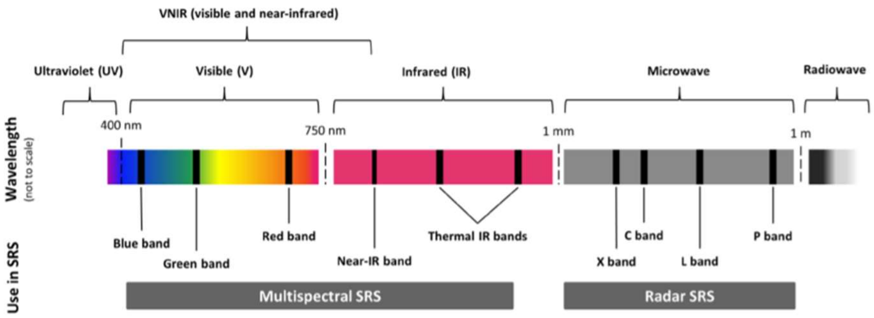

Figure 1: Electromagnetic spectrum and range of wavelengths used by the sensors. (Campbell 1996).

In active remote sensing, on the other hand, the sensor itself produces radiation to illuminate the scene and records the return signal. The most common active sensor is, for example, Synthetic Aperture Radar (SAR), which sends a beam of radiation, and records the return signal after it has interacted, and has therefore been modified, from the investigated surface. Radar sensors, including the SAR sensor, operate in the microwave part of the electromagnetic spectrum (1mm-10 cm, Figure 1), and have the advantage of operating at wavelengths unobstructed by cloud cover.

Furthermore, active sensors have the ability to operate both day and night. These peculiarities allow for high temporal frequencies of observations of the evolutionary dynamics. The weaknesses of SAR data are represented by the complexity of the data and, consequently, the difficulties related to the use of such data by non-expert users. The use of SAR sensors can be severely limited from the speckle effect (salt and pepper effect) making data interpretation difficult even after adequate filtering techniques.

In addition, SAR data can be influenced by geometric effects, such as layover and shadows (Gelautz et al., 1998), which occur mainly in mountainous areas.

SAR images contain two types of information: phase, which indicates the target sensor distance, and amplitude, which is the intensity of the signal reflected from the ground. Each cell in an image contains both quantities. The amplitude data are used to monitor changes in the various land cover classes over time; while the phase is the most important information for interferometric applications and is used to derive, through specific algorithms, ground displacements (e.g., monitoring of slow landslides).

The choice of the satellite data to be used, in a specific monitoring application, depends on many factors, such as: the object size (for example the length and width of the target river reach), the spatial resolution required, the physical properties of the objects to be observed, the duration of the observation period and the frequency with which changes need to be tracked (Legleiter and Fonstad 2012; Brierley and Fryirs 2013; Gilvear and Bryant 2016).

In general, spatial, temporal and spectral resolutions are in opposition to each other, data with coarse spatial resolution are available with high temporal resolution, and vice versa. For example, MODIS (Moderate Resolution Imaging Spectroradiometer) data have spatial resolution equal to 250 m and temporal resolution equal to 1 day, whereas very high-resolution images are available at irregular time intervals and with higher revisit times. Likewise, hyperspectral data are usually available at coarse resolutions. Therefore, the choice of the suitable satellite remote sensed datasets is challenging due to inevitable trade-offs between spatial resolution and return period.

Once the type of data has been identified, another key issue is the need to identify automatic procedures for retrieving useful information for monitoring purposes.

The following paragraphs present the satellite data employed in the study. A set of cloudless multispectral images acquired by passive sensors mounted on the Landsat-4/5, Landsat-8 and Sentinel-2 satellites and SAR images acquired by Sentinel-1 and Cosmo SkyMed satellites, were used. In addition, very high-resolution multispectral images (VHR) of the GeoEye-1 and WorldView-2 and 4 satellites were employed to validate the results obtained from the multispectral and SAR images at lower spatial resolutions. The choice was limited to free available satellite images on the Internet or distributed by space agencies following the approval of a research project. Among the freely available data, preference was given to data with the highest available spatial resolution.

After a short presentation of the satellite data used in the present work, a section related to the methods follows, in which the pre-processing operations and the spectral behaviour of the various ground covers will be presented in detail.

2.1 Mission and available datasets

2.1.1 Landsat missions

The Landsat program provides the most extended temporal series of the Earth’s land observations from satellites, from 1972 up to now (landsat.gsfc.nasa.gov, last accessed on 1st January 2022). For decades, Landsat data have been provided by the joint effort of the United States Geological Survey (USGS) and the National Aeronautics and Space Administration (NASA).

The first satellite launched into orbit on 23rd July 1972 under the name of ERTS1, "Earth Resources Technology Satellite", later renamed Landsat-1, represented the beginning of the era of Earth observation for non-military purposes. Since the launch of the first satellite, there have been a further seven successful missions that have contributed to an unprecedented 49-year record of Earth observation. Table 1 provides a summary of the Landsat missions since 1972 to now.

Table 1: List and main characteristics of the Landsat missions.

Missions	**Launch date**	**Satellite status**	**Sensors**	**Resolution [m]**
Landsat-1	23 July 1972	Mission Completed 1978	Return Beam Vidicon (RBV) and Multispectral Scanner System (MSS)	80
Landsat-2	22 January 1975	Mission Completed 1981	Return Beam Vidicon (RBV) and Multispectral Scanner System (MSS)	80
Landsat-3	5 March 1978	Mission Completed 1983	Return Beam Vidicon (RBV) and Multispectral Scanner System (MSS)	40 (RBV) 80 (MSS)
Landsat-4	16 July 1982	Mission Completed 1993	Multispectral Scanner System (MSS) and Thematic Mapper (TM)	80 (MSS) 30/120 (TM)
Landsat-5	1 March 1984	Mission Completed 2013	Multispectral Scanner System (MSS) and Thematic Mapper (TM)	80 (MSS) 30/120 (TM)
Landsat-6	5 October 1993	Failed to reach orbit	-	-
Landsat-7	15 April 1999	Operation despite Scan Line Corrector failure 31 May 2003	The Enhanced Thematic Mapper Plus (ETM+)	15/30/60
Landsat-8	11 Feb. 2013	Operation	Operational Land Imager (OLI) and the Thermal Infrared Sensor (TIRS)	15/30 (OLI) 100 (TIRS)
Landsat-9	27 Sep. 2021	Operating from 2022	Operational Land Imager-2 (OLI-2) and the Thermal Infrared Sensor-2 (TIRS-2)	15/30 (OLI-2) 100 (TIRS-2)

Currently two satellites are operational: Landsat-7 and Landsat-8, both equipped with technologically innovative sensors that have greatly expanded the detectable spectrum and spatial resolution bringing it to about 30 meters.

Unfortunately, the Landsat dataset is not continuous due to two events. The first event is linked to a failure in the instrumentation of the Scan Line Corrector mechanism (SLC) of the Enhanced Thematic Mapper Plus (ETM+) of the Landsat-7 satellite. Without an operating this sensor, the instrument's line of sight has a zig-zag trend along the satellite track and consequently the image area is doubled with an amplitude that increases when getting closer to the edges of the recorded scene. When the image acquired by the satellite, in the absence of the SLC sensor, is processed, a gap is left in the image represented by diagonal bands of black colour with a loss of information of the entire image around 22%. This renders the images acquired by the Landsat-7 satellite unusable. Secondly, the decommissioning of the Landsat-5 satellite before of the full operation of the Landsat-8 satellite resulted in a lack of data for the year 2012.

To date, the only satellite that is operational and capable of providing error-free images is the Landsat-8 satellite. In early 2022, images of the new Landsat-9 satellite, launched into orbit on 27th September 2021, will be publicly available from USGS. The Earth observation capabilities offered by the eight past, current and future Landsat missions have ensured and will ensure a consistency and continuity of measurements, with periodic incremental improvements that have increased and will increase the usefulness of the data for science and applications.

To exploit data with a spatial resolution of 30 m, in this thesis only multispectral images provided by the Landsat-4/5 and 8 missions were used, while the data provided by the Landsat-7 mission were not used for the reasons described above. Such missions, however, only the data from the Thematic Mapper (TM) and Operational Land Imager (OLI) sensors were used, capable of providing information on multiple bands of the electromagnetic spectrum. Landsat-4 (L4) and Landsat-5 (L5), both with the Multispectral Scanner (MSS) and the Thematic Mapper (TM)

Earth-imaging sensors on-board, were launched on 16th July 1982 and 1st March 1984, respectively. The TM sensor collected data in seven spectral bands, from the Visible (VIS), Near-Infrared (NIR), Shortwave Infrared (SWIR) and Thermal Infrared portions of the electromagnetic spectrum, with a moderate spatial resolution of 30 meters, except for the Thermal band, which has a spatial resolution of 120 m. To continue the collection, archiving and distribution of multispectral imagery, the Landsat Data Continuity Mission (LDCM)/Landsat-8 (L8) satellite was launched on 11st February 2013, with two instruments onboard: the Operational Land Imager (OLI) and the Thermal Infrared Sensor (TIRS), a two-channel thermal imager with a 100 m resolution. The Landsat-8 OLI sensor collects images data with a spatial resolution of 30 meters in the VIS, NIR, and SWIR wavelength and has a spatial resolution of 15 m for the panchromatic band. When working with multispectral data, it is essential to use surface reflectance products that provide an estimate of the spectral reflectance at ground level after radiometric and atmospheric correction. Therefore, The Landsat data exploited for the present research were Level-2 on-demand surface reflectance, freely downloaded from the USGS database (earthexplorer.usgs.gov, last accessed on 1st January 2022) of L4/5 (TM) and L8 (OLI) satellites. In absence of clouds, the L4/5 and L8 satellites have a temporal resolution of about 17 and 8 days, respectively.

2.1.2 Sentinel-2 mission

The Sentinel-2 (S2) mission is part of the Copernicus Earth Observation program led by the European Commission and operated by the European Space Agency (ESA). The S2 mission covers a field of view of 290 km and comprises a constellation of two polar-orbiting satellites placed in the same orbit. The first satellite, Sentinel-2A, launched on 23rd June 2015 provides images with a revisit time of approximately 10 days. Since the launch of the second satellite, Sentinel-2B, on 7th March 2017, the overall revisit time has become around 5 days. Both satellites are equipped with an opto-electronic Multispectral Instrument (MSI), which has provided moderate-resolution imagery since June 2015 (Sentinel-2A) and March

2017 (Sentinel-2B). The MSI provides 13 spectral bands from VIS, NIR to SWIR with four bands at 10 m, six bands at 20 m and three bands at 60 m spatial resolution. In detail, 10 m for the visible and the NIR bands (2,3,4,8), 20 m for the Red-Edge (RE), NIR and SWIR bands (5,6,7,8a,11,12), and 60 m for the atmospheric bands (1,9,10). S2 collection delivers Top-of-Atmosphere (TOA) reflectance (level-1C) products for data acquired before 2017 and Bottom-of-Atmosphere (BOA) reflectance images (level-2A) for data acquired after 2017. Therefore, it is necessary to correct the atmospheric effects on the S2 Level 1C images acquired before 2017 (see §2.2.2).

For the present study, the S2 satellite images were acquired from the ESA website (scihub.copernicus.eu, last accessed on 1st January 2022). In detail, level 1C (top of atmosphere reflectance - TOA) images were acquired before 2017 and the Level-2A (bottom of atmosphere reflectance - BOA) images for the remaining years.

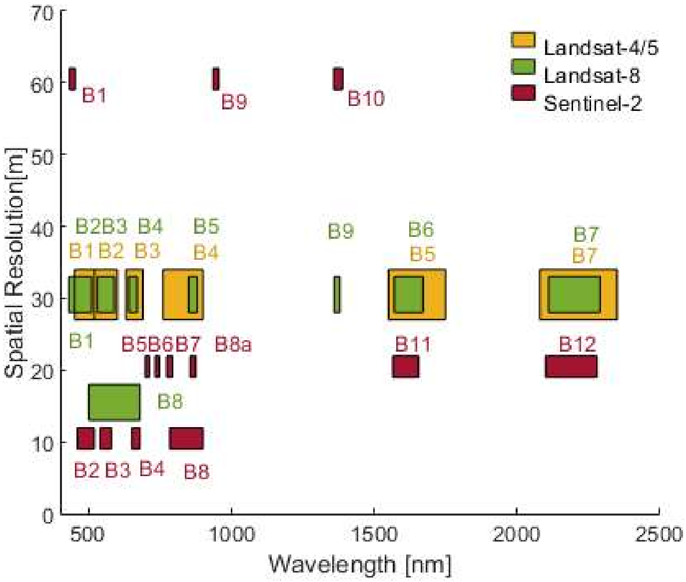

Figure 2: Spatial versus spectral resolution of the multispectral bands for the Landsat-4/5 TM, Landsat-8 OLI, Sentinel-2 MSI instruments.

Figure 2 shows the spatial and spectral resolutions of the multispectral bands (B1, B2, …., B12) of the three missions (Landsat-4/5-TM, Landsat-8-OLI, Sentinel-2-MSI) employed in this study. To make Figure 2 more readable, the Landsat bands in the Thermal wavelengths (10400 nm–12510 nm) were not reported. In this thesis, Sentinel-2 data were used for all the case studies (Chapters 4, 5 and 6), while Landsat-4/5 and 8 data were used to monitor the hydro-morphological changes of two reaches of the Italian Po River (Chapter 5) and Landsat 8 to monitor the Albufera wetland (Chapter 4).

2.1.3 Sentinel-1 SAR mission

Sentinel-1 is an ESA’s space mission within the Copernicus programme. The Sentinel-1 mission is a constellation of two polar-orbiting satellites, Sentinel-1A (launched on 3thApril 2014) and Sentinel-1B (launched on 25th April 2016) performing C-band synthetic aperture radar imaging. They allow for the acquisition of imagery regardless of the weather and illumination conditions with a revisit time of about 6 days. Sentinel-1's SAR instrument can acquire data in four modes: Stripmap Mode (SM), Interferometric Wide (IW), Extra Wide Swath (EW) and Wave (WV).

Stripmap mode is provided for continuity with European Remote Sensing and Envisat missions. Stripmap provides coverage with a resolution of 5m * 5m over an 80km swath of terrain. The IW mode is the main mode of land acquisition and meets most of the requirements of service. It acquires data with a swath of 250 km with a spatial resolution of 5 m* 20 m. EW is used for operational services in maritime, icy and polar areas where broad coverage and review times are required short. This acquisition mode scans images with a resolution of 20m * 40m. Finally, the Wave mode acquires data in 20 km * 20 km of vignettes, with a spatial resolution of 5 m*5 m, every 100 km along the orbit, acquired alternately on two different angles of incidence. The data are available in single polarization (VV or HH) for Wave mode, and double polarization (VV + VH or HH + HV) or single polarization (HH or VV) for Stripmap, Interferometric Wide and Extra Wide Swath modes. Each acquisition mode includes three processing levels: Level zero, Level 1 under two product types, Ground Range Detected (GRD) and Single Look Complex (SLC), and Level 2 Ocean data. Sentinel-1 Level 1 data is distributed free of charge from the Copernicus Open Access Hub (scihub.copernicus.eu, last accessed on 1st January 2022). A set of Sentinel-1 GRD level-1 images, with IW acquisition mode, in co-polarization VV and cross-polarization VH, was used for the Po River case study (§5.9).

2.1.4 Cosmo SkyMed SAR mission

Cosmo SkyMed is the Earth observation satellite programme developed by the Italian Space Agency (ASI) in collaboration with the Ministry of Defence and University and Scientific Research. COSMO-SkyMed provides global coverage of our planet operating in all weather and light conditions (day/night) and delivers high spatial resolution images with fast response times. The observation programme comprises a constellation of four identical satellites, equipped with X-band synthetic aperture radar (SAR). The first and second satellites of the COSMO-SkyMed constellation were launched on 7th June and 9th December 2007 (CSKS1, CSKS2). The third satellite was launched on 25th October 2008, and the last satellite was launched on 5th November 2010 (CSKS3, CSKS4). In recent years, the satellite mission has been further expanded with second-generation satellites. The first satellite of the COSMO-SkyMed Second Generation programme was launched on 18th December 2019 (CSGS1), while the second satellite was put into orbit on 31st January 2022 (CSGS2). Cosmo SkyMed can work by focusing on an area of a few square kilometres, obtaining images with a resolution of up to one metre (Spotlight images, 10 km * 10 km), or by observing areas of 40 km*40 km or 30 km*30km of the Earth's surface with approximately 3 m and 15 m of spatial resolution (StripMap Himages or StripMap pingPong), or by covering a region of 100 km or 200 km across, with 30 m and 100 m of spatial resolution (Scansar wide region and Scansar huge region images). Depending on the acquisition modes, the sensor acquires images in the signal polarisation between two of the possible ones i.e., VV, HH, HV and VH, and each image can be provided as a standard product. Standard products can include different in increasing order of processing levels (Level0, Level 1A,1B, 1C and 1D, Tepete et al., 2019). Cosmo images are not free of charge, but thanks to the "ASI Cosmo Open Call for science", it is possible to request images for research purposes. Once the project has been approved, the data can be accessed through the new COSMO-SkyMed portal (https://portal.cosmo-skymed.it/CDMFE/home, last accessed on 1st January 2022).

In this thesis, a set of COSMO-SkyMed stripmap images, level 1B, with 3 m resolution, 26.56° of incidence angle and HH polarization were used. One hundred COSMO-SkyMed observations of the scene were provided by the ASI within the framework of the “HABISAT- Habitat modelling in intermittent rivers by satellite data exploitation” project.

These data, thanks their high spatial resolution were used to monitor the hydrological phases in the non-perennial rivers (§ 6.9).

2.1.5 Very High-Resolution Images

In addition to the moderate spatial resolution (10-30 m) data provided by NASA/USGS and ESA, very high-resolution images (spatial resolution less than 1m) were employed as the ground-true condition for validating the various classification methods.

The very high-resolution images (VHR) of the Word-View-02/04 (WV-2, WV-4) and GeoEye-01 (GE-1) satellites and the images collection available on the Google Earth Pro platform were used.

The VHR images of WV-2, WV-4 and GE-1 satellites were provided by the European Space Agency (ESA) in the framework of the ESA third-party mission (© TPMO 2019) within the two projects: “Monitoring and modelling of surface water environments at large spatial and temporal scales by the integration of satellite remote sensing and local surveys” and “Tracking riverine morpho-dynamics from satellite imagery: the case of the Po River, Italy”. ESA’s third-party missions programme consists of about 50 satellite missions, which are owned by various organisations around the world. Thanks to agreements with these organizations, ESA can acquire, process and distribute data from their missions.

WV-2, WV-4 and GE-1 satellites are commercial Earth observation satellite owned by Digital Globe. The WV-2 and WV-4 satellites were launched on 8th October 2009 and 11st November 2016, respectively. The WV-2 satellite acquires data in nine spectral bands covering panchromatic, coastal, blue, green, yellow, red, red edge, NIR1, and NIR2, with a spatial resolution of 0.50 m for the panchromatic band and 2 m for the multispectral bands. The WV-4 satellite acquires five spectral bands covering the blue, green, red (VIS) and NIR bands at a resolution of 1.24 m and panchromatic images at a resolution of 0.31 m.

GE-1 satellites were launched on 6th September 2008, acquires VIS (blue, green, red) and NIR bands at 2 m and panchromatic images at 0.5 m. Details of all the bands provided by all the considered missions are given in Table 2. The data can be ordered in various optional formats: multispectral bands with standard spatial resolution, pan-sharpening of multispectral bands and bands bundle (Pan-sharpening + multispectral bands with standard spatial resolution). Pan-sharpening is a fusion technical in which the lower-resolution multiband dataset (2 m) is sharpened by the higher-resolution panchromatic image (0.30-0.50 m). To make the most of the information obtainable from a very high-resolution images, in this work the pan-sharpened of multispectral bands format, with a spatial resolution of about 0.50 m, were used to create RGB images.

Thanks to their very high spatial resolution, the RGB images created from the data provided by the WV-2/4 and GE-1 satellites and images collection available on the Google Earth Pro platform were used as a reference condition to validate the classification tools.

Table 2: Spectral coverage of the employed very high-resolution satellite data.

Bands [μm]	**WorldView-2**	**WorldView-4**	**GeoEye-1**
Coastal	0.40–0.45		
Blue	0.45–0.51	0.45−0.51	0.45–0.51

Green	0.51–0.58	0.51−0.58	0.52–0.58
Yellow	0.59–0.63		
Red	0.63–0.69	0.65−0.69	0.65–0.69
Red-Edge	0.71–0.75		
NIR_1	0.77–0.90	0.78−0.92	0.78–0.92
NIR_2	0.86–1.04		
PAN	0.46–0.80	0.450−0.800	0.450−0.90

2.2 Processing of remote sensed images

To analyse the state of surfaces and their change over time, it is necessary to rely on comparable datasets, so that changes in the measured parameters should be ascribed to changes in the monitored object and not to possible disturbances. Before being used in applications, the collected data need a series of corrections to eliminate or limit disturbances and distortions due to the acquisition system (platform and sensor), the signal propagation medium (atmosphere), the angle of view and the effect of the earth's curvature. The data pre-processing operations are useful to remedy defects inevitably present in the remote sensing images. The need to perform the different operations depends on the type of data and the type of analysis for which these images are to be used. Generally, multispectral images are already geometrically and radiometrically corrected by the various agencies, in some cases the only operation required is atmospheric correction. SAR images, on the other hand, require a more complex chain of pre-processing, and this may vary slightly depending on whether the analysis is carried out on single or multiple images.

In order to retrieve information from a high number of archive multi-temporal images, it is necessary to resort to automatic classification methods. Classification is an operation with which thematic maps are produced from remote sensing data, where each pixel is assigned to a class based on its spectral and/or geometric characteristics.

Depending on the classification method to be used, after the pre-processing and before the classification, other automatic procedures may be required, such as the calculation of multispectral indices, or additive processing (RGB), or image segmentation operations. The classification techniques can be distinguished and grouped into two great categories: pixel-based techniques, based exclusively on the spectral information of the single pixels present in the image; object-based techniques, which use information tied to groups of pixels, considering the interrelationships between contiguous pixels. These, in turn, can be of the supervised and unsupervised type.

Finally, in order to extract useful information to understand the state of objects and their change over time, further automatic procedures are necessary.

2.2.1 Processing tools

There are many existing image processing software packages, which allow to perform pre-processing and classification operations, such as ESA Sentinel Application Platform (SNAP) toolbox, ENVI etc. The Sentinel Application Platform (SNAP) software, provided by ESA, is specifically designed for the processing and analysis of Sentinel images and can be used for processing Radar and optical data. In addition, this software can also be used for other types of data, such as multispectral Landsat images.

A significant alternative for the acquisition and processing of Landsat and Sentinel data is represented by the Google Earth Engine (GEE) platform (https://earthengine.google.com/). The GEE is a cloud computing portal, available for everyone with an internet connection, rendering the data collection of satellite imagery over four decades around the entire world (Gorelick et al., 2017). GEE gives valuable opportunities for global-scale applications in hydrology, food security or others. The free of charge access to satellites data and specific algorithms can possibly reduce some limitations, especially in the developing world. Users can easily use ancillary layers or algorithms in their programming interface without downloading the satellite images and without requiring specialist remote sensing software. Although a plethora of algorithms useful for image processing is provided, the programming scripts allow users to create custom cloud-based computing algorithms for specific functions that are not available on GEE. The data available is from the complete Landsat series, Sentinel 1, 2, and 3, Moderate Resolution Imaging Spectrometer (MODIS), and so on. Some of the considered multi-spectral datasets have been provided both in raw digital numbers and surface reflectance.

Unfortunately, SNAP and Google Earth Engine do not allow Cosmo SkyMed SAR images to be processed. For these images, it is necessary to use commercial or self-produced codes. Among the commercial software beacons, one of the most used is ENVI, which integrates the SARscape module that allows for an easy processing and analysis of SAR data acquired from various satellite platforms. The ENVI software also allows for the continuation of Landsat and Sentinel-2 multispectral data, and in the most recent versions also the sentinel-1 SAR data. Another open-source software useful for some operation on satellite data is the Orfeo Toolbox (OTB) developed by the French space agency. Furthermore, thanks to a series of plugins, it is also possible to perform operations on satellite images in the open-source QGIS software. For some applications, especially for classification and subsequent analysis, Python, Matlab programming languages allow to create custom computing algorithms for specific functions. In this thesis, according to the needs, different platforms have been used including SNAP, GEE, ENVI and SARscape module, Orfeo Toolbox (OTB) and programming languages such as Matlab and Python.

Table 3: Summary of the analysis tools for each case study

Case studies	Satellite Data	Freely available				Commercially available
		SNAP	OTB	Programming languages (Orginal code)	GEE	ENVI+IDL
Wetland	Multispectral images	X	X	Matlab - Python		
Perennial river	Multispectral images	X	X	Matlab	X	
	Sentinel-1 SAR images	X	X	Python	X	
	Multispectral images	X	X	Matlab	X	

Non-perennial rivers	Cosmo SkyMed SAR images					X

Table 3 summarises the analysis tools used for each case study, details of which are given in the following paragraphs. The pre-processing operations on the Sentinel-2 multispectral images, e.g. the atmospheric correction and the resampling of the bands at the same spatial resolution, were carried out in the SNAP software. Similarly, the pre-processing operations on Sentinel-1 SAR images were also performed in the SNAP software. The CosmoSkyMed SAR images, as will be explained later, were instead processed in the ENVI software. Case-specific analyses (e.g. calculation of multispectral indices, calculation of flooded areas, wet channel extraction, etc.) were carried out using original codes developed by myself in programming languages such as Matlab and Python or in GEE. The OTB software was mainly used to georeferenced the outputs obtained from the codes implemented in Matlab and Python.

2.2.2 Pre-processing of multispectral images

Observation of the earth's surface using satellite sensors can be influenced by the interaction between electromagnetic radiation and the atmosphere presence. The earth's atmosphere acts as a filterable level that hinders the passage of electromagnetic radiation causing, in some cases, its complete absorption. Electromagnetic signals at a fixed wavelength can be altered differently by the various atmospheric layers, depending on the chemical composition and the absence or presence of suspended agents. At the same time, the same atmospheric layer can react differently to radiation of different wavelengths. However, it is possible to identify portions of the electromagnetic spectrum with respect to which the disturbing action is moderate. Most of the sensors used for remote sensing on space platforms are built to operate in the ranges of the electromagnetic spectrum for which the atmospheric action is limited, called "atmospheric windows". The best-known atmospheric windows are those that cover the portion of the electromagnetic spectrum between 0.1 to 20 µm and between 0.2 and 100 cm of wavelength. As can be seen in Figure 3, in the region between 0.1 to 20 µm, there are still opaque regions, in correspondence of which it is possible to define even more specific atmospheric windows, such as, for the near and short infrared bands. In the microwave region, on the other hand, most of the radiation passes through the atmosphere without many obstacles.

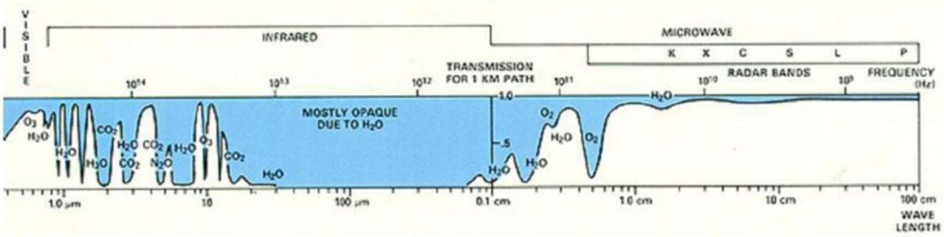

Figure 3: Transmission spectrum of the atmosphere. Blue area is the portion of the electromagnetic spectrum that are blocked, white area is the portion of the electromagnetic spectrum that can be transmitted through the atmosphere, named atmospheric windows. (Source: https://gisetelerilevamento.files.wordpress.com/2010/11/bande.jpg).

When working with multispectral data, it is essential to use surface reflectance products that provide an estimate of the spectral reflectance at ground level after a correction of the atmospheric scattering or absorption. The NASA/USGS provides Level-2 on-demand surface reflectance images. The surface reflectance of Landsat products (Level-2 data products) is generated by the Earth Resources Observation and Science (EROS) center. The on-demand interface EROS Science Processing Architecture (ESPA) corrects satellite images for atmospheric effects through the Land Surface Reflectance Code. While S2 collection delivers Top-of-Atmosphere (TOA) reflectance (level-1C) products for data acquired before 2017 and Bottom-of-Atmosphere (BOA) reflectance images (level-2A) for data acquired after 2017. Therefore, it is necessary to correct the atmospheric effects on the S2 Level 1C images acquired before 2017. For all the case studies presented in this thesis, the Sen2Cor tool, developed by ESA and Telespazio VEGA Deutschland GmbH, was used for this purpose. In addition, a bilinear interpolation algorithm was adopted, implemented in the SNAP tool, to resample at 10 m all the spectral bands that were originally acquired with lower resolutions.

To decrease the revisit time and improve the temporal continuity of monitoring, it may be useful to join the available datasets. To this end, it is necessary to check beforehand whether the images of the various datasets are comparable with each other. In the context of multispectral images, space agencies use different procedures for atmospheric correction, and the configurations of the bands (wavelength and bandwidth) are partially different from one sensor to the other (Figure 2). Mandanici and Bitelli (2016) showed that corresponding bands in Landsat-8 and Sentinel-2 are positively correlated. However, the impact of radiometric differences, between the images acquired by the two sensors, needs careful evaluation for each specific application. The combination of images provided by different sensors can be performed by combining the data, the indexes or the information retrieved separately from each set (Carrasco et al., 2019, Wang et al., 2017). In this thesis, with the goal of providing a tool that is extremely easy to apply, a method based on the integration of the information separately retrieved from the processing of different datasets was used. The results and the compatibility of the information retrieved by the heterogeneous data were verified by checking the coherence of the classification products obtained by the various datasets.

2.2.3 Land cover segmentation trough multispectral indices

Different types of surfaces, such as water, vegetation, bare soil and urbanized areas, have different reflectivity spectra (Ma et al. 2019). This difference is due to the fact that the reflected and emitted quantity of electromagnetic energy differs as the wavelength and the land usage conditions vary (Jensen 2009). The energy reflected by objects at different wavelengths determines an identifying signature of the object, called “*spectral signature*”.

The main land covers that can occur in freshwater environments can be divided into flooded areas, vegetated areas and bare soils. Depending on the environment, wetland or river, but also among river environments, the chemical, physical and structural composition can vary considerably, and influence the spectral response.

The spectral signature of water depends on its chemical and physical characteristics. The clear water (suspended solids <10 mg/l) reflectance spectrum peaks in the green wavelength band (0.50–0.56 µm) and decreases against increasing wavelengths, reaching a reflectance close to zero in the near-infrared (NIR) region (0.75–1.4 µm). The turbid water reflectance spectrum exhibits higher values than clear water in the visible and near-infrared region and approaches zero at longer wavelengths (Malinowski et al. 2015). This is due to the concentration and size of solutes, sediments and organic matter, whose presence reinforces the reflection in the near-infrared band. The above-described patterns are displayed in Figure 4 (adapted from Malinowski et al. 2015). Typically, the water of wetlands, lakes and rivers contains solid particles and could appear not clear. In general, in environments such as lakes, turbidity in the surface layers is low, and the water in most cases has a spectral signature similar to clear water (suspended solids <10 mg/l), whereas in rivers, due to solid transport, turbidity may be greater, and the spectral signature may appear similar to turbid water. In the case of shallow water, the turbidity of the surface layer can be particularly high. Furthermore, in the case of shallow transparent water, the spectral signature can be influenced by the type and colour of the background material.

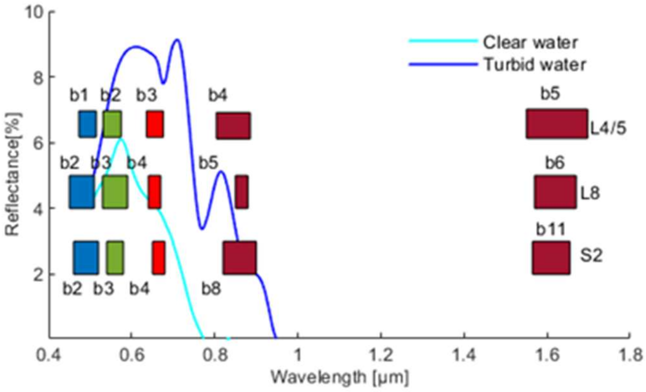

Figure 4: Spectral reflectance of clear (suspended solids <10 mg/l) and turbid water compared to L4/5, L8 and S2 acquired band, reworked from Malinowski et al. 2015.

The spectral response of vegetation varies, as for water, with the wavelength, and depends on multiple factors, such as the type of vegetation, density, state of growth and moisture content. In the visible, the reflected energy values are correlated to the presence of pigments, such as chlorophyll. For the purposes of photosynthesis, vegetation absorbs the visible blue and red radiation and reflects the green one. In the near infrared lengths (0.7-1.35 μm), the spectral signature is influenced by the structure of the leaf, while in the short-wave infrared (1.35- 2.70 μm) by the water content. Healthy vegetation tends to show greater reflectance in the near infrared wavelengths.

For soils, in the same way, the reflectance varies according to their chemical and physical composition. The most important factors are the moisture content, the organic substance content, the texture and the structure. The reflectance of the soil increases with the wavelength and decreases proportionally to the moisture content in correspondence with the water absorption peaks (e.g., 1.4, 1.9, 2.7 μm). The reflectance of a moist ground is lower than that of a dry ground.

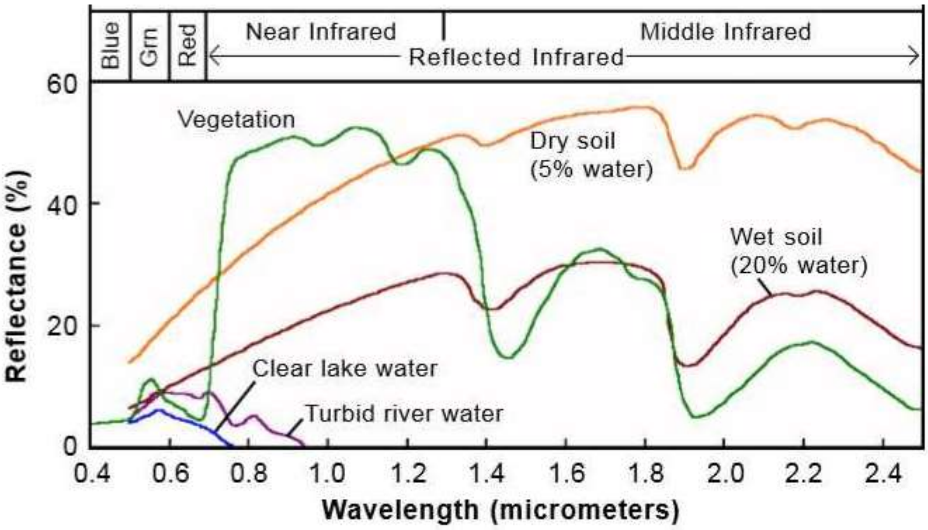

Figure 5: Spectral reflectance of clear lake water (suspended solids <10 mg/l), turbid river water, vegetation, dry soil and wet soil, (source: https://www.progressivegardening.com/agricultural-meteorology/pft-[erm-e-x-100.html).

The differences in spectral signatures are typically exploited for the automatic classification of land cover. For land cover classification, various multispectral indices have been developed, using the VIS, NIR and SWIR bands. The widely used Normalized Difference Water Index (*NDWI*) (McFeeters 1996) is defined as:

$$NDWI = \frac{\rho_{green} - \rho_{NIR}}{\rho_{green} + \rho_{NIR}} \tag{1}$$

where ρ_{green} and ρ_{NIR} are the reflectivity in the green and NIR bands. It can be argued from the spectra presented in Figures 4 and 5 that areas covered with clean water will be characterized by positive values of *NDWI*. On the contrary, it is expected that the surfaces covered by turbid waters will manifest almost null values of *NDWI*. In contrast, both clean and turbid water will be characterized by positive values of *MNDWI* (Xu et al., 2006), which uses the short-wavelength infrared $\rho_{\mathrm{SWIR\_1}}$ (SWIR) (1.4–3 μm) in place of the NIR reflectivity:

$$MNDWI = \frac{\rho_{green} - \rho_{SWIR\_1}}{\rho_{green} + \rho_{SWIR\_1}} \tag{2}$$

Along with the water indices, the Normalized Difference Vegetation Index (*NDVI*) (Curran 1983) is used to identify vegetated areas. The *NDVI* is defined as a combination of the NIR and visible red (ρ_{red}) to bring out the significant difference in the vegetation spectrum in these bands:

$$NDVI = \frac{\rho_{NIR} - \rho_{red}}{\rho_{NIR} + \rho_{red}} \tag{3}$$

In Table 4, the bands used to compute the *NDWI*, *MNDWI* and *NDVI* indices are specified for the L4/5-8 and S2 datasets.

Table 4: Specification of bands used in the multispectral indices' calculation. Where "ρ" indicates the reflectance value relative to the various multispectral bands. The numbers in the subscript (e.g. 2, 3…11) represent the names of the bands.

Landsat-4/5	Landsat-8	Sentinel-2
$NDWI = \frac{\rho_2 - \rho_4}{\rho_2 + \rho_4}$	$NDWI = \frac{\rho_3 - \rho_5}{\rho_3 + \rho_5}$	$NDWI = \frac{\rho_3 - \rho_8}{\rho_3 + \rho_8}$

$MNDWI = \frac{\rho_2 - \rho_5}{\rho_2 + \rho_5}$	$MNDWI = \frac{\rho_3 - \rho_6}{\rho_3 + \rho_6}$	$MNDWI = \frac{\rho_3 - \rho_{11}}{\rho_3 + \rho_{11}}$
$NDVI = \frac{\rho_4 - \rho_3}{\rho_4 + \rho_3}$	$NDVI = \frac{\rho_5 - \rho_4}{\rho_5 + \rho_4}$	$NDVI = \frac{\rho_8 - \rho_4}{\rho_8 + \rho_4}$

Some of the classification methods that will be introduced in the various case studies are based on the use of multispectral indices as well as on the analysis of the spectral signatures of the various land covers.

2.2.4 Pre-processing of SAR images

SAR images, unlike multispectral images, require a longer and more complex pre-processing. The amplitude SAR images, which contain information on the part of the electromagnetic field reflected towards the sensor, are not immediately interpretable because of the characteristic speckle noise. The speckle appears visually in the form of a “salt and pepper” noise and is an inevitable feature of SAR data. This speckle effect is the consequence of the presence of small objects (at the wavelength scale) and of the coherent nature of illumination in the pixel. Due to the microscopic details of these objects’ shapes and positions, the signals may interfere constructively or destructively (Gargiulo et al., 2020).

The pre-processing of SAR Sentinel-1 GRD product is not univocal, several pre-processing chains are proposed in literature (Filipponi 2019, SAR Basics with the Sentinel-1 Toolbox in SNAP tutorial). Filipponi (2019) proposes seven pre-processing steps, designed to best reduce propagation errors in subsequent processes. The pre-processing chain suggested by Filippone (2019) concerns single SAR image analysis, and includes the following steps: Apply Orbit File, Thermal Noise Removal, Border Noise Removal, Calibration, Speckle Filtering, Range Doppler Terrain Correction and Conversion to dB.

The first step “apply orbit file” consist of acquiring the satellite's orbit file. The second step is useful for removing the thermal noise that disturbs the intensity of the image, while the third step allows to reduce low intensity noise and invalid data on the scene edges. The step “Calibration” converts digital pixel values to radiometrically calibrated SAR backscatter. The information required to apply the calibration equation is included within the Sentinel-1 GRD product; specifically, a calibration vector included as an annotation in the product allows for a simple conversion of image intensity values into sigma nought values. Speckle filtering is a procedure to increase image quality by reducing speckle. When such a procedure is done at an early processing stage of the SAR data, the speckle is not propagated into any ongoing processes. SAR data are generally sensed with a varying viewing angle greater than zero degrees, resulting in images with some distortion related to side-looking geometry. Terrain corrections are intended to compensate for these distortions so that the geometric representation of the image will be as close as possible to the real world. Range Doppler terrain correction is a correction of geometric distortions caused by topography, such as foreshortening and shadows. This operation can be done by using or not a digital elevation model to correct the location of each pixel. The last step “Conversion to dB” is useful to convert the backscatter coefficient in dB using a logarithmic transformation. This last operation is not strictly necessary, it is more useful in images visualization. In cases where multitemporal analyses are carried out, it is advisable to also perform a Coregistration, which records the set of images on the same reference grid; and Multitemporal Speckle Filters instead of single Speckle Filters, which take advantages of multiple SAR observations in time.

In the present work, using a set of Sentinel-1 images, the following procedure was performed: Apply Orbit File, Thermal Noise Removal, Border Noise Removal, Calibration, Coregistration and Multitemporal Speckle Filters. The Refined Lee multitemporal speckle filter, having a window size 5 × 5, was performed. One of the tools available to perform these operations is SNAP, within which it is possible to implement the six pre-processing steps. The preprocessing of Sentinel-1 images can be implemented also in GEE.

Once the speckle effect was eliminated, an automatic classification was carried out, presented in §5.9, and subsequently a georeferencing of the images by existing analysis tool, such as OTB software. In order to simultaneously georeference the entire image archive, an original Python code was created to perform the georeferencing operation implemented in OTB automatically on a large number of images.

The CosmoSkyMed images were processed in the ENVI SARscape software. The images were registered on the same grid reference (Coregistration), and after, a data calibration and speckle reduction were performed. The speckle reduction was performed by employing the multi-temporal De Grandi filtering implemented in ENVI SARscape (De Grandi et al., 1997). De Grandi filtering allows to reduce speckle without degrading the spatial resolution. In this case, however, the images, after the removal of the speckle, were georeferenced with a DEM at 5 m inside ENVI SARscape.

3. Challenges and opportunities of satellite monitoring of freshwater environments

To monitor freshwater environments, valid, accurate and standardized data are needed.

In situ monitoring provides detailed information on the characteristics of freshwater environments. Unfortunately, in situ approaches cannot be highly frequent and they are limited to point representations of complex and dynamic systems. In addition, in situ measurements are also limited by several logistical issues such as access, cost and timing. Consequently, in situ method can be feasibly practiced only in limited geographical areas and for some time periods (Bizzi et. al 2016).

Acquisition by remote pilot systems is also limited to some geographical areas due to high costs and time. The acquisition of images with global coverage from remotely piloted systems or aerial platforms is tied to multi-year surveys conducted by national and/or regional environmental agencies. They provide images with a spatial resolution of the order of 0.5 m, but, in the best-case scenario, temporal resolutions are in the order of several years or decades (Carbonneau et al. 2020).

Satellite remote sensing is a comparatively cost-effective and timely tool over monitoring systems. It enables spatially continuous, regular, and repeatable observations over large spatial domains and at multidecadal time scales. Moreover, in recent years, the number of satellites at ever higher spatial resolutions has been increasing.

The potential of multispectral and SAR satellite data in monitoring freshwater environments has been investigated in the last decade. For example, multispectral data have been used for monitoring lake (Wu et al., 2009, Wan et al., 2014) and wetlands (Kaplan et al., 2017, Halabisky et al. 2016).

Traditional multispectral satellite data such us Landsat, ASTER and MODIS have been used in fluvial remote sensing studies (Carbonneau & Piégay 2012, Henshaw et al., 2013). However, their use has often been limited to the study of large rivers and the analysis of evolutionary processes that are not rapid, due to their coarse spatial and temporal resolution. SAR data, instead, have been used primarily for lake detection (Strozzi et al., 2012), wetlands mapping (White et al., 2015, Brisco et al., 2015) and flood detecting and mapping (Rahman et al., 2018), but little is known about their capabilities to monitor hydro-morphological changes along rivers.

Recently, satellite data have started to achieve adequate spatial, spectral and temporal resolution for river sciences (Carbonneau et al. 2020). Satellite data in the public domain such as Sentinel or Landsat-8/9 offer a reasonable temporal repetition rate with at much higher spatial and spectral resolutions. For example, Sentinel-2 has thirteen bands, four of which are natively acquired at 10 m spatial resolution. Downing et al. (2012) estimated that the average width of fifth-order streams is about 30 m and that streams with orders 5-12 occupy 76% of the global stream area. Sentinel-2 data should therefore at least be able to detect such flows and thus be sensitive to most of the world's rivers (Carbonneau et al. 2020). We are entering an era in which river channel shapes and processes can be observed and classified by satellites on an almost weekly basis for large rivers around the world. This opportunity requires specific and interdisciplinary expertise. For this reason, this new satellite information has not yet resulted in concrete progress in understanding river process (Piegay et al., 2019).

One of the main challenges is the implementation of classification methods that provide maps that are as consistent as possible with reality on the ground, but at the same time can be used by people who are not experienced in processing satellite data.

Multispectral sensors acquire data with high spectral resolution in the visible and infrared range and this makes them suitable for identifying different types of land cover, such as water, vegetation and bare soil (see, e.g., (Rebelo et al., 2019, Munyati 2000, Yang and Liu 2005)).

The practical exploitation of the high number of archive multi-temporal images depends on the possibility of automatic classification. Many methods are available in literature, mostly exploiting the peculiar reflectivity spectrum of land covers. The different spectral responses have been frequently exploited to define multispectral indices. Past works have shown that the use of one or more indices obtained from multispectral sensors is an effective method in monitoring wetlands and rivers (Ozemi & Bauer 2002, Gilvear and Bryant 2016).

Satellite monitoring and mapping of freshwater environments are highly complex operations. These environments are not unified by a common land cover type, but water, soil and vegetation interact with each other. The combination of different types of land covers within a single pixel can lead to different behaviors of the individual element and consequently to misinterpretations or misclassifications (Gilvear and Bryant 2016). They are highly dynamic environments in time and space. The cover of these environments can vary from open water to vegetation-choked surfaces, and water levels can range from a few centimeters to a few meters. Vegetation can be characterized by grass, shrub, or trees. Mapping and monitoring become even more complex when the size of the object to be monitored is comparable to the pixel resolution. All these aspects significantly influence the spectral behavior and the interaction between the electromagnetic signal and the sensor (backscatter). Consequently, each freshwater environment requires specific analyses before the appropriate classification method can be identified. To evaluate the present and past conditions of the system and identify the occurrence of time changes, the classification methods must be able to provide a time series of data that is consistent in time and space.

3.1 Remote observation of Wetlands

Wetlands, natural or man-made, permanent or temporary, provide essential ecosystem services all over the Earth. They contribute to improving water quality, protecting shorelines, recharging groundwater, reducing flood and drought severity, while also providing unique habitats for many plants and animals (Guo et al., 2017). The role of wetlands in maintaining the biodiversity of aquatic ecosystems has motivated several international environmental protection initiatives, such as the Ramsar Convention (Matthews 1993). Despite their recognized importance, wetlands are among the most threatened ecosystems in the world. More than 50% of the world's wetlands have been converted or lost in the last century (Gezie et al., 2017). They were either completely converted to other land uses or their ecological functionality was gradually altered by changing the hydrologic regime and introducing farming and agriculture (Revenga et al., 2000). In the Mediterranean region, approximately 80–90% of natural wetlands have disappeared and 23% of the remaining wetlands have been artificially managed as rice fields, salt pans or water storage for irrigation purposes (Perennou et al., 2012). Many studies have demonstrated the ecological value of artificial wetlands as surrogate habitats for many species of aquatic invertebrates and birds (Tourenq et al., 2001, Ma et al., 2004, Balcombe et al., 2005, Bellio et al., 2009, Pires et al., 2016). Rice fields, currently accounting for 15% of the world's wetlands (Lawler 2001), are one of the essential artificial habitats for the conservation of many aquatic species (Pernollet et al., 2015). Aquatic habitat availability for many species depends on several factors, including the duration and extent of flooding (Stenert at al., 2009), the water depth (Baumgartner et al., 2008), the sediment content (White et al., 2019), the water quality (Gezie et al., 2017, Preston et al., 2018, Burger et al., 2018, Kim et al., 2019) and the presence of aquatic and terrestrial vegetation (Kim et al., 2019, Schad et al., 2020). Wetland management practices that shorten the duration of flooding periods may significantly reduce the ecological value of rice fields and cause the decline of many aquatic species (Lawler 2001, Machado and Maltchik 2009). The conservation of biodiversity in artificial wetlands and rice fields requires proper duration, frequency and seasonality of flooding. Many studies have shown how the winter flooding of rice fields contributes to increasing habitat availability for birds (Pernollet et al., 2015, Elphick 2000, Tajiri et al., 2013).

Continuous monitoring is essential to optimize their management and quantify habitat availability for water-related organisms. Wetlands are characterized by a large variety of land cover classes, and this makes them particularly complex to monitor. Wetland satellite monitoring is interesting since it is relatively inexpensive and provides information at different spatial and temporal scales with even high acquisition frequencies. The Ramsar Convention encouraged the development and implementation of remote sensing applications for wetland monitoring (Rebelo et al., 2019). However, mapping wetlands by satellite with levels of accuracy that can be used for biodiversity conservation is highly complex.

Multispectral sensors are particularly useful in analysing the spectral characteristics of wetlands as they acquire information in various spectral bands. The characteristics and properties of wetlands can be studied by measuring the spectral response of various land cover classes in different parts of the electromagnetic spectrum. For example, Amani et al. (2018) developed an extensive analysis of Sentinel-2, Landsat-8 and other multispectral datasets, investigating the capability to distinguish soil, water and vegetation by exploiting their spectral signatures. They found that the red, red-edge (RE) and near-infrared (NIR) bands are the most appropriate for wetland classification, while the shortwave infrared (SWIR) bands exhibited intermediate separability and were helpful in specific cases (e.g., for discriminating the shallow water class). In particular, the reflectance of the SWIR band decreases as the moisture content increases, allowing dry soils to be distinguished from wet soils. However, moist soils and soils covered by shallow water provide similar reflectance in the SWIR band and cannot be separated. The different spectral responses have been frequently exploited to define multispectral indices. For example, Davranche et al. (2013) combined various multispectral indices in a classification tree, in order to monitor the Camargue wetland by multispectral SPOT-

5 images (10 m spatial resolution). Pernollet et al. (2015) used the Modified Normalized Difference Water Index (*MNDWI*), extracted from the Landsat dataset, to map open water areas in five study regions. Li et al. (2013) used multispectral indices with ALI and Landsat data (30 m spatial resolution), while Li et al. (2015) used MODIS data (250 m spatial resolution).

Supervised classification algorithms have also been used by many authors (e.g., (Rebelo et al., 2009 , Munyati 2000)). Forkuor et al. (2017) used random forest and support vector machine algorithms and showed the potentialities of multi-sensor approaches. Dronova et al. (2011) performed change detection using object-based analysis for the mapping of four wetland land cover classes (water, vegetation, sand and mud flood), by using multispectral data from the Beijing-1 microsatellite sensor, with a resolution of 30–40 m. However, the use of supervised classification methods is limited in practical application because they need a large amount of training data. A comprehensive review of remote sensing data and methods for wetland classification was provided by Mahdavi et al. (2018).

Despite many advances in remote sensing technology, wetland land cover classification is still an unresolved problem due to the difficulties linked to their extreme heterogeneity and frequent time changes. Ozesmi and Bauer (2002) pointed out that, in the case of wetlands, satellite image classification is challenging due to fluctuating water levels, which change the spectral reflectance of vegetation, and the presence of floating masses of periphyton. The classification of flooded areas is particularly challenging, especially when the water depth is shallow, water turbidity high and there is emergent or submerged vegetation, along with a continuous succession of small emerged and submerged patches.

3.2 Remote observation of Rivers

Rivers, as well as wetlands, are highly complex environments that provide essential ecosystem services. Human-induced pressures and impacts through over-exploitation of water resources, pollution, changes in flow regimes, hydro-morphological alterations and climate change have led to an increasing deterioration of natural habitats (Grizzetti et al. 2017).

Many studies have pointed out that river hydro-morphology, and its evolution over time, has substantial effects on fluvial habitats and biodiversity (Garcia et al. 2012; Rinaldi et al. 2017). In Europe, the Water Framework Directive 2000/60/CE (WFD 2000) highlighted the importance of hydro-morphological quality, in addition to the physico-chemical and biological quality, in the assessment of the ecological status of rivers. As a support tool for hydro-morphological assessments, a multi-scale, hierarchical framework was developed within the REFORM project (Restoring rivers for effective catchment Management, reformrivers.eu). The framework delineates regional landscapes into nested spatial units at catchment, landscape, segment, reach, geomorphic and hydraulic units (Gurnell et al. 2015).

The monitoring and evaluation of river changes, from the catchment scale to the hydraulic unit scale, are necessary for the identification of optimal management practices, aiming at the improvement of river ecological status.

The adequate extents and resolutions (both spatial and temporal) of the monitoring are determined by the hydro-morphological process under examination and the size of the watercourse. The portion of territory to be monitored ranges from a few to several hundred square kilometres and the observation period ranges from one to one hundred years or more. The needed spatial resolution depends on the dimension of the target: in the case of rivers, the relevant dimension is the width (Legleiter and Fonstad 2012; Gilvear and Bryant 2016). The time resolution depends on the speed of evolution of the observed process (Boothroyd et al. 2021b). It follows that, in many cases, a large amount of monitoring data is required. For example, the evaluation of the effectiveness of river restoration requires extensive monitoring both pre and post intervention (Nones 2016) covering several years and spatial extent of the order of several kilometres, with a monthly revisit time and spatial resolution proportionate to the river width.

The hydro-morphological monitoring of rivers has found great interest in the scientific world (Bizzi et al. 2016; Nones et al. 2017; Rinaldi et al. 2017). In the last decades, the interest in remote monitoring has grown (Marcus and Fonstad 2010), and many studies have exploited the potential of airborne (Marcus et al. 2003; Gilvear et al. 2004; Casado et al. 2015) and drone (Woodget et al. 2017) remote sensing. These instruments offer the possibility to create maps with a very high spatial resolution (about 1 m), but they still have the drawback of limited availability in frequency and coverage. Satellite sensors are powerful means for observing hydro-morphological changes (Tomsett and Leyland 2019). Thanks to their global coverage, they allow for the continuous monitoring of vast areas, from catchment scale to geomorphic and hydraulic units, and in some cases, long historical archives of observations with high temporal resolution are available. For a small-scale analysis (e.g., geomorphic and hydraulic units) and for monitoring the hydro-morphological processes in medium rivers (width in the range of 20–200 m, Gilvear and Bryant 2016 and Latrubesse 2015), very high-resolution satellite images (e.g., GeoEye, WorldView, Quick Bird, Planet) are suitable. However, in most cases, acquiring very high spatial resolution images of large areas is still too expensive. The Google Earth Pro Platform provides an enormous reservoir of freely-available remotely sensed data that can support the study of river physical forms (Henshaw et al. 2020). However, these images are available with a rather poor temporal resolution and therefore not sufficient for the analysis of evolutionary processes occurring on lower time scales. As of now, freely available data, with adequate temporal resolution (a few days), are available only at moderate spatial resolutions (10–30 m). Landsat TM/OLI and Sentinel-2 belong to this typology: they provide multispectral images with variable resolutions (10, 20, 30, 60 m) according to the band, with short revisit times, in the range of 5–9 days. Following Jiang et al. (2014), the minimum width of the river that can be monitored is equal to three image pixels, therefore Landsat and Sentinel-2 data can be used for rivers wider than about 90 m and 30 m respectively. These data offer the opportunity to perform analyses at various spatial scales (e.g., catchment, landscape, segment, reach and macro morphological units). There is a growing amount of literature on integrating data between two or more satellites and using multispectral moderate resolution data for inferring information on riverine dynamics from catchment to reach scales. Examples of the applications are wet channel mapping and hydro-morphological changes monitoring. At the catchment scale, Wang et al. (2021) used Sentinel-2 images to extract drainage networks in the Lancang-Mekong River basin. At a lower scale (e.g., segment, reach), Baki and Gan (2012) used Multispectral Scanner System (MSS) Landsat images, with a spatial resolution of 80 m, and TM Landsat images, with a spatial resolution of 30 m, for monitoring the bank erosion/accretion and island dynamics of the Jamuna River (average channel width of about 10 km) for three decades (1973–2003). Dewan et al. (2017) analysed the planform dynamics of the Gange (average width of about 1–8 km) and the Padma rivers within Bangladesh for the period 1973–2011, using multitemporal Landsat images. Jiang et al. (2014) used TM Landsat and ETMþ (Enhanced Thematic Mapper Plus) images, with 30 m spatial resolution, for the wet channel mapping of six different rivers in the north and north-western China. In this study, the authors evaluated the ability of the Landsat data to monitor both narrow (less than three pixels wide) and large rivers. Other authors have exploited the potential of such data to extract information at even finer scales. For example, Carbonneau et al. (2020) used Sentinel-2 images to delimit water, vegetation, and dry-sediment, detect vegetation growth, and delimit active channel on four Italian rivers: the Po River, the Sesia River (average active channel width of 100 m), the Paglia River (average active channel width of 30 m), and the Bonamico River (average active channel width of 300 m). Kryniecka and Magnuszewski (2021) used Sentinel-2 images to study alternate sandbars movement on the Vistula River (average width of 2–5 km) in Poland. Seaton et al. (2020) detected changes in the size of water pools in non-perennial rivers like the Nuwejaars, Breede, Tankwa and Touws (average width 40–100 m) in the Western Cape, South Africa, from 2016 to 2017, using a combination of Landsat-8 and Sentinel-2 datasets.

3.3 Remote observation of non-perennial rivers

Remote data (drones, satellites, etc.) have rarely been used in the monitoring of non-perennial rivers for a variety of reasons. First, non-perennial rivers were historically neglected both at regulatory and scientific levels. Secondly, past missions did not provide the necessary measurement resolutions.

This typology of river is widely distributed all around the world and represents more than half of global stream network (Datry et al., 2014, Skoulikidis et al., 2017, Messager et al, 2021). Particularly, they result predominant in Mediterranean catchments, where marked dry/wet climate patterns favour their occurrence (Skoulikidis et al., 2017), but are also characteristic of seasonally frozen regions and karst environments (Shanafield et al., 2021).

In the Mediterranean region, the number of temporary rivers is expected to increase in the coming years, as anthropogenic pressures such as withdrawals for irrigation purposes, land use changes and climate change can turn perennial rivers into temporary rivers or increase the intermittent nature in already non-perennial rivers. The value of non-perennial rivers and streams has been historically underestimated (Datry et al., 2014), and only since a few years, an interest in their hydrology, ecology, management and conservation has developed. However, there are still many scientific and management gaps to be overcome. Adequate management is precluded by a general lack of information on the duration and frequency of the periods of zero flow. Unfortunately, in most cases, there are no gauging stations along non-perennial rivers. The gauging stations are mainly concentrated on the main perennial rivers, while the smaller network, to which the temporary rivers normally belong, is almost always ungauged. The lack of hydrological measurements prevents the definition of the flow regime as well as the intermittent behaviour of these watercourses. The scarcity of data has triggered the development of alternative methods, including citizen science or expert field observations of the flow regime. However, these efforts only provide local information and suffer from several limitations. Furthermore, even if gauging stations are present, they are not adequate to describe the space-pattern of the presence/absence of water. In the presence of a strong longitudinal variability of the flow rate, the measurement in one point cannot be representative of the entire watercourse. In addition, temporary rivers are often characterized by long periods of non-flow with the presence of pools of water. These conditions cannot be extrapolated from point measurements; in order to identify them, an overall view of the river reach is necessary.

Consequently, the lack of a monitoring network and the scarce information provided by traditional gauging systems also make it impossible to develop adequate hydrological models. Common hydrological models applied to this type of watercourse have demonstrated multiple constraints due to the highly unpredictable flow regime. In the absence of adequate data and hydrological models, an approach capable of reconstructing the flow regime of non-perennial watercourses is still lacking. Furthermore, the global extent and number of non-perennial rivers is largely unknown, and their mapping is therefore necessary. In this context, the use of satellite data constitutes a unique and crucial resource. The recently launched Sentinel-2, with improved spatial resolution of 10 m for some bands, make it possible to employ satellite data for the monitoring of such environments.

In addition to choosing the adequate data set, it is necessary to identify the appropriate classification algorithm for automatically extract river units (e.g., wet channel, ponds of water, sediment bars and vegetated areas) and monitoring the hydro-morphological changes in a continuous way through time. In remote sensing, when the size of the detected object is almost equal to the pixel size, or the pixel edge does not coincide with the edge of the elements to be monitored, data interpretation and automatic classification become a real challenge.

4. Remote monitoring of wetland flooding: the study case of the Albufera wetland (Spain)

This chapter presents the application relating to monitoring wetlands. For this particular application, multispectral multi-temporal images, Landsat-8 and Sentinel-2, were used.

The main objective of this work is to develop a classification method for monitoring the wetland land cover and the temporal succession of flooding and drying, with the aim of providing a useful tool for the protection of biodiversity in these precious environments. A rule-based classification method will be presented, based on three multispectral indices, to discriminate four land cover classes and monitor the evolution and duration of flooding.

The case study is the Albufera wetland, located in the western area of the Mediterranean Sea, in the Iberian Peninsula. Previous research on the satellite remote sensing of the Albufera wetland had objectives other than the one presented here, such as water quality estimation (Lopez-Garcia et al 1987, Dona et al., 2015, Sòria-Perpinyà et al., 2020, Soria et al., 2021). The Albufera wetland can be used as an example of a natural wetland that was transformed into an artificially managed one over the years, and to date, it is mostly devoted to rice cultivation (Soria et al. 2021). Despite its transformation, the Albufera offers a great variety of habitats and species of community interest. In this application, the information acquired by L8 and S2 data were jointly used in order to reduce the revisit time and consequently improve the temporal continuity of monitoring.

The results presented in this chapter have been published in the Remote Sensing journal (Cavallo et al., 2021).

4.1 Case study: the Albufera Wetland, Spain

The Albufera is a Mediterranean coastal wetland located 10 km south of the city of Valencia in Spain (Figure 6). This wetland covers an area of 210 km^2; it includes the Albufera lake, with a surface of approximately 24 km^2, and rice fields with an area of around 150 km^2.

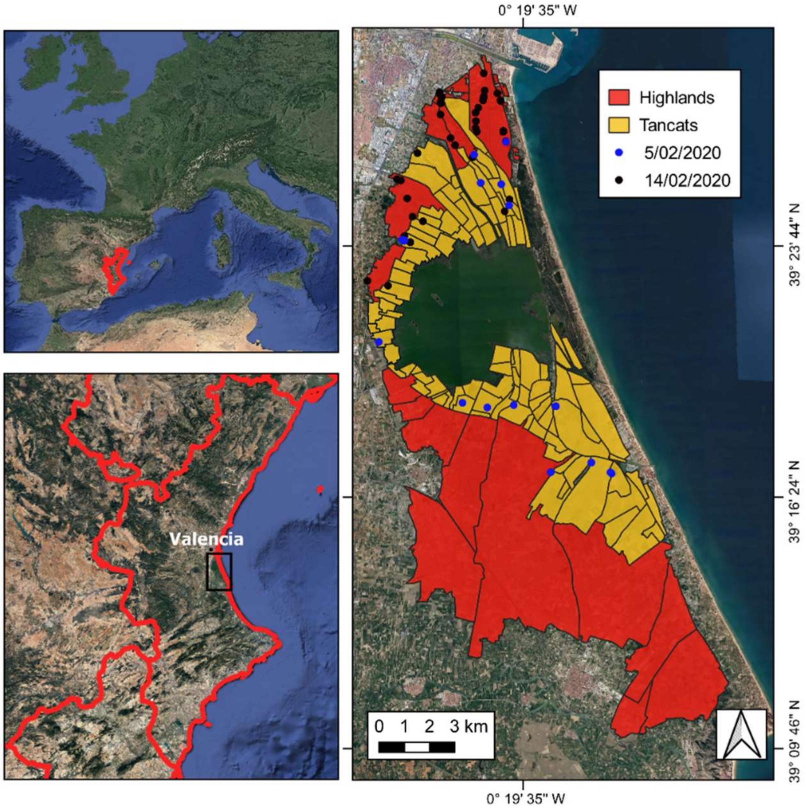

Figure 6: Overview of the Albufera wetland (© Google 2020) and outline of the rice fields with lower (Tancats) and higher elevation (highlands). The points represent the locations of field surveys performed on 5th February 2020 and 14th February 2020.

The Albufera wetland was declared a Natural Park in 1986 and was included in the Ramsar Convention on "Wetlands of International Importance" in 1989, because, during the winter flooding, it offers habitats for migratory birds. It is also part of the Natura 2000 network as a Special Protection Area for Birds (SPA) under the Birds

Directive 2009/147/EC (site code ES0000471), and a Site of Community Importance (SCI) under Habitats Directive 92/43/EEC (site code ES0000023). The SCI site hosts, in total, 115 species, referred to in Article 4 of the Birds Directive and listed in Annex II of the Habitats Directive. Among them, 64 winter and 35 reproduce in the wetland. Among the protected fish species, there are the Spanish Cyprinodont, classified as endangered, and the Valencia Toothcarp, classified as critically endangered. The endangered plants Marsilea and Marsilea Quadrifolia are also present.

From a geological point of view, the site is located in a sedimentary basin of Holocene origin that includes the coastal plain of the province of Valencia. The climate is Mediterranean, with mild winters and warm to hot summers. The average annual precipitation is less than 460 mm, with a maximum in October and a minimum in July.

The Albufera lake is the largest freshwater body on the Iberian Peninsula; it is fed by irrigation channels, storm water streams and urban and industrial wastewater treatment plants. The Albufera lake is connected to the Mediterranean Sea through two natural channels and one artificial channel called "golas", where sluice gates control the freshwater outflow towards the sea and regulate the water level of the lake. The wetland flooding is managed in two different ways (see Figure 6). The rice fields close to the lake correspond to the traditional area previously occupied by the lake. Earth dikes and pumping stations were introduced to regulate the water level in these lowlands, which are locally called "*Tancats*". The highlands, further away from the lake and at a higher elevation, are flooded from the Turia and Xuquer Rivers. In addition to these water sources, since 1990, the northern part of the wetland has been irrigated with the outlet of the wastewater treatment plant of Pinedo, located at the northern boundary of the natural park.

Water levels and the extension of the flooding area are regulated by different irrigation communities according to the needs of rice cultivation. Rice fields constitute a temporary wetland with a summer flood cycle and a winter flood cycle. The summer flooding usually starts in May and ends in mid-September, when the farmers dry up the fields for harvesting. The duration of the summer flooding is determined by the rice cultivation technique. Winter flooding starts around the end of October and lasts until the beginning of March. The purposes of the winter flooding are to provide habitats for water-related animals and plants, and to support recreational activities such as hunting (Soria et al. 2021). The winter flooding is economically supported by the European Agricultural Fund for Rural Development (EAFRD). In winter periods, the *Tancats* are completely flooded with the water level at the top of the dikes and the rice fields are hydraulically connected to each other. Parts of the highlands are also flooded but the water depth may be of the order of a few centimetres only. Given the unpredictability of the duration of winter flooding and its importance for maintaining biodiversity, this work is focused specifically on the monitoring of the winter period.

4.1.1 Remote sensing data

For this case study, 81 cloud-free Landsat-8 images, acquired from 2013 to 2020 and 69 cloud-free Level 2A Sentinel-2 images, acquired from 2015 to 2020, from September to April, were used. In addition, I employed very high-resolution images (VHR) of the GeoEye-1 (GE-1) and WorldView-4 (WV-4) satellites (whose characteristics have been described in § 2.1.5) and field data to validate the results obtained from the L8 and S2 images, from September to April, were used. During my research at the Polytechnic University of Valencia, I planned with the ESA an acquisition of a very high-resolution image on a day close to the acquisition of the Landsat-8 and Sentinel-2 satellites. In this case, since Landsat-8 and Sentinel-2 passed on the 13th and 15th respectively, the acquisition by the GeoEye-01 satellite took place on the 14th, on the same day Professor Guillermo Palau Salvador and I acquired geolocated pictures inside the Albufera park.

4.1.2 Field survey

To evaluate the potential of automatic-classification method of the multispectral images, in addition to VHR images, the 5th February 2020 and the 14th February 2020, I performed a field survey on the Albufera wetland at the same time of the satellite acquisitions. In particular, geo-located pictures of the area of interest were acquired in various conditions: dry, flooded, with and without vegetation. On 5th February 2020, the pictures were taken in correspondence to 18 points located in different parts of the Albufera wetland (see Figure 6). In this survey, the acquisition points were preferentially fixed in correspondence to the *Tancats*, where, at the time of acquisition, the area was mostly covered by water. On 14th February 2020, 38 geo-located pictures were taken in the north-west of the Albufera at the boundary between the *Tancats* and the highlands. This area is characterized by a variety of land cover patches. As previously specified, the survey was purposely scheduled on the same day of the WV-4 acquisition and within a few days of the L8 and S2 acquisitions. A set of the acquired pictures, showing the most common land cover types in the winter period, is provided in Figure 7. Figure 7 (a/b) represents the typical winter condition in the *Tancats*, that are flooded with about one metre of water depths in the winter period. The condition in Figure 7 (c, d, e, f, g, h, i, j, k) are present at the edge of the *Tancats* area.

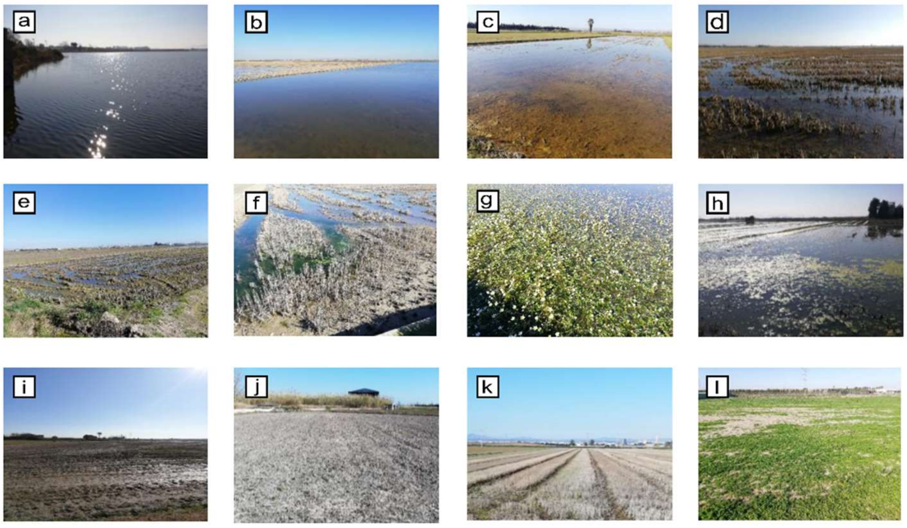

Figure 7: Photographs of land cover classes taken in the Albufera wetland on 14th February 2020; (a,b) water; (c) shallow turbid water; (d) shallow water with dead vegetation; (e,f) mosaic of water ponds, mud and vegetation; (g,h) flooded area partially covered by vegetation; (i) wet soil; (j) dry soil; (k,l) vegetated soil.

4.2 Rule-Based Classification of Land Cover Classes

As illustrated in Figure 7, the Albufera wetland's land cover, in the winter period, is extremely variegated. Considering the classification capacity of the multispectral indices, described in chapter 2, land cover types were grouped into four classes: *Open water; Mosaic of water, mud and vegetation; Bare soil and Vegetated soil*. In the following, the rule-based classification method used to discriminate the four classes will be described. This method was implemented in original code in Matlab.

Following previous literature studies (Holben 1986, Rutkay et al., 2020), a threshold of 0.3 to discriminate the presence of vegetation in the observed area and a threshold equal to zero for both water indices were employed.

The first class, labelled "*Open water*" (*W*), represents the typical winter condition in the *Tancats* that are flooded, with water depths ranging from around 0.5 to 1 m (see Figure 7a,b). It is worth noting that in some *Tancats*, dried rice plants could emerge from the shallow water, as shown in the background of Figure 7b. The *W* class refers to flooded areas with a smooth clear surface and significant depth (higher than approximately 20 cm). In these areas, the sediment content of the water layer close to the surface is low, as shown in the pictures in Figure 7. As the multispectral response is determined by this surface layer, the *NDWI* results in a positive value. Consequently, the *W* class can be identified with positive values of the water indices (*NDWI* and *MNDWI*) and below-threshold values of the vegetation index (*NDVI*).

In the marginal areas of the *Tancats*, patches of shallow water, mud and vegetation may coexist for transitional periods. As an example, Figure 7e,f show ponds of shallow water surrounded by mud, grass and dead vegetation. Figure 7c shows an area flooded with shallow and turbid water; Figure 7d shows an area flooded with a thin layer of water, from which dry rice plants emerge; Figure 7g,h show flooded areas partially covered with vegetation. All these situations are grouped into the second class, labelled "*Mosaic of water, mud and vegetation*" (*M*). These areas can be identified with low values of the *NDWI*, high values of the *MNDWI* and any value (the ∀ sign) assumed by the *NDVI*. The third class, labelled "Bare soil" (S), represents wet and dry bare soils (see Figure 7i,j). These areas can be identified in the satellite images with low values of the water and vegetation indices.

Finally, the fourth class, labelled "*Vegetated soil*" (*V*), represents soils partially or entirely covered by vegetation, in wet and dry conditions, as presented in Figure 7k,l. These areas can be identified with negative values of the water indices and above-threshold values of the vegetation index.

Based on these considerations, a rule-based classification that allows to distinguish the four classes was developed by exploiting the combination of the responses of the three multispectral indices. The adopted rule-based classification method is summarized in Table 5. The few pixels that do not meet the adopted conditions were considered outliers and labelled as non-classified.

Table 5: Rule-base classification method for the mapping of the four land cover classes.

Land Cover classes	Photos	Class	*NDWI*	*MNDWI*	*NDVI*

Open Water	a/b	*W*	>0	>0	<0.3
Mosaic of water, mud and vegetation	c/d/e/f/g/h	*M*	<0	>0	∀
Bare soil	i-j	*S*	<0	<0	<0.3
Vegetated soil	k/l	*V*	<0	<0	>0.3

The actual possibility of identifying and distinguishing the four land cover classes was verified by calculating the values of the three multispectral indices for surfaces with known characteristics. These surfaces were mapped by the combined use of VHR images taken on the 14th of February 2020 and geo-located pictures. In detail, by reporting the point of geo-located pictures on the VHR images, it was possible to draw polygons, associated with one of the four land cover classes. In this way, a manually generated ground truth is obtained that was used to construct Figure 8 and validate the results in the next paragraph.

The results displayed in Figure 8 show that for S2 data, pixels with positive *NDWI* values can be exclusively associated with the *W* class. For L8 data, pixels with positive *NDWI* values can be mostly associated with the *W* class, with a limited superposition with the *M* class. Pixels with positive *MNDWI* values can be only associated with the *W* and *M* classes. Pixels with negative *MNDWI* values can be associated with the *V* and *S* classes. Despite small regions of superposition, the *MNDWI* seems to be able to discriminate the four classes. Pixels with values of *NDVI* greater than 0.3 represent areas with a significant presence of vegetation and can be mostly associated with the *V* class. In the case of *NDVI*, the separability of classes is limited. In particular, the *S* and *M* classes are hardly separable with the exclusive use of the *NDVI*.

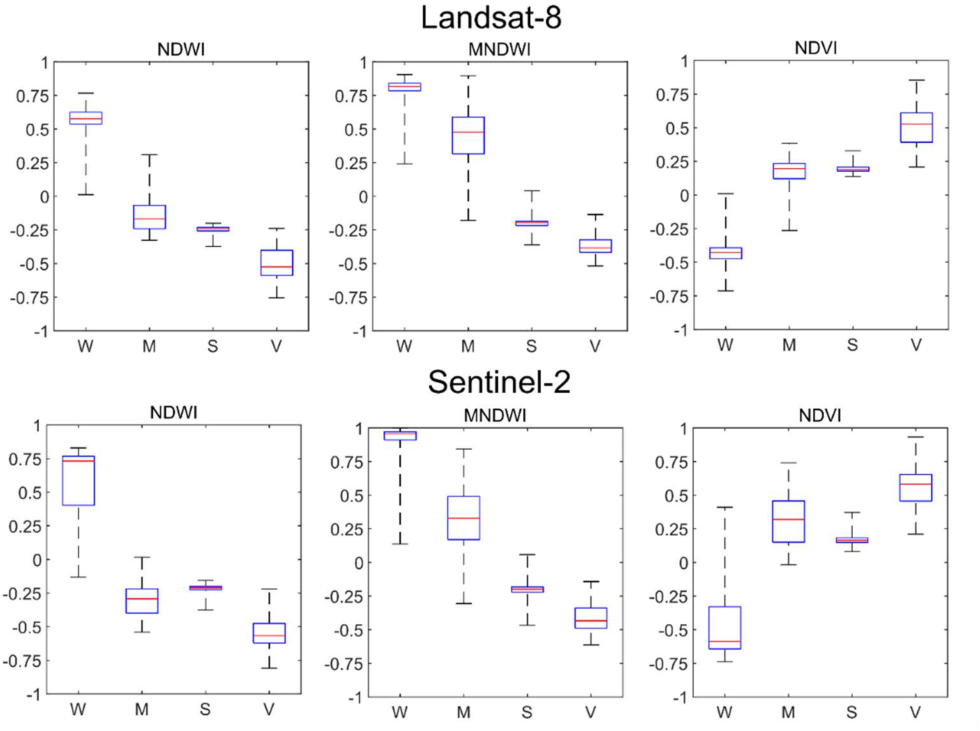

Figure 8:Distribution of multispectral indices values for the four land cover classes (W, M, S, V).

4.3 Performance estimation: rule-base classification methods vs VHR images and field surveys

In order to validate the results of the land cover classification method, the classification obtained from the S2 and L8 images with the evidence extracted from the VHR images, and the field data were compared. Given the slow dynamic of the flooding, the scene can be assumed unchanged in a time interval of a few days. Accordingly, a comparison between acquisitions with up to three days of time-lapse can be considered acceptable. Such an approach led to defining 6 test cases. The acquisition dates of the S2, L8, VHR images and field campaigns, of the 6 tests, are shown in Table 6.

Table 6: Acquisition dates of the VHR images and field survey used for the validation tests.

Case n°	Sentinel-2	Landsat-8	Very high-resolution image	Field survey	Spatial coverage VHR images
1	15/02/20	13/02/20	14/02/20 GeoEye-1	14/02/20	160 km^2- see Figure 9a
2		06/02/20	-	05/02/20	
3	01/01/19	02/01/19	02/01/19 GeoEye-1	-	43 km^2
4	28/10/18	-	25/10/18 WorldView-4	-	28 km^2
5	12/03/18	-	13/03/18 WorldView-4	-	22 km^2
6	21/01/18	22/01/18	20/01/18 GeoEye-1	-	37 km^2

Given the different types and consistencies of the data available on the various cases listed in the Table 6, it was necessary to use three different validation approaches. In particular, (i) a pixel-based comparison was employable for case-1 where both the VHR images and field pictures were available, (ii) an object-based comparison was possible for case-2 by using only field data as the ground truth, and (iii) a more qualitative visual comparison was possible for the cases in which only VHR images were available (cases 3, 4, 5 and 6). As anticipated in the previous paragraph, the points of the geo-localized images were reported on the VHR images, and the polygons associated with one of the four land cover classes were drawn. This approach could only be used in case-1, when the contemporary acquisitions of VHR and ground pictures were available. Consequently, in case-1 it was possible to carry out a quantitative, pixel-based, accuracy estimation by the computation of the confusion matrix for a multi-class classification (Story 1986). The performances are assessed through the number of *True Positives* (*TPi*), *False Positives* (*FPi*), *True Negatives* (*TNi*) and *False Negatives* (*FNi*) for the i-th class (*W*, *S*, *V* or *M*), computed as follows:

$$TP_i = C_{ii} \tag{4}$$

$$FP_i = \sum_{l=1}^{n} C_{li} - TP_i \tag{5}$$

$$FN_i = \sum_{k=1}^{n} C_{ik} - TP_i \tag{6}$$

$$TN_i = \sum_{l=1}^{n}\sum_{k=1}^{n} C_{lk} - TP_i - FP_i - FN_i \tag{7}$$

Where C_{lk} is the generic confusion matrix element, the index l relates to the ground truth and the index k refers to the predicted classification. *Overall Accuracy, Precision (P_i)*, *Recall*(R_i) and *F1-score ($F1_i$)* were than computed by:

$$Overall\ Accuracy = \frac{\sum_{i=1}^{n} C_{ii}}{\sum_{l=1}^{n}\sum_{k=1}^{n} C_{lk}} \tag{8}$$

$$P_i = \frac{TP_i}{TP_i + FP_i} \tag{9}$$

$$R_i = \frac{TP_i}{TP_i + FN_i} \tag{10}$$

$$F1_i = 2 * \frac{P_i * R_i}{P_i + R_i} \tag{11}$$

The rule-based classification method was applied separately to the L8 image of 13th February 2020 and the S2 image of 15th February 2020, and the results were compared to the ground truth generated by the combination of ground pictures and VHR image.

For case-2, an object-based comparison between the predicted L8 classification in a specific area and the land cover shown in the ground pictures for the same area were performed. In case-2, the acquisition points are concentrated inside the *Tancats* (see Figure 6), where water is almost always present in this period (*W* and *M* classes) and not enough points are available for the other two classes (*S* and *V*). For this reason, the comparison with the ground truth was made only for *W* and *M* classes. A two classes confusion matrix was computed, and the classification metrics were then estimated by equations (8 ,9 ,10 and 11). The quantitative pixel-bases validation approach was implemented in an original code in Matlab.

4.3.1 Quantitative pixel-based validation approach: case-1

For a pixel-based comparison, case-1, 95 polygons of known soil cover classes were drawn for 1136 km^2, of which 675 km^2 in *W* class, 165 km^2 in *M* class, 147 km^2 in *S* class and 150 km^2 in *V* class. The ground truth in *W* class turns out to be larger than the others. This occurs because this class had a greater spatial extension than the others. In Table 7 and Table 8 the confusion matrices for the S2 and L8 classification are reported.

Table 7: Confusion matrix between predicted S2 classification and ground truth.

		Predicted condition				
		W	***M***	***S***	***V***	***TOT$_{pixel,i}$***
True condition	***W***	6691	54	2	0	6747
	M	3	1602	25	17	1647
	S	0	1	1468	2	1471
	V	0	0	72	1429	1501
					TOT$_{pixel}$	11366

Table 8: Confusion matrix between predicted L8 classification and ground truth.

		Predicted condition				
		W	***M***	***S***	***V***	***TOT$_{pixel,i}$***
True condition	***W***	744	0	1	0	745
	M	25	145	6	1	177
	S	0	2	166	1	169
	V	0	0	9	166	175

					TOT_{pixel}	1266

It is worth noting that the pixels' number in ground truth classes was different for L8 and S2 because of the different spatial resolutions of the two datasets. In both the L8 and S2 cases, the confusion matrix was almost diagonal showing that the rule-based classification method is efficient and reliable. The overall accuracy resulted very high for both datasets and, in particular, is 0.985 for S2 and 0.965 for L8. In Table 9 and 10, the most relevant performance metrics are presented for S2 and L8 respectively. The precision was always higher than 0.9 with minor differences between the classes: the *W* class is identified with the highest precision while the *S* class is identified with the lowest one. The recall is higher than 0.950 for all the classes except for the *M* class derived from L8 for which the lowest metrics is obtained (0.819). Similar results are obtained for the F1-score that is always higher than 0.950 except for the *M* class of L8 for which it is 0.895.

Table 9: Performances metrics estimated for S2 land cover classification.

	W	M	S	V
Precision	1.000	0.967	0.937	0.987
Recall	0.992	0.973	0.998	0.952
F1 -score	0.996	0.970	0.966	0.969

Table 10: Performances metrics estimated for L8 land cover classification.

	W	M	S	V
Precision	0.968	0.986	0.912	0.988
Recall	0.999	0.819	0.982	0.949
F1 -score	0.983	0.895	0.946	0.968

4.3.2 Quantitative object-based validation approach: case-2

In case-2, field data were available, but VHR images were not, and the metrics were computed with the object-based procedure as introduced in §4.3. It is worth noting that, in case-2, only the L8 image was available due to the absence of cloud-free S2 acquisition close enough in time. As specified above, in case-2 only the two classes (*W* and *M*) confusion matrix were computed. Of the 18 ground objects, one was excluded because it was in the S class, 8 were correctly classified in *W*, 8 were correctly classified in *M* and only one object of the *M* class was wrongly classified in *W*. The overall accuracy resulted in 0.941. The F1-score resulted in 0.947 for both the *W* and *M* classes. Albeit with a small number of comparisons, the estimated performances confirmed the previous paragraph evaluations (case-1).

4.3.3 Qualitative validation approach: case-3

The qualitative comparison between predicted land cover and VHR images was performed for all the cases in which VHR images were available (see Table 6). For the sake of brevity, in this paragraph only two examples were reported, and in particular case-1 and case-5. Figure 9 displays an overview of the Albufera wetland, in particular, it shows the RGB GeoEye-1 image acquired on 14th February 2020 along with the land cover maps derived from the S2 of the 15th of February and the L8 of the 13th of February. These images show the Albufera wetland in the drying phase, a typical situation at the end of the winter flooding. In this period, several *Tancats* are still flooded and placed in the *W* class while some fields are drying up and partially or completely in the *M* class.

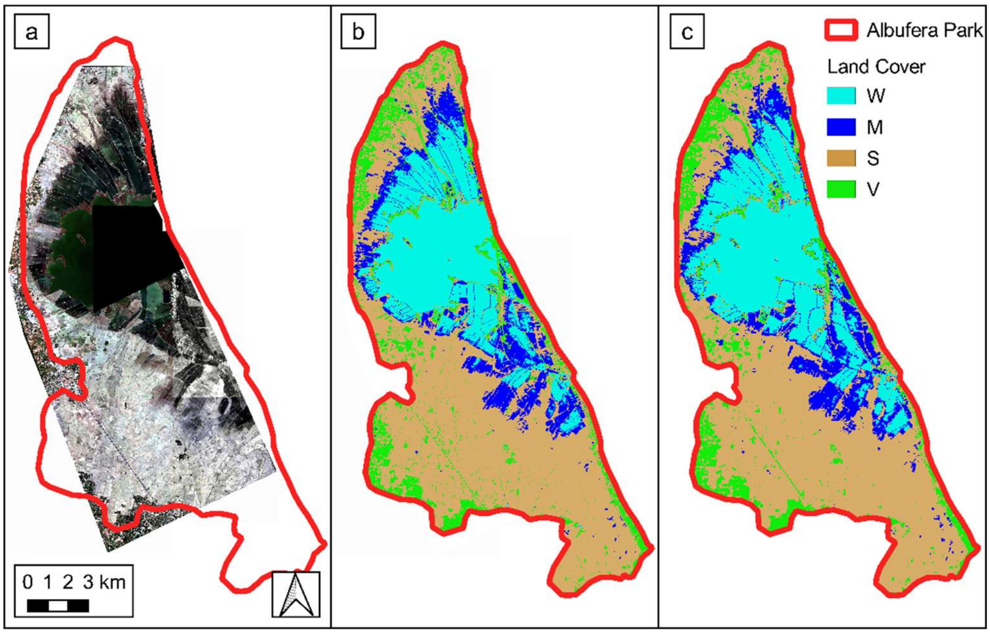

Figure 9: (a) RGB GeoEye-1 of the 14th February 2020 provided by ESA (© TPMO 2020); (b) Land cover classification extracted by S2 image of the 15th February 2020; (c) Land cover classification extracted by L8 image of the 13th February 2020.

Figure 10a reports a detail of the Figure 9 for S2 land cover classification in the northern portion of the Albufera Park for case-1. The Figures 10b are zoomed sub-panels of the same map that are compared with the corresponding panels of the VHR image (Figures 10c) and with ground pictures (Figures 10d and Figures 10e). In Figure 10.1, an example of an area classified as "*open Water*" (*W*) is presented. The peculiar characteristic of the *W* class is the presence of water depths higher than about 20 cm. In this condition, the post-harvest rice plants, if present, are mostly submerged and the surface layer of water is characterized by low turbidity. Therefore, the rice fields are represented as a water body similar to the Albufera lake. As an example, the land cover classification, reported in Figure 10.1b, is in perfect agreement with the VHR (Figure 10.1c) and the geolocated ground picture (Figure 10.1d). The classification of Figure 10.2b shows a patches of *Mosaic water* (*M*), *Bare soil* (*S*) and a small *Vegetated* area (*V*). The *M* class, frequently encountered at the boundary of the flooded area, is characterized by shallow water depths or a combination of water, mud and vegetation. Regions with ponds smaller than the resolution cell also fall into this class. The *S* class includes both dry and wet soil as the classification method could not distinguish the two. Looking at the picture of Figure 10.2.d, it is possible to note an area (*M1*) with very shallow water that was correctly classified as the *M* class. In the picture of Figure 10.2.e, bare soil (locations *S1* and *S2*) was present in the foreground. In addition, a small, isolated pond (*M2*) is also visible in the background. All these areas were correctly classified in their relative classes. It is worth noting that the classification could detect the presence of very shallow water (with depth of few centimeters), pointing out the distinction between *M* and *S* which is very well demonstrated by Figure 10.2b,e.

Figures 10.3 and 10.4 display a composite of *S* and *V* classes. Also in these cases the classification method responded confidently and could detect the vegetation patchiness. The Figure 10.5 shows how the method could detect the presence of water mixed with the dry stalks of the cut rice and to associate this area with *M* class. The adjacent area, in which the water level was higher and there were not stalks emerging from the water surface, was correctly assigned to the *W* class.

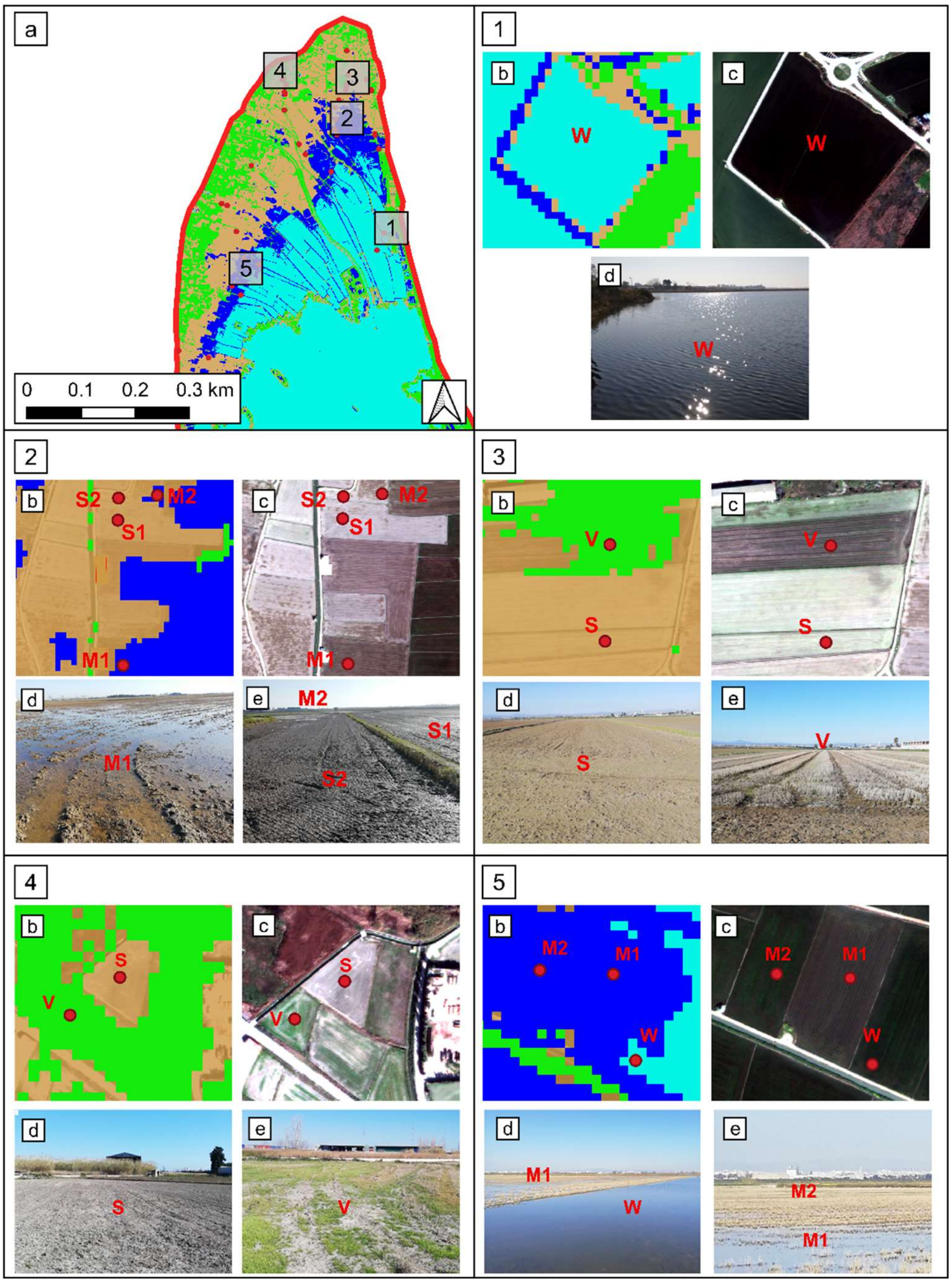

*Figure 10: (**a**) Land cover classification extracted by S2 image of the 15th February 2020 with field surveys locations of the 14th February (points) and the position of the frames displayed with larger scales in the panels 1,2 3, 4 and 5; (**b**) zoom of land cover classification; **c**) zoom of the RGB GeoEye-1 (© TPMO 2020) of the 14th February; (**d**) and (**e**) ground pictures taken on the 14th February.*

The comparison between the classification obtained from the S2 image of 28th October 2018 and the GE-1 VHR image of 25th October 2018 is presented in Figure 11. The *W*, *M*, *S* and *V* classes appear congruent with what can be deduced from the VHR image.

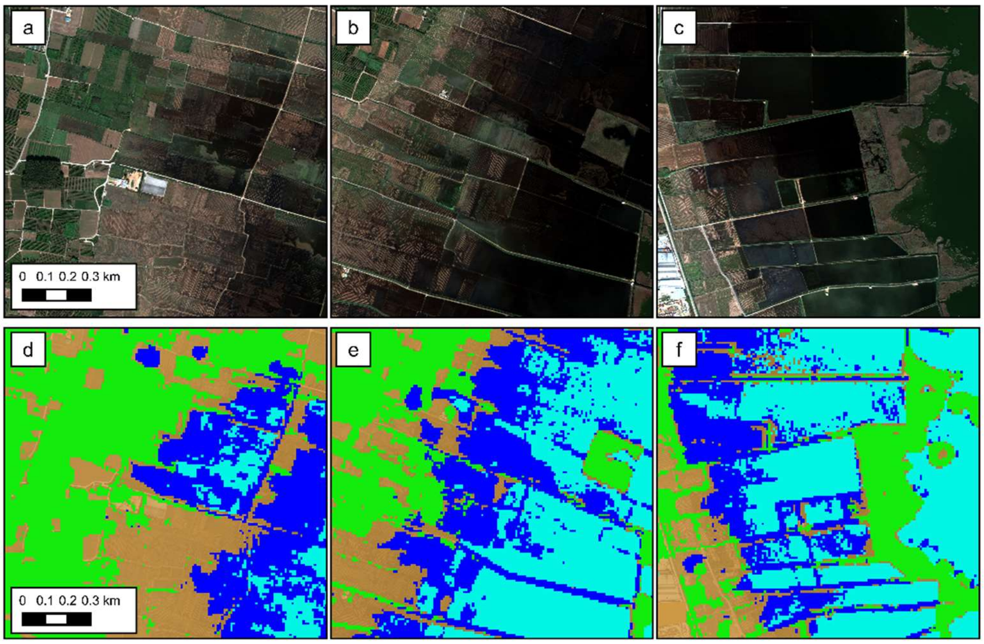

Figure 11: Comparison between GE-1 VHR of 25th October 2018 (a–c) and land cover classification extracted by S2 image of 28th October 2018 (d–f).

4.4 Consistency check between the Landsat-8 and Sentinel-2 datasets

In order to reduce the revisit time and consequently increase monitoring temporal continuity, the information acquired from the L8 and S2 data were joined. To evaluate the consistency between possibility of jointly using L8 and S2, the coherence of the land classification obtained separately by the two datasets was checked. A first confirmation occurs in the previous paragraph, the consistency between the classifications made with L8 and those made with S2 is indirectly verified by the comparisons made in case-1. In case-1, the classifications obtained from two images, one L8 and one S2, close in time, were separately compared with the ground truth, giving satisfactory results for both.

Further verification was obtained from direct comparisons between the L8 and S2 cloud-free images acquired on the same day. With this aim, the S2 and L8 cloud-free images, acquired in the same days, were selected. In the observation period, there are six contemporaneous S2 and L8 acquisitions. For this analysis, the L8 were resampled at the same resolution of the S2 images (10 m) using a bilinear interpolation algorithm within Orfeo-ToolBox (OTB). The performances were estimated by comparing, each pixel of the so-called predicted condition (L8) with the so-called truth condition (S2). After computation of the confusion matrix, the Overall Accuracy, Precision, Recall and F1-score were estimated with the equations (8, 9, 10 and 11, in §4.3).

Table 11 reports the resulting performance metrics. The Overall Accuracy ranges from 0.85 to 0.94. The F1-score is always very high (between 0.93 and 0.98) for the *W* class and is extremely variable for the *M* class. The value of the F1-score is particularly low in the *M* class for the acquisition of October, November and end of March. In these periods of the year, the presence of water is mainly limited to the Albufera lake and to small, scattered areas. The portion of pixels classified in the *M* class by S2 in these dates are only 0.3% on the 8th October 2019; 0.4% on the 27th March 2018 and 6.5% on the 12th November 2017. A high fragmentation of areas with ponds or shallow and turbid waters occurs. In this situation, due to the higher resolution of S2 images, it is some-times possible to distinguish single pixels or small groups of pixels that are in the conditions *M*, *S* or *V*. Differently, L8 images, characterized by lower spatial resolution, tend to return more frequently the *M* class which is intrinsically a mosaic of patches. This impacts the precision, and consequently the F1-score of the classification for the *M* class in these dates. The comparison made in the flooding period between December and March gives, for the *M* class, higher classification performances (F1-score between 0.8 and 0.87). This is also coherent with the high performance obtained in the ground truth check of case-1, performed on 15th February and 13th February. The performance of *S* and *V* are less variable in time; the F1-score is between 0.75 and 0.93 for the *S* class and between 0.84 and 0.94 for the *V* class. The confusion matrixes showed that L8 places in the *V* class some pixels labelled by S2 as the *S* class. This is the main source of discrepancy between the results of S2 and L8 for the *S* and *V* classes.

Table 11: Performances metrics estimated for "predicted" L8 indices compared with "ground truth" S2 indices.

Date	F1 -score				Overall Accuracy
	W	M	S	V	
17 March2017	0.983	0.869	0.931	0.813	0.912
12 November/2017	0.941	0.572	0.875	0.787	0.853
31 January 2018	0.937	0.847	0.882	0.821	0.884
27 March 2018	0.984	0.552	0.964	0.811	0.944
08 October 2019	0.980	0.350	0.828	0.835	0.848
27 December 2019	0.931	0.796	0.755	0.808	0.848

The L8 and S2 consistency can also be assessed by comparing the temporal trends of the surfaces, represented in km^2, for the different classes. In this way, a cross-check with the daily tests described above is also possible and the impact of seasonality can be further assessed. An example is reported in Figure 12, where the temporal trend of land covers extracted from L8 is compared with the same trends extracted by S2 for 2019/20. On two dates of this period, L8 and S2 were acquired the same day (08th October 2019 and 27th December 2019, shown in Figure 12 as 08/10 and 27/12). A good agreement between the flooding dynamics (*M* and *W* classes) extracted by the two datasets is shown (Figure 12a). In September and October, the *W* area almost corresponds with the Albufera lake, and the *M* area is negligible. The L8 and S2 trends are similar even if the F1-score resulted very low for the *M* class on 8th October (see Table 11). The increasing and decreasing trends of the following months are also similar, and this shows that the good performances found for 27th December are stable over time. Figure 12b indicates that the *V* class mapped by L8 is sometimes more extended than the S2 one (e.g., on 08th October), while the opposite occurs for the *S* class.

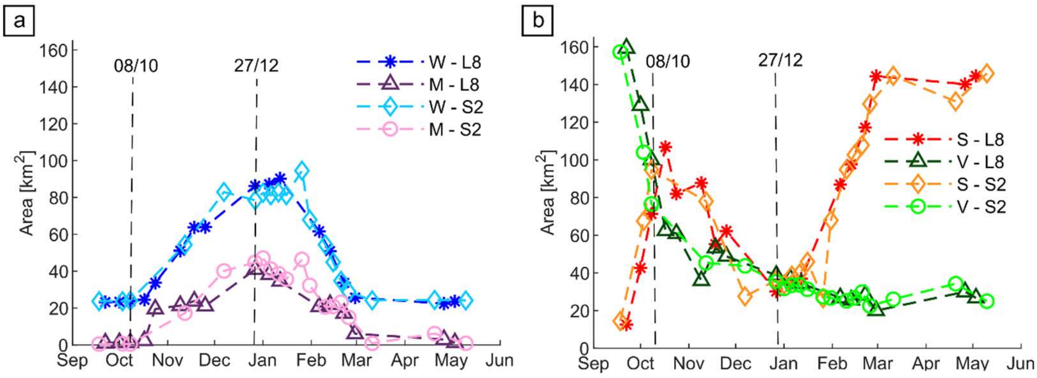

Figure 12: Extent of W, M, S and V areas extracted by Landsat-8 and Sentinel-2 in 2019/2020.

The joint use of the two datasets offered excellent advantages in terms of reducing the revisit time. For the study area, the L8 archive contains a total of 166 images with an average revisit time of about 8 days from September to April in the observation period (2013-2020). Due to the presence of the cloud cover, only 81 images with an average revisit time of 18 days were actually employable. The longest time interval between two cloud-free images was 57 days. In the S2 archive, a total of 175 images was available, with an average revisit time of about 10 days between 2015 and 2017 and 5 days between 2017 and 2020. Due to the presence of the cloud cover, only 69 images with an average revisit time of 16 days were actually employable. The longest time interval between two cloud-free images was 120 days. In the period covered by both missions (2015-2020), the integration of the two datasets led to an effective average revisit time of 7 days. In addition, the longest time interval between two cloud-free images dropped to 16 days. As an example, the revisit time of the separated and merged datasets in 2019 are shown in Figure 13.

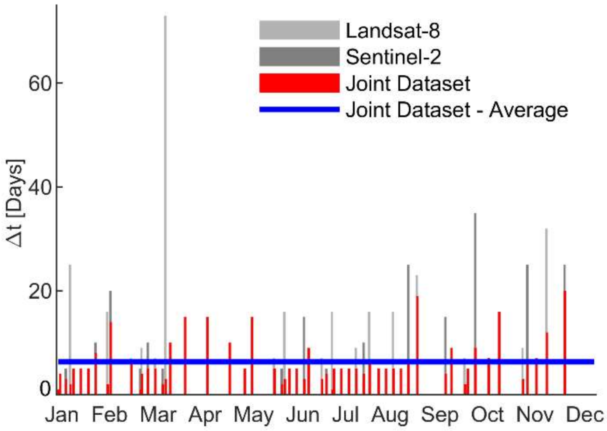

Figure 13: Number of days between two free-cloud images of the L8 and S2 datasets used separately and of the merged dataset in 2019.

4.5 Winter flooding duration map

The winter flooding duration is a key piece of information to evaluate the habitat availability for water-related animals and plants. Given the varied management of the wetland by farmers, this duration varies from point to point and can be represented with a raster map showing, for each pixel, the number of days in which the corresponding surface was covered with water. To this purpose, an original Python code was implemented, which allowed for a temporal gap-filling first on the *MNDWI* and *NDWI* maps, and subsequently the rule-based classification method was applied to identify the *W* and *M* classes. The linear temporal gap-filling proposed by Inglada et al. (2015) was used. This method has the advantage of being easily implemented and more robust than higher-order models. The temporal gap-filling is obtained by:

$$\hat{I} = \frac{\Delta_+}{\Delta_- + \Delta_+} \cdot I_- + \frac{\Delta_-}{\Delta_- + \Delta_+} \cdot I_+ \tag{9}$$

where Iˆ is the estimated value of the multispectral index (i.e., *NDWI* and *MNDWI*) at specific date, I_and I_+ are the previous and the subsequent available values, and Δ_ and Δ_+ the left and right temporal gaps.

The gap-filling was separately performed on the S2 and L8 datasets to obtain two separate daily series of indices values. For each day, the closest S2 or L8 acquisition was identified, and the corresponding synthetic map included in the merged series. When the acquisitions S2 and L8 are contemporary, the S2 series is preferred. The rule-based classification method is then applied to all the maps of the merged series to identify the *W* and *M* classes.

Figure 14 shows the winter annual flooding trend, from September to April, outside the rice growing period, for the seven years of observation. In addition to the areas in open water conditions (*W* class), Figure 14 also shows the overall area in which water was present (*W* + *M* classes), even if with small depths or in a spatially discontinuous way. The time evolution of the *W* area shows similar trends in the different years (Figure 14a). There is an enlargement period in autumn, a maximum extent of around 80 km^2 (almost the area of the lake plus the area of the *Tancats*) in December and January and a progressive reduction until March. In September and March, the flooded area is around 24 km^2 that is the area of the Albufera lake. In some years (2015/16 and 2018/19), the flooding started earlier than other years (at the beginning of October) and had a longer duration. 2013/14 was the year with the shorter duration of the flooding that was already over by 12th February.

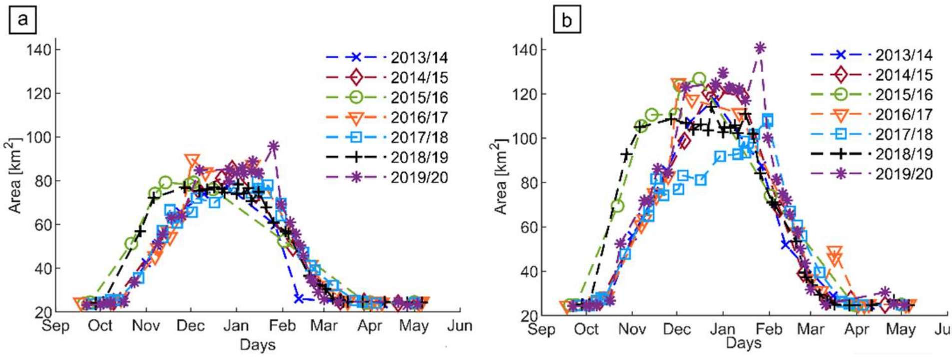

Figure 14: (a) Temporal trend of area in W class (open water); (b) temporal trend of area in W or M class (open water or mosaic of water, mud and vegetation).

The overall extension of the *W*+*M* area showed a similar trend of the *W* one, but with more pronounced variations between different years (Figure 15b). The maximum extent of around 120 km^2 was not reached every year, but the area always exceeded 100 km^2. The duration and seasonality of the *W*+*M* flooding varied from year to year.

Once the *W* and *M* maps have been extracted, the number of days, in which the *W* or *M* class was present, is finally computed on a pixel basis.

Figure 15a shows the number of days in which open water (*W* class) is present. Figure 15b shows the days in which water is present in any condition, even if in shallow layers or discontinuous patches (*W* class plus *M* class).

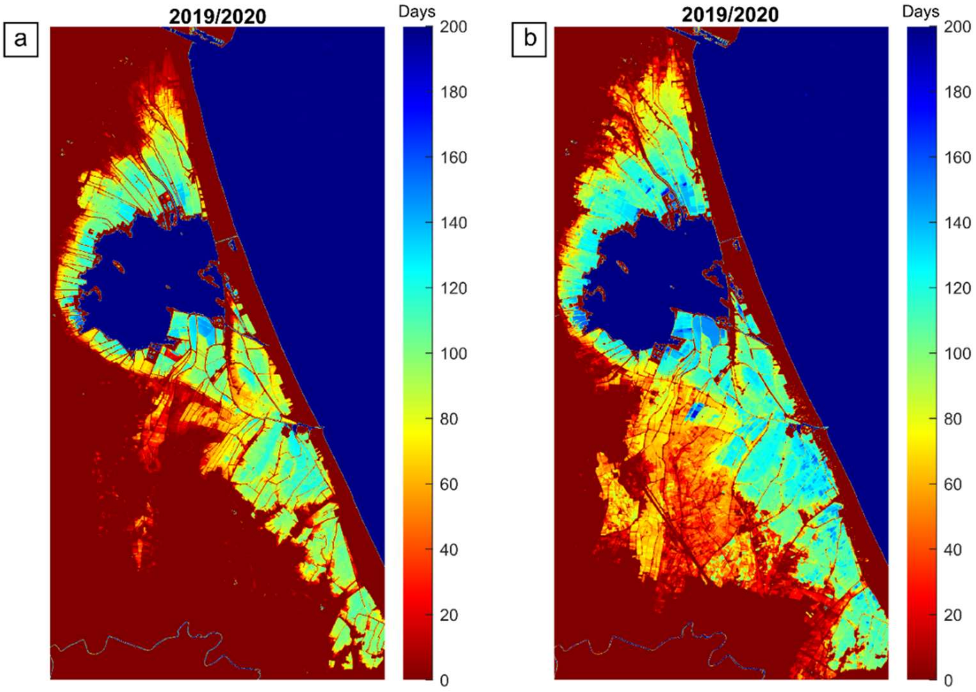

Figure 15: Days of water presence from October to April in 2019/20; (a) W class; (b) W class plus M class.

The average duration of open water presence in the *Tancats* and the highlands, in the winter period, is reported in Figure 16. The *Tancats* are flooded for a period between two and three months depending on the year in question, while the highlands are flooded for shorter periods (around 20 days). The overall presence of water lasts longer. The period with the presence of either the *W* or *M* class in the *Tancats* is in the range of three or even, in some years, almost four months. In the highlands, these conditions last about 40 days except in 2017/18.This effect can be explained by the particular weather conditions during the winter in the Mediterranean coast. In this area, it is normal to have cold front events with rainfall up to 200 mm in less than 48 hours. These storms produce local floods in areas with worse drainage, sometimes correlated to traditional natural springs (named locally "*ullals*") with higher water tables. The 2017/2018 winter was particularly dry, without any cold front event, which can explain the reduction of water in the highlands.

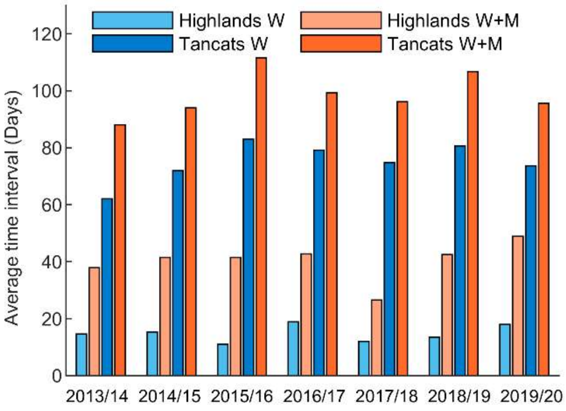

Figure 16: Average number of days of water presence in W and W + M classes, in the Tancats and in the highlands.

Figure 17 shows an example of the spatial distribution and temporal dynamic of the land cover of February 2020. The areas of the four classes *W*, *M, V* and *S* are mapped. Figure 17 depicts the drying phase. The area initially in *W* conditions progressively empties, for some time there is still a residual water cover (*M* class) and finally dries-up completely. The duration of the drying phase varies in space. In the areas further away from the lake, the *M* conditions are prolonged for longer times.

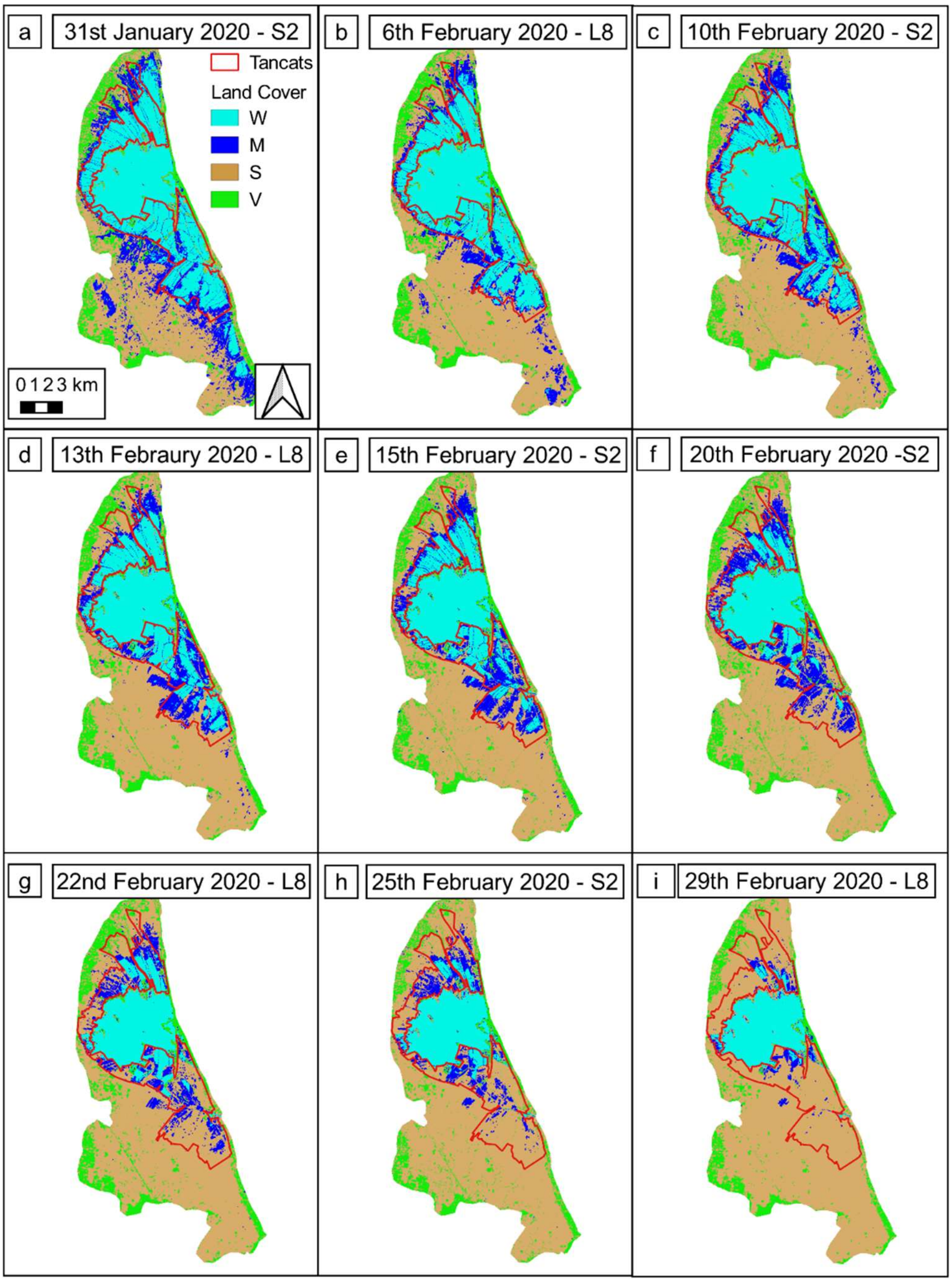

Figure 17: Maps of land cover classes in February 2020 obtained by L8 and S2. The continuous line is the boundary of Tancats area.

4.6 Discussion

The classification of wetland land cover from remote sensed data is particularly complex due to the large spatial and temporal variability of water depth, water turbidity, floating or emerging vegetation, growth and harvest of crops (Ozesmi. and Bauer 2002). Supervised methods algorithms have been implemented with good results for wetland land cover classification (Rebelo et al., 2009, Munyati et al., 2000, Yang et al., 2005). In some cases, various land cover classes were identified, as in the present chapter. For example, Dronova et al. (2011), mapped four land cover classes with an object-based supervised procedure. The application of supervised methods seems to be limited due to the lack of local training datasets. Very high-resolution images, apart from their limited availability, do not provide reliable ground truth because the interpretation of the land covers is uncertain, especially when plants are growing into the water or at the edges of submerged areas. To obtain reliable training samples, it is necessary to support the interpretation of high-resolution images with field surveys. Nevertheless, extensive field data collection is limited in number since they can be expensive and time consuming. Unsupervised methods algorithms do not have these limitations and are generally characterized by higher transferability and therefore can be implemented with less effort in different locations.

In this case study, a straightforward and easily applicable unsupervised, rule-based classification algorithm for land cover classification in wetlands exploiting S2 and L8 datasets was employed. The method is based on the combined use of three multispectral indexes (*MNDWI*, *NDWI*, and *NDVI*) and can be easily implemented by technicians and water managers using common GIS platforms. Another significant advantage of the proposed method algorithm is the possibility of distinguishing four land cover classes that are relevant for the evaluation of habitat availability for water-related animals and plants. The open water (*W* class) is distinguished from very shallow water or a mosaic of ponds, vegetation and mud (*M* class). Adjacent non-water environments are also singled out in vegetated land (*V* class) and bare soil (*S* class). After spectral analyses, Amani et al. (2018) concluded that the spectral indices derived from the NIR, RE, and red bands (e.g., *NDWI* and *NDVI*) were the most useful spectral bands for the differentiation of wetland land cover. They also found that SWIR bands helped to discriminate the shallow water class from other wetland classes. In this case study, the distribution of indices values for the four land cover classes (*W*, *M*, *S*, *V*) were computed (Figure 7). The analysis showed that the *NDWI* index is useful to distinguish the open water condition, the *MNDWI* allows to also classify the areas characterized by a mosaic of shallow water, mud and vegetation. Finally, the *NDVI* index allows to distinguish the bare soil from the vegetated one. Therefore, the proposed combination of these indices in a rule-based classification algorithm enhances the discrimination properties and reduces the ambiguity of each index. Amani et. al. (2018) pointed out that the SWIR band is sensitive to the moisture content in soil and vegetation. This could lead to possible misclassification between wet soil and shallow water conditions. However, this aspect was not observed with the indices combination proposed in this work (see Figures 8 and 10 and Tables 7 and 8). Considering the significant spatial and temporal variability of the humidity conditions, further analysis, at different times of the year, could help to bring out the possible occurrence of misclassification at particular times or location.

The availability of ground truths is important to relate remote sensed data to real features and the correct land cover on the ground. Undoubtedly, the most stringent validation test for the proposed unsupervised classification algorithm was the pixel-based one (case-1) in which the ground truth was obtained by the contextual use of geo-located ground pictures and VHR images. The Overall Accuracy resulted very high for both datasets (0.985 for S2 and 0.965 for L8). The F1-score values were, 0.996 (0.983) for the *W* class, 0.970 (0.895) for the *M* class, 0.966 (0.946) for the *S* class, 0.969 (0.968) for the *V* class. The L8 results are reported in brackets next to the S2 ones. The identification of the *M* class is the task with the most significant difference between the S2 and L8 metrics (difference between a F1-score higher than 0.02). The slightly lower performance of the L8 data in the *M* class identification could be due to the lower spatial resolution of the L8 images, which had the greatest impact when the patchiness of the land cover features was higher, as in the *M* class. Further differences can be due to the slightly different frequency bands acquired by the two sensors. This point was further investigated by comparing the L8 and S2 images acquired the same day, which is discussed below.

The same ground truth data of case-1 was also used for a visual inspection of the results (see the examples reported in Figure 10). This analysis showed how the method could discriminate surfaces with similar characteristics, such as humid soil and isolated ponds of water. Since wetlands are highly variable over time, with a seasonal regime, it was necessary to verify the performances of the classification tool throughout the year. This was done through qualitative validation tests of cases 3, 4, 5 and 6. These validation tests confirmed the high classification capacity of the method and allowed to assess that the results are stable regardless of the particular conditions of the day of acquisition.

The revisit time of the multispectral imagery can be highly impacted by the possible presence of cloud cover. In order to mitigate this problem, the two S2 and L8 datasets were combined. In this way, the average revisit time between two cloud-free images dropped from 18 and 16 days of the L8 and S2 separate datasets to 7 days of the merged dataset. The possibility of integrating the two datasets was investigated by Mandanici and Bitelli (2016). They performed tests on images acquired with a time gap lower than 20 min and demonstrated a good correlation between the corresponding bands of the two sensors. However, the radiometric characteristics of the two sensors were not identical. The authors suggested evaluating the impact of such discrepancies for each specific application, depending on the adopted methodology and the aim of the study. In this work, as already specified in §2.2.2, with the object of providing a tool extremely easy to apply, the two datasets were separately processed, and the land cover maps were obtained independently for the S2 and the L8 datasets. To verify the validity of this approach, it is sufficient to verify the coherence between the classifications results obtained by the two datasets. The direct comparison of the land cover classification, derived from S2 and L8 acquisitions made in the same days, showed satisfying coherence (Overall Accuracy between 0.84 and 0.94). The detailed analysis of the performances for the different classes, showed that, when the flooding is scarcely present and scattered, pixels classified by L8 as the *M* class were placed by S2 in other classes. This is probably due to the lower spatial resolution of L8 which induces a sort of spatial average thus shifting the response towards classes characterized by higher patchiness (i.e., the *M* class). Another small discrepancy was found between the V and S classes. In particular, L8 tended to classify as *V* class pixels what S2 classifies as the *S* class. These discrepancies may be adjusted by calibrating the threshold of the *NDVI* index separately for the L8 and S2. A further confirmation of the overall coherence between S2 and L8 classifications is reported in Figure 12, showing that the temporal trends of the estimated area in different classes are similarly estimated by the two datasets. This result is particularly significant because it shows how, despite the high dynamism of the wetland context, the coherence between the two datasets was relatively stable over time.

The possibility of mapping the four classes and spatially quantifying submerged areas (*W* and M classes), showed interesting aspects of the hydrometric regime of the Albufera wetland. The spatial extension of the *W* class has an approximately constant trend from year to year, while the surface in the *M* class is more variable (see Figure 14). This can be explained by the fact that the surface classified by the *W* class is influenced by agricultural practices. The farmers can dry the rice fields easily and quickly by using pumps and opening the gates that connects the rice fields to the lake. The moment in which the rice fields are dried up is decided by the irrigation communities and is relatively constant throughout the years. The variability of the *M* class over time can be explained by factors that may not depend on only irrigation and agricultural practices. A mosaic of water, mud and vegetation (M class) can be observed also after intense precipitation or generated by high evapotranspiration.

Land cover maps, such as those shown in Figure 17, can be very useful for observing in detail the spatial distribution of the land cover and its evolution over time. For example, in 2020, the *Tancats* were flooded with high water depth in January and started emptying from the middle of February. In the southern area, the water depths started decreasing first and lasted until the end of February. While in the northern portion, the decrease began later and was more rapid. This is probably due to the different ways in which the emptying is carried out as pumps are sometimes used to accelerate the drying up in the *Tancats* near the lake, while in the areas further away from the lake, the process takes place more slowly. Maps similar to the one of Figure 15 can be produced for all the years of observation and allow for detailed and continuous monitoring. The difference between the duration of the *W* and the *M* conditions is particularly evident in the highlands. The occasional and sparse presence of the *M* condition for short time intervals, as shown in Figure 15b, can be due to rainfall events and can be independent of the artificial management of the wetland.

The joint use of the two multispectral datasets provided the advantage of reducing the revisit time. Obviously, a further reduction of the review time could be obtained from the joint use of SAR and multispectral data. SAR data in addition to reducing review times could provide further contributions. For example, multispectral data provide little information on the physical characteristics of vegetation, such as morphology and height (Gallant 2015, Mahdavi et al., 2018). Furthermore, their depth of penetration is low, and detection of water under trees/dense vegetation is not possible. Due to the disadvantages, the use of multispectral sensors alone is not sufficient in some applications. An interesting continuation of this work could regard the extension of the monitoring period to the rice growing season. During the period from May to September, the multispectral data identify the presence of water only during the first month (May), because when the plant reaches a certain height, the multispectral data are not able to discriminate the presence of water because this is clouded by rice cultivations. One recent work (Vera-Herrera et al., 2021), carried out on the Albufera wetland, has estimated the presence of water under the rice fields, assuming as a hypothesis that the fields are always and constantly flooded during the cultivation period and that therefore the extension of the flooded areas coincides with the extension of the rice fields. Unfortunately, this hypothesis cannot be taken into consideration because the rice fields, in some circumstances, can be periodically drained and then irrigated by the farmers. The field surveys carried out during the month of July 2019, on the Albufera wetland, confirmed that on some fields there was no water under the rice plants (Figure 18).

Figure 18: Photographs of rice fields taken in the Albufera wetland in July 2019

Therefore, in order to determine the presence and duration of flooding under the rice plants, further considerations are necessary. One possibility could be to investigate the potential offered by L-band SAR data, which have a greater ability to penetrate the presence of vegetation and identify the possible presence of water (Martinez et al., 2007).

5. Detection of river hydro-morphological changes: the case study of the Po River (Italy)

This chapter presents an application of satellite monitoring of the hydro-morphological changes in large rivers. For this application, multi-temporal multispectral images, Landsat-4/5, Landsat-8 and Sentinel-2 were used. As a case study, a 40 km lowland reach of the Italian Po River between Boretto and Borgoforte was used. The evolution of the wet channel in the period 1986-2020, and a river restoration work will be presented, to show how the information extracted by satellite data can help in monitoring hydro-morphological changes pre and post-intervention. 288 Landsat-4/5, 136 Landsat-8 and 226 Sentinel-2 free-cloud images were used.

One of the novelties of this work relates to the combination of information extract from several types of sensors, covering a time interval of 35 years with 650 images. To my knowledge, this is the first time that a river has been analysed using the information from all these multispectral satellite sensors. Several past works have integrated data between two satellites or limited the analysis to a small number of images (Jarchow et al. 2018, Billah et al. 2018, Dewan et. al 2017).

Unfortunately, multispectral images are not able to acquire data in the presence of cloud cover, and to further increase the review time, in addition to multispectral sensors, it is possible to use SAR images. §5.9 will illustrate the potential of SAR Sentinel-1 data in monitoring the hydro morphological evolution of the wet channel. Some results presented in this chapter have been published in the Geocarto international journal (Cavallo et al., 2021).

5.1 Case study: the Italian Po River

The Po River is the longest watercourse in Italy (maximum distance 682 km), it originates in the Cozie Alps, flowing eastward across northern Italy for around 651 km, draining a catchment area of approximately 74,091 km^2, and outflowing in the Adriatic Sea (AdbPo 2008) (Figure 19a). During the last centuries, anthropogenic disturbances have significantly influenced its fluvial dynamics. To reduce flood-hazard, some reaches have been confined by the construction of levees and extensive longitudinal bank protection (Domeneghetti et al. 2015). The presence of hydraulic protection works, the extraction of aggregates for civil buildings, mainly in the period 1960–1980, the presence of dams for hydropower production and the construction of wing dykes for navigation purposes have led to a significant oversimplification of the lowland part of the Po River, which changed from pluri- to mono-cursal (Lamberti and Schippa 1994; Surian and Rinaldi 2003; AdBPo 2008; Lanzoni et al. 2015; Maselli et al. 2018). Since the 1980s, the anthropogenic pressures on the Po catchment have been reduced, causing a shift towards quasi-equilibrium sediment conditions: today eroded and deposited volumes of sediment tend to be approximately equal (Castiglioni et al. 1999; Marchetti 2002; Lanzoni et al. 2015). However, despite the reduction of human pressure in the catchment, past channel deepening activities and the presence of wing dykes still determine, in some parts of the river, a single-thread channel able to convene flows of the order of 6000 m^3/s (i.e., high-flow conditions), excluding the secondary channels and therefore causing both an excessive erosion of the river bed and the impoverishment of morphological quality and habitat availability. To counteract these problems, in recent years river restoration measures were implemented for the reactivation of secondary channels during frequent peak flows (namely >1000 m3 /s), to restore the biodiversity and reduce the bed erosion during extreme events (Domeneghetti et al. 2015). The study mainly focuses on a 40 km reach between Boretto and Borgoforte (Figure 19a,b), having an average bankfull width of 200–500 m. Within the study reach, the channel pattern is mainly single-thread with a straight to meandering planform, while point bars, mid-channel bars and chute channels are the most common geomorphic units. The alluvial bed is composed of well-sorted coarse sand with a median size D_{50}=0.4 mm and a sorting of 1.2ϕ (ϕ diameter), (Guerrero et al. 2013; Maselli et al. 2020). The studied reach of the Po River is also part of the Natura 2000 network as a Special Protection Area for Birds (SPA) under the Birds Directive 2009/147/EC (site code ES0000471), and a Site of Community Importance (SCI) under Habitats Directive 92/43/EEC (site code IT20B0501).

The study reach was divided into two sub-reaches, one upstream of the confluence with the Oglio River (Boretto reach) and one downstream of the same confluence (Borgoforte reach). In 2013, just upstream of the Oglio River confluence, a wing dyke was lowered to reactivate the secondary channel on the right (Figure 19c). A downstream 15 km river reach close to the hydrometric station of Ostiglia, having similar characteristics, was also considered, to further validate satellite data against ground-based evidence.

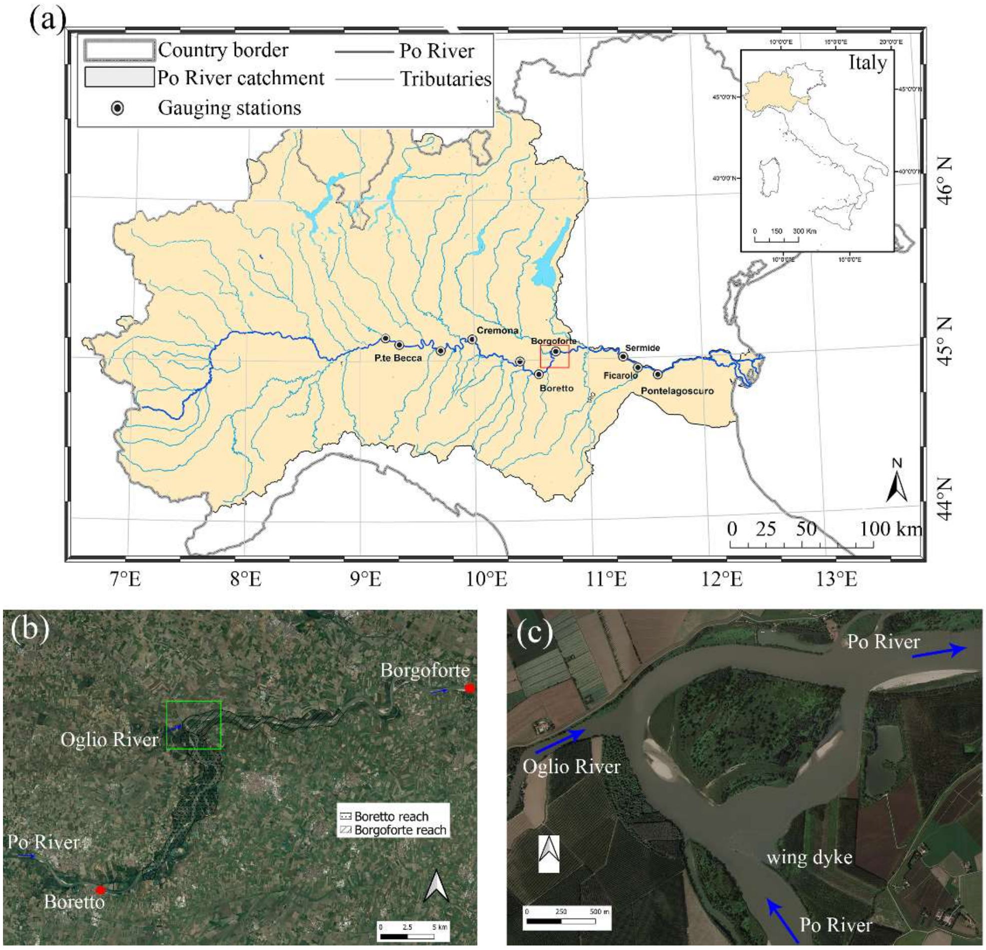

Figure 19: *(a) Location map of the Po River catchment and study area (red rectangle); (b) Boretto and Borgoforte reaches; (c) wing dyke upstream of the confluence between the Oglio and the Po rivers, lowered in 2013 for reactivating the secondary channel on the right side.*

5.1.1 Hydrological data

The hydrological data were extracted from the annals of the "*Agenzia Regionale per la Prevenzione, l'Ambiente e l'Energia dell'Emilia-Romagna*" (ARPAE - arpae.it/it/temi-ambientali/meteo/report-meteo/annali-idrologici), covering the period 1986–2020. It is worth noting that ARPAE measures the water levels at a time interval of 30 minutes, and then derives the daily discharges through a stage-discharge relationship updated once a year. Previous analyses of long-term time-series measurements of discharge along the Po River have shown peak discharge in autumn and spring, generated by rainfall and snowmelt events (Montanari 2012), reflecting the dominant climatic behaviours (Zanchettin et al. 2008). Overall, the study reach exhibits transient hydrology interspersed with discrete, high-magnitude flood events, as also visible from the daily river discharge measured during the period 1986–2020 in two nearby gauging stations (Boretto and Borgoforte) and reported in Figure 20. The Boretto station is close to the upstream end of the study reach and the Borgoforte station is close to the end section of the reach (see Figure 19). During the studied period, the mean daily discharges measured in these stations were about 1,300 m^3/s, with several high-magnitude flood events (>5,000 m^3/s). The largest flood event, which occurred in October 2000, reached 11,500–11,800 m^3/s, and was described as a very significant flood (Castellarin et al. 2011).

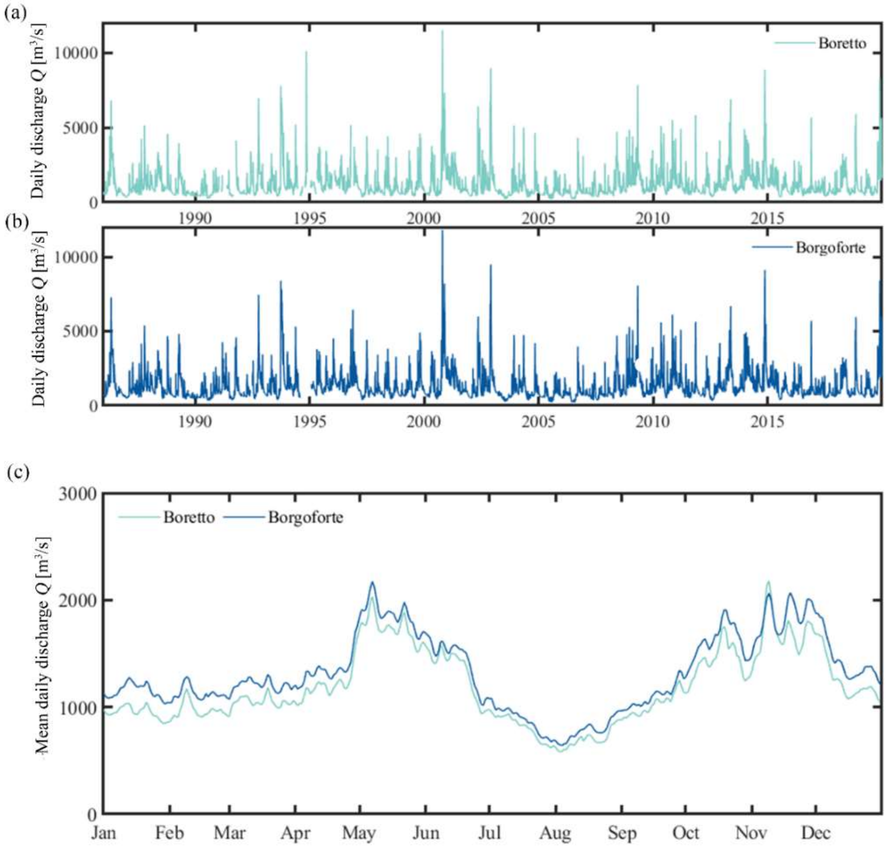

Figure 20: Daily discharge of the Po River measured at the (a) Boretto and (b) Borgoforte gauging stations for the period 1986-2020. (c) The seasonal component of the daily flow.

5.2 Satellite data

In this work, freely available satellite images at a moderate spatial resolution and very high spatial resolution images were used. Among the images freely available online, Landsat-4 and 5, Landsat-8 and Sentinel-2 satellites were used for a multitemporal analysis from 1986 to 2020; and Sentinel-1 images were used to test an automated classification method in §5.9. In addition, multispectral images of the WorldView-02 and GeoEye-01 satellites (see §2.1.5) and images provided by

Google Earth Pro platform with a very high spatial resolution (about 0.50 m) were used, as the ground truth, to validate the results of the classification method.

5.3 Wet channel classification by multispectral data

In this paragraph, a simple wet-channel classification method is presented based on the use of the multispectral indices introduced in the §2.2.3. To identify the most appropriate water index in the classification of the wet channel, the reflectance of the water in the different bands and for various acquisition dates was measured.

The spectral signatures of the Po River's water were derived by delimitation of water surfaces on the very high-resolution image and computation of the average reflectance of these areas in the various spectral bands within the GEE platform. The water of the Po River showed the highest values in VIS (480–660 nm), values slightly lower, but still high, in the NIR region (750–900 nm) and closer to zero in the SWIR wavelengths (1500 nm).

The trend of the spectral signatures represented in Figure 21 differs from those presented in literature by Malinowski et al. (2015). The spectral signatures of the Po River water obtained by Landsat-8 and Sentinel-2 have almost similar reflectance values, while Landsat 4-5 has values lower and closer to turbid water signature reported in literature (Malinowski et al. 2015). The reflectance values of the water in specific wavelengths change according to, for example, the turbidity of the water, the presence of vegetation, but also according to the characteristics of the sensor that is used for the construction of the spectral signatures. However, although there are deviations between the reflectance values obtained by the different sensors, the trend remains almost the same (Figure 21).

The classification principle on which the multispectral indices are based is to exploit the difference between the bands for which the reflectance values are significantly different.

In this case, the water spectral signatures suggest that the SWIR band (B11 for S2, B6 for L8, B5 for L4/5) is more appropriate to map the wet channel than the NIR band (B8 for S2, B5 for L8, B4 for L4/5), and since the *MNDWI* exploits the reflectance difference between the green (B3 for S2 and L8, B2 for L4/5) and the SWIR bands, *MNDWI* with a threshold equal to zero was used to extract the wet channel.

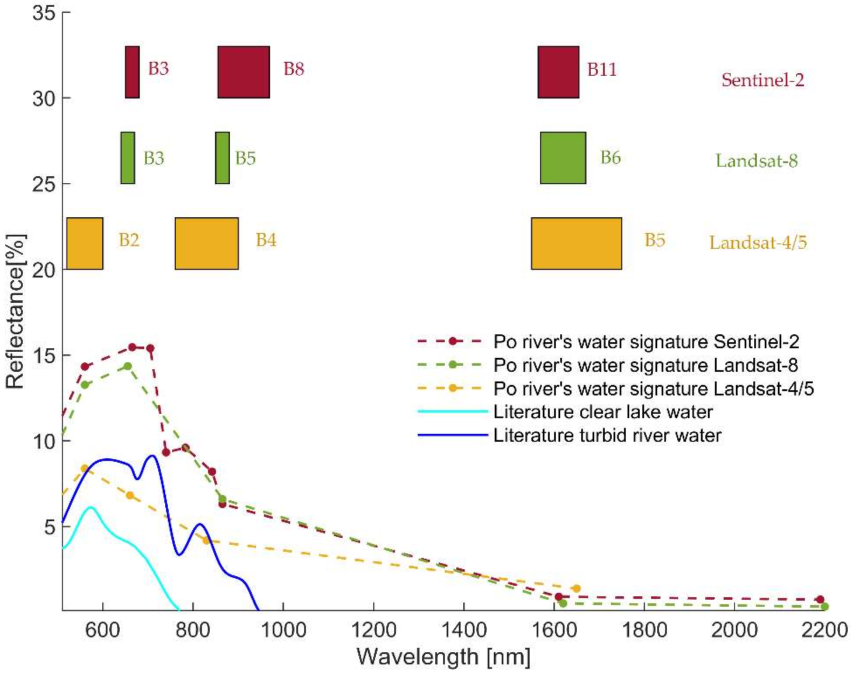

Figure 21: Spectral reflectance of Po River's water extracted by S2, L8 and L4/5 bands and literature water spectral signature (adapted from Malinowski et al. 2015).

The *NDWI,* in some cases, may not correctly identify the wet channel due to the smaller difference of the water reflectance between the green and NIR wavelengths. This was also observed by Jiang et al. (2014), who demonstrated that the *MNDWI* with a zero threshold has a greater capacity to classify turbid water than the *NDWI*. A further comparison between *NDWI* and *MNDWI* is reported in the next paragraph.

5.4 Comparison between water indices: *MNDWI* vs *NDWI*

The reflectance analysis conducted in §5.3 showed that the water of the Po River has high reflectance values in visible wavelengths, nonnegligible values in the wavelengths of the NIR and values almost equal to zero in the length of the SWIR. Based on this, to automatically extract the wet channel, a threshold classification method based on the use of *MNDWI* was used. Figure 22 shows a comparison between the wet channel extracted by *NDWI* and *MNDW* of the Landsat4/5 image of 1st June 1990. From Figure 22, it is possible to see that *NDWI* does not correctly classify the wet channel. This difference between the two water indices does not occur for the entire dataset, but only in correspondence to some acquisitions, probably as a consequence of the greater sediment transport that occurred in those days. Therefore, in the case of the Po River, the *MNDWI* is a more suitable index for wet channel classification as this river is characterised by mixed water.

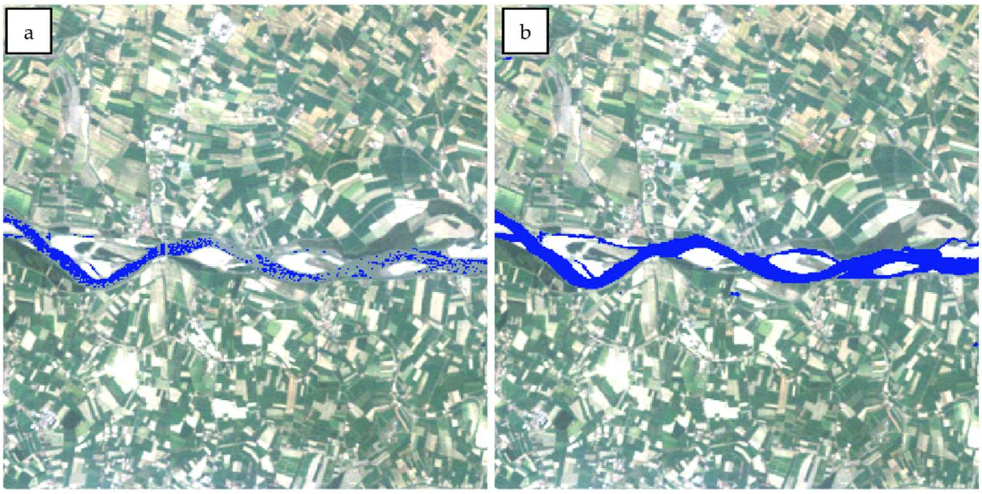

Figure 22: Comparison between the wet channel extracted by (a) NDWI and (b) MNDWI of the 1st of June 1990 with a zero threshold, H = 14.74 m a.s.l.

5.5 Performance estimation of wet channel classification

The validation of the classification method was made by comparing the wet channel derived from L4/5, L8 and S2 with the VHR image. The identified coupes and the relative dates of acquisition are reported in Table 12.

Table 12: Details of the images used for the validation test.

Couples	**VHR data**	**Levels [m a.s.l.]**	**Satellite data**	**Levels [m a.s.l.]**	**Location**
1	World-View-2, 19 October 2010	14.48	Landsat-4/5, 21 October 2010	14.01	Boretto-Borgoforte
2	Google Earth Pro, 4 September 2020	14.69	Sentinel-2, 3 September 2020	14.88	Boretto-Borgoforte
3	World-View-2, 3 December 2017	12.43	Landsat-8, 4 December 2017	12.30	Ostiglia
4	GeoEye-1, 16 September 2018	13.29	Sentinel-2, 16 September 2018	13.29	Ostiglia
5	World-View-2, 8 December 2018	14.33	Sentinel-2, 5 December 2018	14.59	Ostiglia
6	World-View-2, 4 January 2019	13.22	Sentinel-2, 4 January 2019	13.22	Ostiglia
7	World-View-2, 11 September 2019	16.43	Landsat-8, 12 September 2019	16.43	Ostiglia
8	World-View-2, 11 September 2019	16.43	Sentinel-2, 11 September 2019	16.43	Ostiglia

As shown in Table 12, the images compared in pairs were acquired within a time interval of maximum three days. The planimetric surface of the wet channel, given by the envelope of the width of the cross-section in correspondence with the free surface, as will be highlighted below (§ 5.7), is strictly dependent on the water level according to a relationship that expresses the geometry of the cross-section.

The planimetric surface of the wet channel, as well as the water level, is expected to vary over time as a function of the variations in flow rate. However, given the large area of the catchment drained by the studied reach of the Po River, discharge waves propagate with a celerity of a few days and therefore changes of the planimetric surface of the wet channel and water level between consecutive days are expected to be small. It was verified that the maximum difference in the water level between two acquisition dates of the same pair was 0.47 m. This occurred for the images of couple-1 (see Table 12), acquired on 19th and 21st October 2010.

Both a qualitative and a quantitative comparison was made. The qualitative comparisons obtained for the various couples show a satisfactory congruence, as subsequently confirmed via quantitative analyses. The following are some examples, and in particular couple-1, couple-2, couple-3, couple-7 and couple-8. Figure 23 shows couple-1. The classification method can track the wet channel in the main course, which, in this reach, is around 200–400 m wide. However, given the relatively low spatial resolution of the Landsat dataset (30 m), a few small channels close to lateral bars (width around 2 m) are not entirely detectable (Figure 23). Figure 24 shows couple-2. Having a higher spatial resolution, the Sentinel-2 image tracks both the main and secondary channels, and also the shorelines of the bars are more clearly recognizable. Figure 25 reports the comparison with the wet channel extracted by L8 in the Ostiglia reach, confirming what was observed for L4/5 (Figure 23). Figures 26 and 27 show the couples-7 and 8, showing very good results for both comparisons.

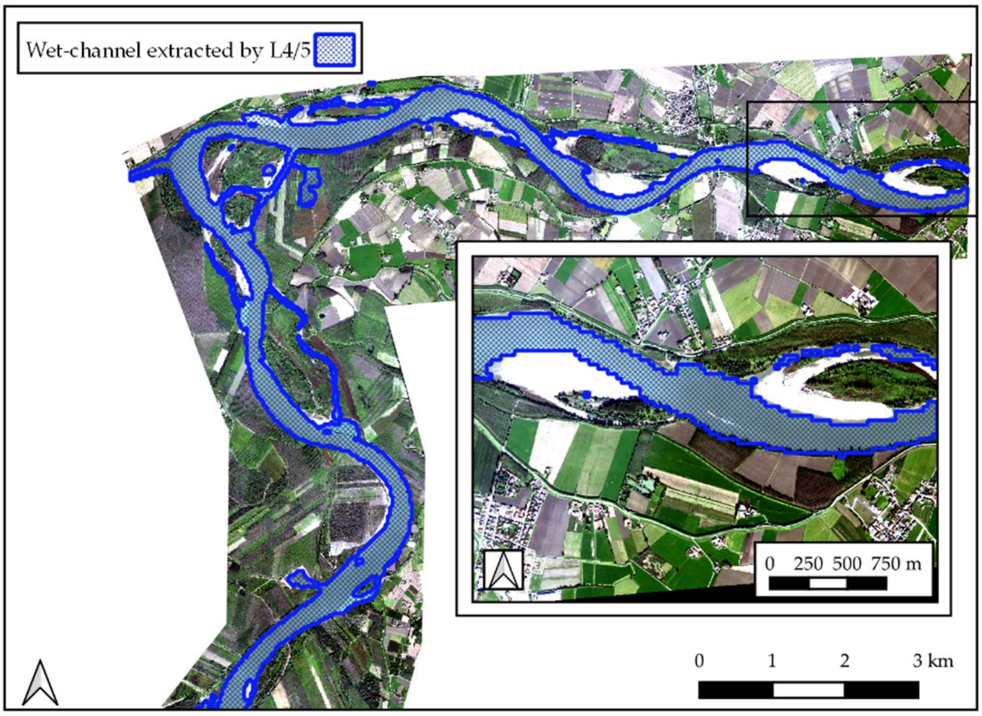

Figure 23: Couple-1, the blue mesh is the wet channel extracted from the Landsat 4/5 image of 21st October 2010 (H =14.01 m a.s.l.), in background the VHR of 19th October 2010 (H =14.48 m a.s.l.),(© TPMO 2020)

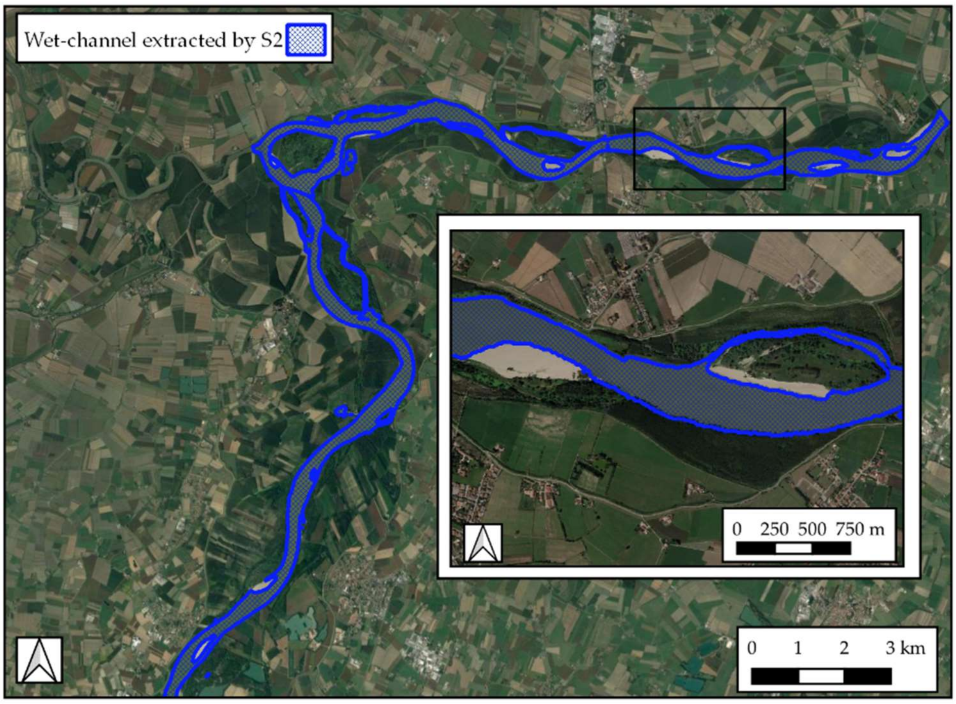

Figure 24: Couple-2, the blue mesh is the wet channel extracted from Sentinel-2 image of 3rd September 2020 (H =14.88 m a.s.l.), in background the VHR extracted by Google Earth Pro Platform, dated 4th September 2020 (H =14.69 m a.s.l.).

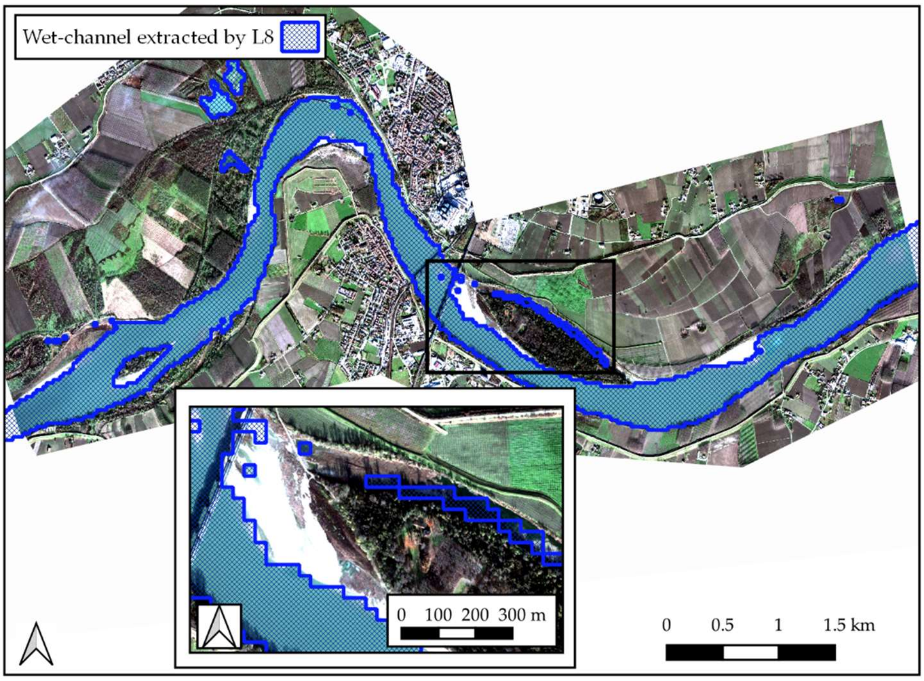

Figure 25: Couple-3, the blue mesh is the wet channel extracted from the Landsat 8 image of 4th December 2017 (H = 12.30 m a.s.l.), in background the VHR of 3rd December 2017 (H = 12.43 m a.s.l.), (©TPMO 2020).

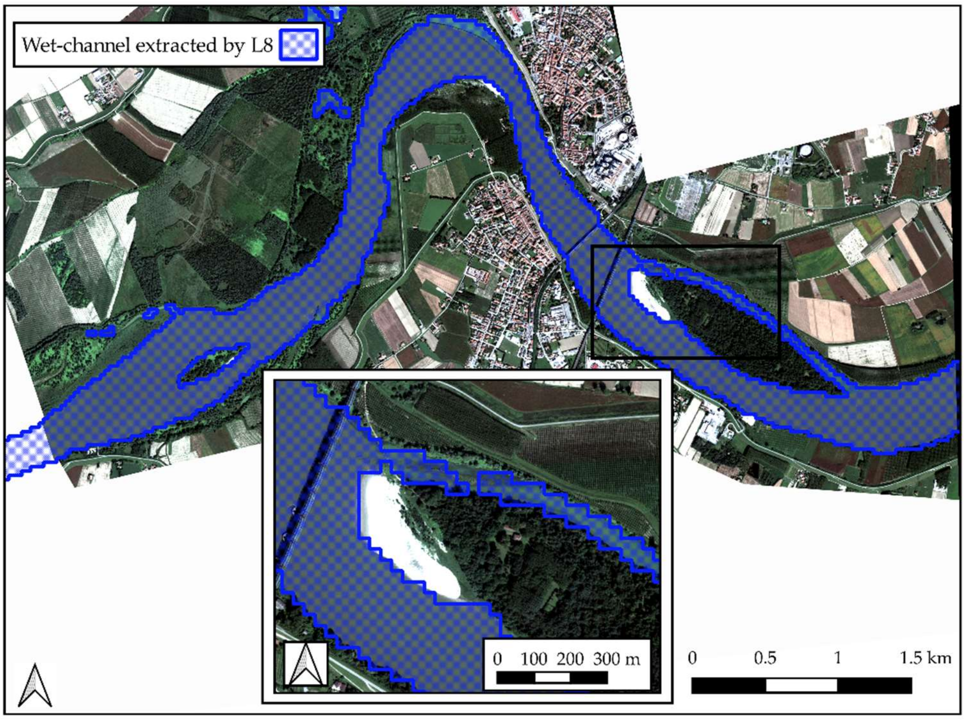

Figure 26: Couple-7, the blue mesh is the wet channel extracted from the Landsat 8 image of 12th September 2019 (H = 16.43 m a.s.l.), in background the VHR of 11th September 2019 (H = 16.43 m a.s.l.), (©TPMO 2020).

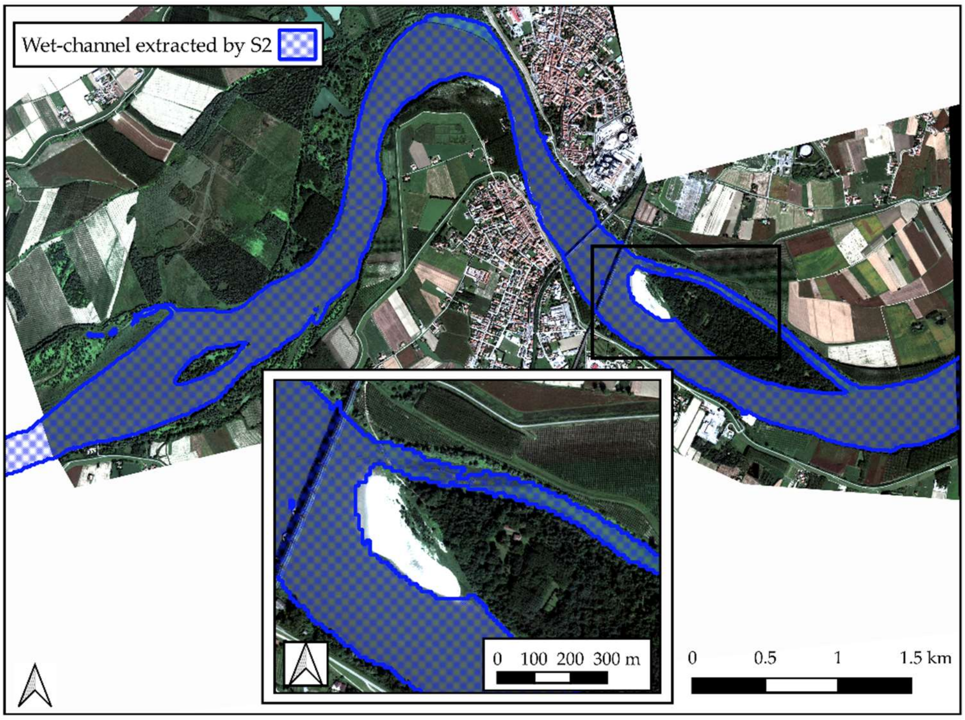

Figure 27: Couple-7, the blue mesh is the wet channel extracted from the Sentinel- 8 image of 11th September 2019 (H = 16.43 m a.s.l.), in background the VHR of 11th September 2019 (H = 16.43 m a.s.l.), (©TPMO 2020).

In addition to the previous qualitative comparison, a quantitative comparison was carried out through a two-class confusion matrix. For each of the available high-resolution images (Table 12), the boundaries of the wet channel were identified through visual inspection, manually drawn in GIS and then rasterized using Orfeo ToolBox (Figure 28). The retrieved raster maps of the wet channel were used as true conditions. The confusion matrices were computed for the eight couples reported in Table 12. *True Positives* (*TP*), *False Positives* (*FP*), *True Negatives* (*TN*) and *False Negatives* (*FN*) were computed for each couple with equations 4,5,6 and 7 introduced in §4.3, for *k* and *l* equal 2. Four main performance indices, *Accuracy* (*A*), *Precision* (*P*), *Recall* (*R*) and *F1-score* (*F1*), were computed by equations (8,9,10 and 11 introduced in §4.3). Table 13 shows the metrics estimated for all the couples. The performance values are always greater than 0.9, except for Recall in couple-6, which is 0.886.

These validation tests confirmed the high classification capacity of the threshold method based on the *MNDWI* and allowed to assess that the results are stable regardless of the particular conditions of the day of acquisition.

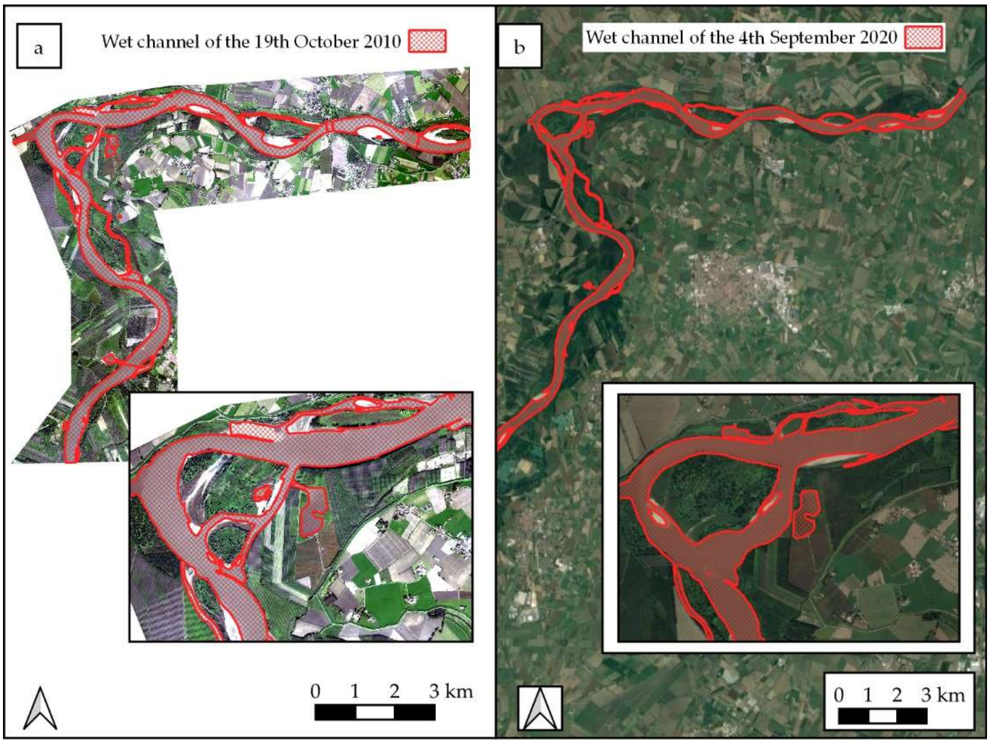

Figure 28: (a) the red mesh is the wet channel retrieved from RGB WV-2 (© TPMO 2020) of 19th October 2010 (H = 14.48 m a.s.l.), (couples -1),(b) the red mesh is the wet channel retrieved from Google Earth Pro image of the 4th September 2020 (H = 14.69 m a.s.l.), (couples -2).

Table 13: Performances metrics estimated for all the validation tests.

Couples	Sensors	Accuracy	Precision	Recall	F1
1	L4/5	0.951	0.952	0.910	0.930
2	S2	0.965	0.969	0.950	0.960
3	L8	0.971	0.976	0.949	0.962
4	S2	0.965	0.958	0.954	0.956
5	S2	0.936	0.935	0.977	0.956

6	S2	0.938	0.973	0.886	0.928
7	L8	0.983	0.983	0.971	0.977
8	S2	0.969	0.968	0.946	0.957

5.6 Consistency check between multispectral datasets

As mentioned above, Mandanici and Bitelli (2016) investigated the possibility of integrating the L8 and S2 datasets, suggesting the need for a specific evaluation for each application. The consistency between the classifications made with L4/5, L8 and S2 is indirectly verified by the performance obtained by all of them compared to the ground truth (see Table 13). Moreover, for couples 7 and 8, the two L8 and S2 derived classifications are almost contemporary and were separately compared with the same ground truth, giving satisfactory results for both (see Figure 26 and 27).
Further verification was obtained from direct comparisons between L8 and S2 cloud-free images acquired on the same day. The possibility of jointly using the multispectral datasets, and therefore the evaluation of the coherence of the wet channel classification obtained by the datasets, was checked only for Landsat-8 and Sentinel-2. Unfortunately, it was not possible to compare the wet channel obtained from all the datasets due to the non-contemporaneity of the operating period of the three satellites. As already introduced in chapter 2, the L4/5 satellite acquired images until 2012, while L8 and S2 were launched in 2013 and 2015. Therefore, only the wet channels extracted from the cloud-free images of the S2 and L8, acquired in the same days were compared. In the observation period (from 2015 to 2020), there are 25 contemporaneous S2 and L8 acquisitions, but the performances were evaluated only for one image per year. The performances were estimated by comparing each pixel of the so-called predicted condition (L8) with the so-called truth condition (S2). For this analysis, the L8 were resampled at the same resolution of the S2 images (10

m) using a bilinear interpolation algorithm in Orfeo ToolBox. After computation of the confusion matrix, the Accuracy, Precision, Recall and F1- score were estimated using equations (8,9, 10 and 11 introduced in §4.3).

Table 14 reports the resulting performance metrics, showing that the overall accuracy is greater than 0.9.

Table 14: Performances metrics estimated for contemporary L8 and S2images.

Date	Accuracy	Precision	Recall	F1
27 August 2016	0.968	0.946	0.951	0.948
17 May 2017	0.954	0.935	0.953	0.944
2 April 2018	0.971	0.962	0.971	0.966
16 February 2019	0.975	0.968	0.964	0.966
28 February 2020	0.966	0.933	0.970	0.951

However, considering the consistency between the classifications of the wet channel extracted from the L4/5 image and the ground truth (see Table 13, Couples-1), it is possible to combine the information extracted from the three satellites and consider a continuous series from 1986 to 2020, with an average revisit time of 32 days before 2012 for L4/5, of 20 days from 2013 to 2015 for L8, of 9 days from 2015 to 2020 for S2 and an average revisit time of 7 from 2015 to 2020 for the merged dataset L8 and S2.

5.7 Relationship between the planimetric surface of the wet channel and the water depth

After validating the consistency of the wet channels with the very high-resolution images and verifying the consistency of the information extracted from the three sensors, an original Matlab code was implemented to automatically extract the wet channel and calculate its planimetric surface for all the merged datasets of cloud-free L4/5, L8 and S2 images, out of a total of 650 images. Comparing the Boretto and Borgoforte reaches, the cross-sections widths of the downstream reach depend more strongly on the water levels, as recognizable from the more-than-linear relationship between the planimetric surface of wet-channel and the water levels (Figure 29a and c). On the other hand, the higher dispersion of the data (lower R^2) is probably linked to a higher propension for the morphological evolution of the cross-section. This behaviour is also recognizable looking at the correlation between river discharge and planimetric surface (Figure 29b and d), with Boretto showing a higher data dispersion for flooding conditions. Given the strong variation of the wet channel planimetric surface with the water stage when aiming to detect the morphological changes of the wet channel, it is necessary to compare the wet channel shape of the images acquired in similar conditions of water depth, as in the following paragraph. The differences in the shape and size of the planimetric surface of the wet channel, in two moments characterized by the same water level, give a clear indication of the occurrence of the morphological changes in the contour of the wet channel. Consequently, to detect any eventual hydro-morphological changes, all the free cloud satellite images referring to similar water levels H were grouped and compared. These groups were composed of at least three images within the interval $H \pm \Delta H$, with $\Delta H = 4$ cm.

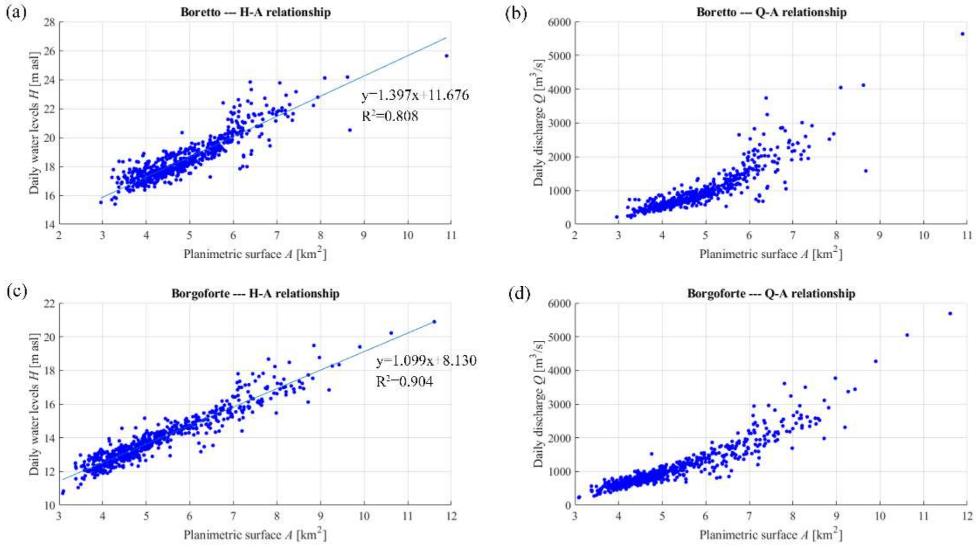

Figure 29: Daily water levels (H) and daily discharges (Q) at Boretto and Borgoforte, versus the planimetric surface of the wet channel (A) derived from the merged dataset of multispectral satellite images

5.8 Monitoring morphological changes

To assess whether the monitored reaches have undergone any hydro-morphological changes in the last 30 years, groups of images acquired with the same water level were compared. Such a comparison did not point out any major morphological changes in the period 1986-2020. Figures 30 and 31 show an example of how to use satellite imagery to track morphological changes. The Figures show the comparison between images acquired at the same water level (14.37 m a.s.l. on average) for the Borgoforte and Boretto reaches. The comparison shows that in correspondence with the sediments bar in the black square of Figure 30a, only small morphological changes are observed. In particular, the sediments bar increases its surface in the period 1993-2014, subsequently, in 2018 its extension decreases and then increases again in 2020. The only significant changes observed are those highlighted in the next paragraph, which concern a small part of the study reach (Figure 19b and Figure 30a, green square).

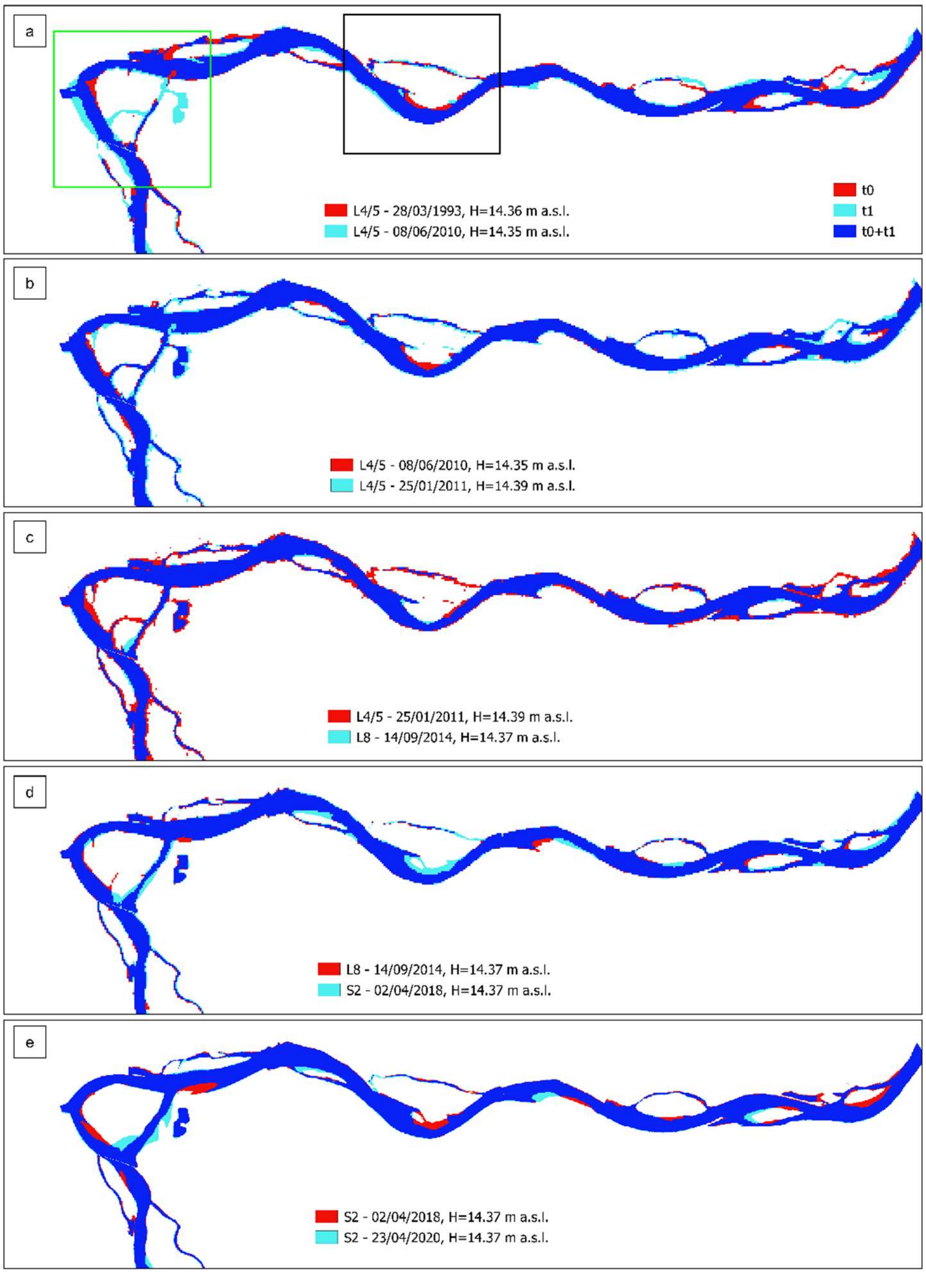

Figure 30: Geomorphological evolution of the Borgoforte reach of the Po River, each sub-panel shows the evolution over time. The areas covered by water respectively on the starting (t0) and final (t1) day of the interval are shown in red and cyan, while the area covered by water in both dates is shown in blue.

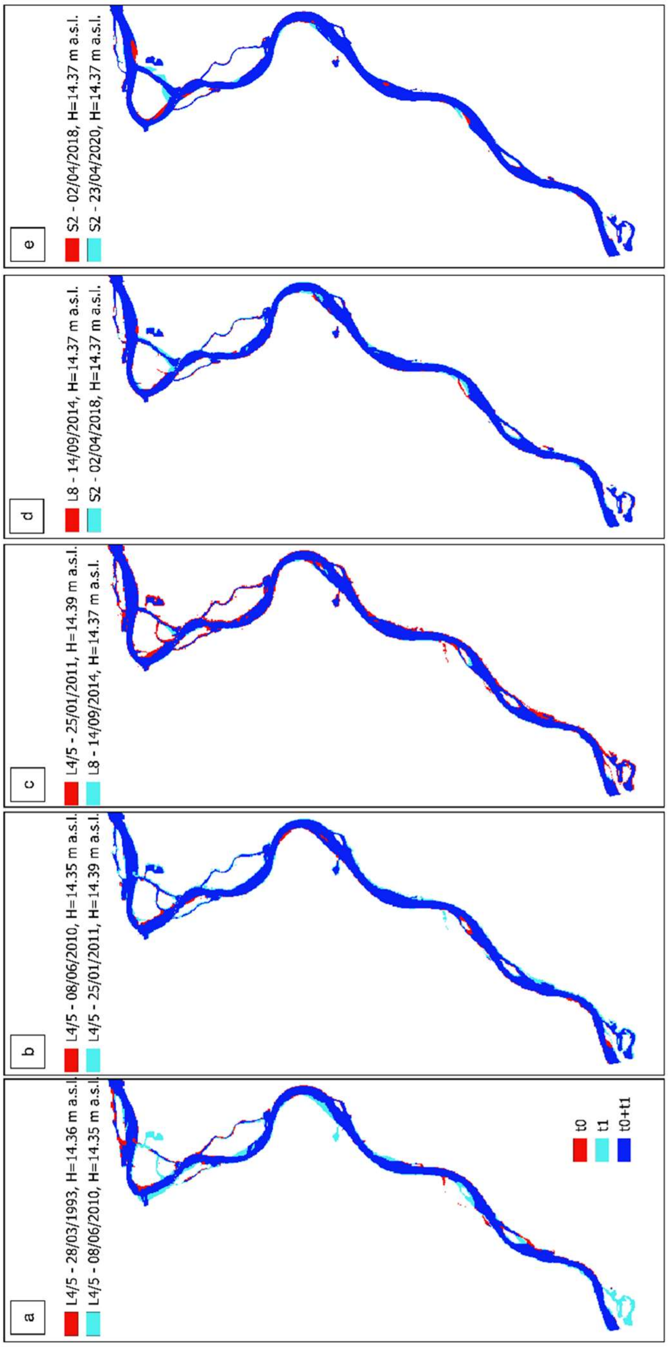

Figure 31:Geomorphological evolution of the Boretto reach of the Po River, each sub-panel shows the evolution over time. The areas covered by water respectively on the starting (t0) and final (t1) day of the interval are shown in red and cyan, while the area covered by water in both dates is shown in blue.

5.8.1 Monitoring pre and post river restoration intervention

To investigate the use of multispectral satellite images as a support tool for studying the effects of a localised river restoration intervention, a small part of the study reach was considered (Figure 19b and 30a, green square). In 2013, a submerged wing dyke was reshaped to allow for the re-activation of the lateral channel in a condition of frequent peak flow, as described in §5.1. To evaluate the effects of this wing dyke's lowering, images acquired with the same water level were compared (13.26 m a.s.l. on average) before and after the restoration works. In the 1994-2004 comparison shown in Figure 33, erosion along the left bank of the main channel and deposition along the right bank were observed. In comparison, after 2004 and before 2013, a stable condition was observed on the left bank and an alternation of erosion and/or deposition phenomena on the right. After the lowering of the wing dyke, the secondary channel on the right side was reactivated. The effect of the intervention becomes more evident with time: the more recent the images are, the bigger the planimetric surface of the wet channel is. During the period 2011-2015, the reactivation of the secondary channel determined a significant deposit along the right bank of the main channel. The morphological configuration of the main channel remains stable until 2017, starting from which small deposits are observed along the right back. Figure 32 shows a comparison between an orthophoto of the study area acquired on 26th March 1988 and the image provided by Google Earth Pro of 4th June 2021. This comparison does not take into account hydro-mophological changes over the time, but allows to observe the state of the river on the two dates. The comparison in Figure 33, on the other hand, shows how the current morphological configuration was reached over time.

Figure 32: (a) Orthophoto of the 26th March 1988, (H = 13.97 m a.s.l); image provided by Google Earth Pro platform of .4th June 2021, (H = 12.61 m a.s.l).

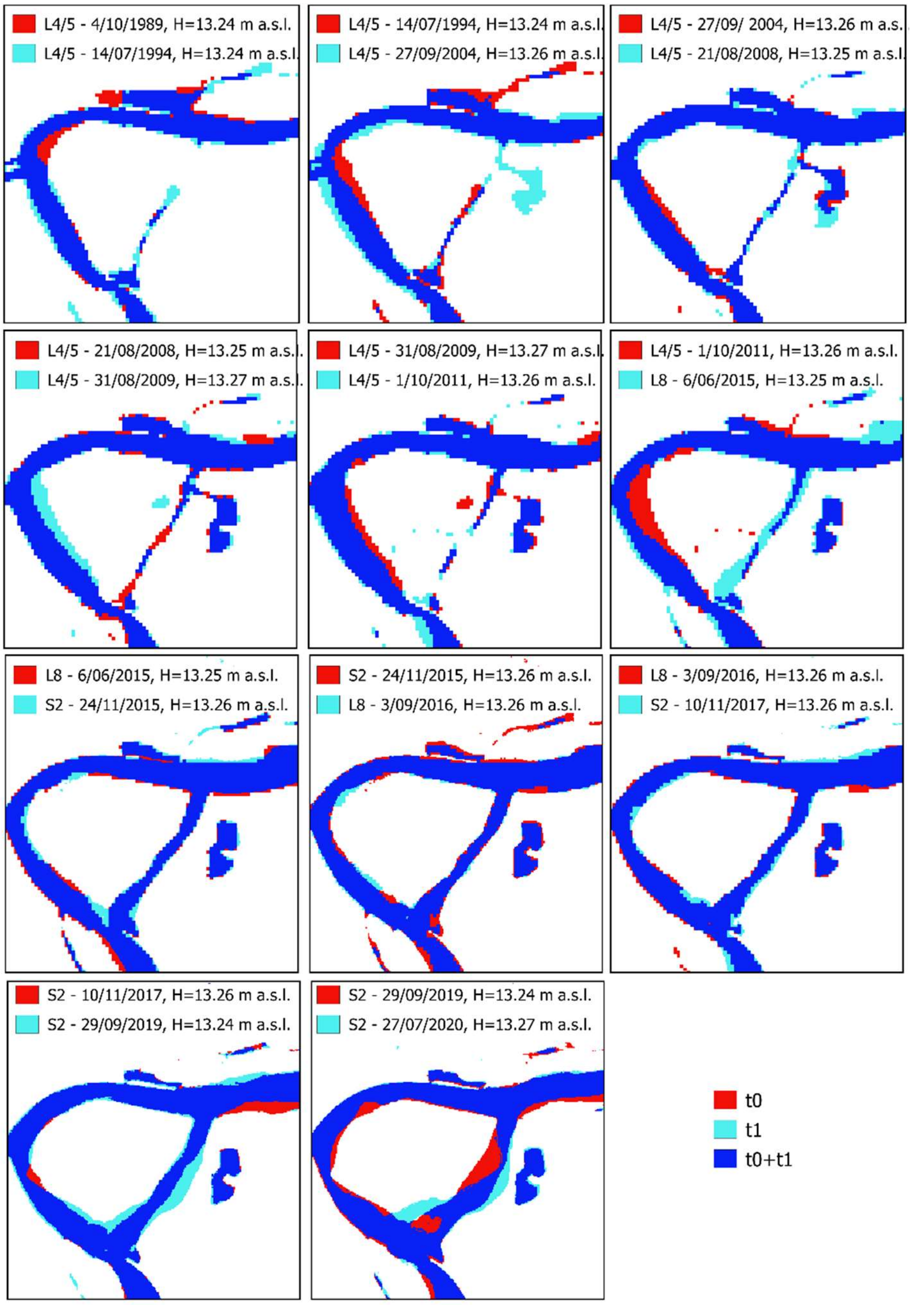

Figure 33: Geomorphological evolution of a secondary channel of the Po River, each sub-panel shows the evolution over time. The areas covered by water respectively on the starting (t0) and final (t1) day of the interval are shown in red and cyan, while the area covered by water in both dates is shown in blue.

In the images acquired from 2004 to 2009 (Figure 33), it is possible to distinguish the connection between the secondary channel and the humid area. In the following images, such a connection is no longer visible. The inability to track the possible connection between the river and the surroundings is due to the growth of vegetation, which represents a limit for the remote monitoring of river dynamics via multispectral data.

5.9 Monitoring hydro-morphological changes using Sentinel-1 data

As shown in the previous paragraphs, Landsat4/5-8 and Sentinel-2 multispectral data can monitor wet channel evolutions with very good accuracy. However, one of the main limitations of multispectral imagery is the inability to provide information in the presence of cloud cover, as well as guarantee continuous monitoring in areas with frequent rainfall. SAR data can overcome this problem, thanks to the ability to be acquired even in the presence of cloud cover.

To investigate the potential offered by the data Sentinel-1, a supervised deep learning algorithm proposed by Gargiulo et al., 2020 was tested.

In detail, after the chain of pre-elaborations of Sentinel-1 images described in §2.2.4, a deep neural network was trained starting from the Sentinel-1 input data, considering as a reference the water masks extracted from the multispectral images. Once the network was trained, it was tested on some of the dates in which very high-resolution images were available.

Figures 34,35,36, and 37 show the qualitative comparison between very-high resolution images (a), VV polarization of Sentinel-1 images (b), VH polarization of Sentinel-1 images (c) and the water mask extracted by the deep learning algorithm (d). Figure 34 shows the result of the classification along the Borgoforte reach, while Figures 35,36 and 37 show the results at a sediment bar near the Boschina Island (Ostiglia).

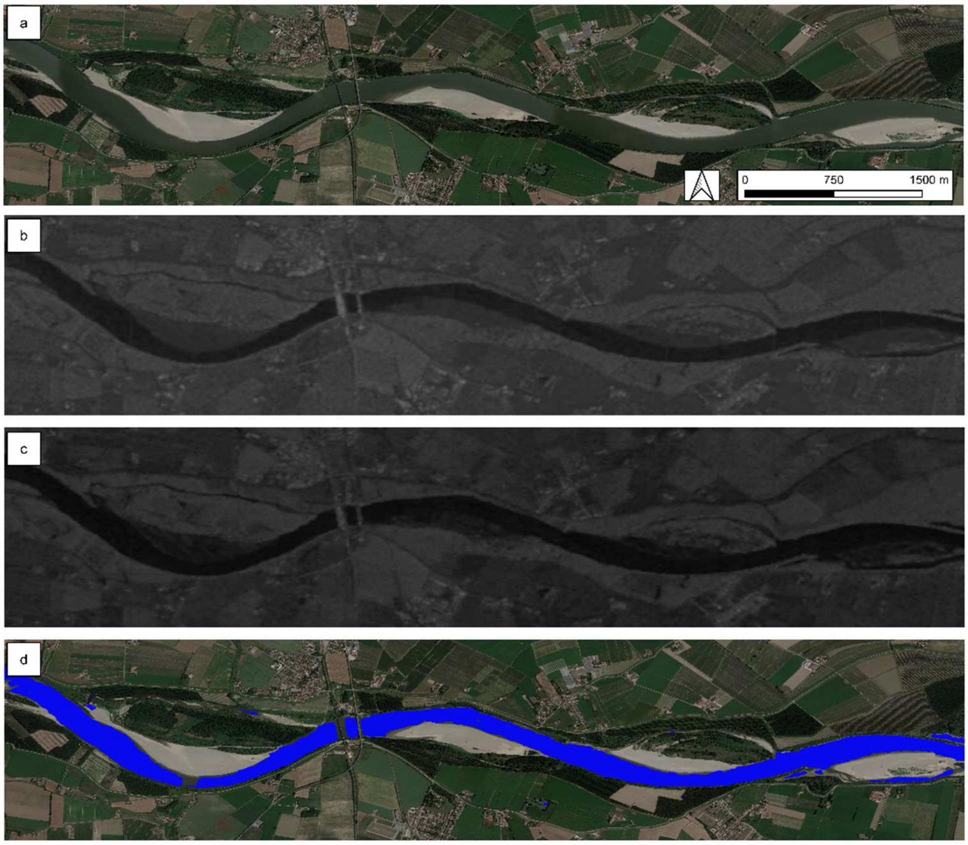

Figure 34: (a) Very high-spatial resolution image extracted by Google Earth Pro Platform of 4th June 2021 (H = 12.61 m a.s.l), (b)VV polarization of Sentinel-1 images of 4th June 2021, (c) VH polarization of Sentinel-1 images of 4th June 2021and (d) the water mask extracted by deep learning algorithm.

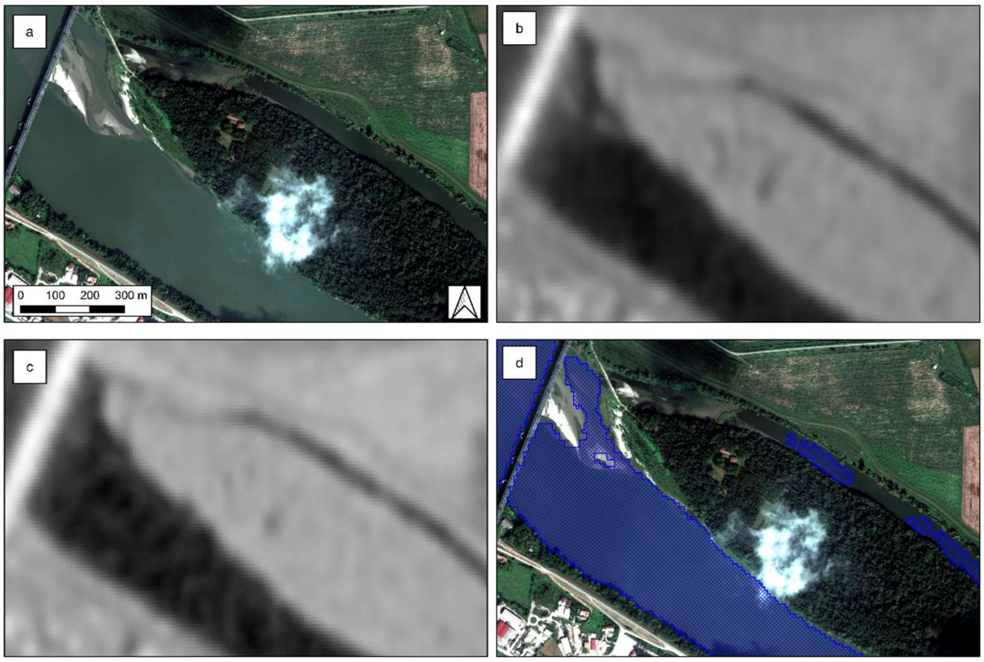

Figure 35: (a) the VHR image of the Geo-Eye-01 (© TPMO 2020) of 16th September 2018 (H = 13.29 m a.s.l), (b) VV polarization of Sentinel-1 images of 16th September 2018, (c) VH polarization of Sentinel-1 images of 16th September 2018 and (d) the water mask extracted by deep learning algorithm.

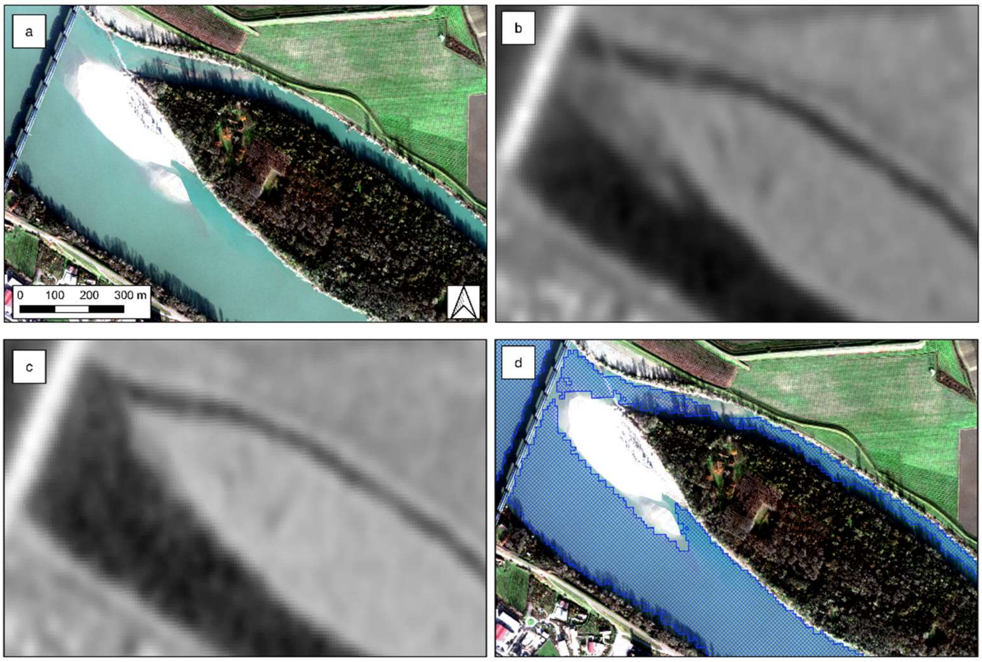

Figure 36: (a) the VHR image of the World-View-02 (© TPMO 2020) of 8th December 2018 (H = 14.33 m a.s.l), (b) VV polarization of Sentinel-1 images of 10th December 2018 (H = 14.23 m a.s.l), (c) VH polarization of Sentinel-1 images of 10th December 2018 and (d) the water mask extracted by deep learning algorithm.

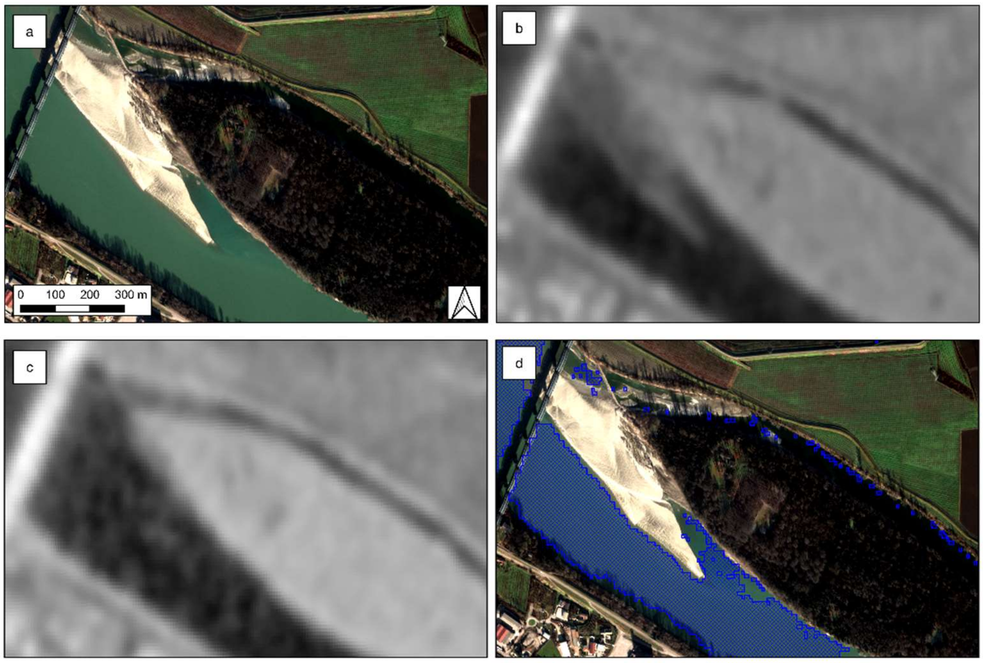

Figure 37: (a) the VHR image of the World-View-02 (© TPMO 2020) of 4th January 2019 (H = 13.22 m a.s.l), (b) VV polarization of Sentinel-1 images of 9th January 2019 (H = 13.11 m a.s.l), (c) VH polarization of Sentinel-1 images of 9th January 2019 and (d) the water mask extracted by deep learning algorithm.

As observed in Figures 34,35,36 and 37, the co-polarized images are more informative than the cross-polarized ones. In VH polarization, the sediments are not recognised, while in VV polarization, in addition to the water presence, it is also possible to identify the sediment bars. However, both polarizations were useful for extracting the water masks.

The water masks extracted from the deep learning algorithm tracks the wet channel with good accuracy (see Figure 34 and 36). However, on some dates, the small channels close to the lateral bars are not entirely detectable (see Figure 35), and the shorelines of the bars are not clearly recognizable (see Figure 37).

5.10 Discussion

Like many other large lowland watercourses in Europe, the Italian Po River is heavily regulated and characterized by incised channels, loss of continuity, and modified hydroperiods. As a consequence, former extensive aquatic/terrestrial transition zones lack most of their basic ecological functions (Schropp 1995; Curran et al. 2020). An effective restoration measure is the reconnection of floodplains and secondary channels that foster the continuity of water, sediment and biota. The continuous monitoring of fluvial dynamics is essential to know past evolutionary trends, to help water managers and decision-makers in managing any hydro-morphology alterations of rivers (Sinha and Ghosh 2012) and in improving their ecological status (Nones 2021; Boothroyd et al. 2021a). Furthermore, post-intervention monitoring is equally essential to understand whether that intervention was effective or not. Thanks to the recent developments in remote sensing, it is now possible to observe river dynamics at a very detailed spatio-temporal scale. Multispectral satellite images at moderate spatial resolution have been used with good results for hydro-morphological processes monitoring, at different spatial scales and in rivers of different sizes. In medium to large rivers, where the average river width is more than 2–3 times the spatial resolution of the satellite images, it is possible to monitor processes up to the scale of the hydro-morphological units and observe, for example, changes along reaches (Rashid et al. 2021), the evolution of sandbars (Kryniecka and Magnuszewski 2021) and water pool dynamics (Seaton et al. 2020). It is obvious, however, that such data are not adequate to monitor processes occurring at spatial scales lower than the spatial resolution of the image pixel (Wang et al. 2021). According to Jiang et al. 2014, the minimum width of the river that can be monitored is equal to three image pixels, therefore Landsat and Sentinel-2 data can be used for rivers wider than about 90 m and 30 m respectively.

The reflectance analysis conducted in §5.3 showed similar results to those proposed by Jiang et al. (2014), demonstrating that, in the NIR wavelengths, mixed water has a reflectance higher than pure water, and showed that the *MNDWI* (Xu 2006) has a greater ability to discriminate mixed water than the *NDWI* (McFeeters 1996), even if the *MNDWI* can incorrectly classify some pixels covered by mountain shadow. Figure 21 shows that the water of the Po River has high reflectance values in visible wavelengths, non-negligible values in the wavelengths of the NIR and values almost equal to zero in the length of the SWIR. Based on this, a threshold classification method based on the *MNDWI* were used to automatically extract the wet channel. Moreover, since our study focuses on a relatively flat area (Figure 19), no errors of classification due to the shadow of the mountains have been found. The validation of image classification should be performed through a comparison with field data. However, when field data are unavailable or insufficient, very high-resolution images can be effectively used as the ground truth. In this study, VHR images with a spatial resolution of about 0.5 m were used. Given the ratio between the resolution of the VHR images and the size of the observed object (average wet channel width around 500 m), the image can be considered a sufficiently reliable ground truth. The capabilities of the *MNDWI* index in classifying the wet channel showed an accuracy higher than 0.9. Despite its simplicity, the proposed classification method can map the wet channel with a considerable performance. By comparing the wet channel extracted from L4/5 and L8 with the RGB of the very high-resolution images, it is possible to observe that channels narrower than 30 m are not identifiable, while for Sentinel-2 images the minimum width of observable channels is reduced to 10 m. As shown in this work, despite the spatial resolution not being high, these data can be used to map large enough wet channels with relatively good precision and to monitor the hydro-morphological changes up to the scale of macro hydro-morphological units. In addition to the choice of the spatial scale, it is necessary to choose the appropriate time scale for the process to be observed. For example, Gurnell et al. (2015) pointed out that the time scale varies between a maximum of one hundred years and a minimum of ten years to monitor the dynamics at the segment scale, while the scale is reduced to 1–10 years to analyse trends at the hydro-morphological units. The choice of an adequate temporal resolution is connected to the event under study: the more intense and rapid an event is, the more frequent the images should be acquired. As an example, to monitor a flooding wave and its effects on the channel morphology, it is necessary to first understand the wave dynamics (i.e., celerity), which is a function of both the river dimension and the hydrology, and then evaluate what satellite data can have an adequate spatial resolution and revisit time to monitor the event (Alexakis et al. 2012). In the case of multispectral images, the actual temporal resolution is conditioned by the availability of cloud-free images. This is an additional limitation for tracking rapid fluvial changes (Boothroyd et al. 2021b). Unfortunately, to date, no free data with high spatial resolution are available to monitor very rapid hydro-morphological changes (time scale 1 day). Commercially available very high spatial resolution images with multiple acquisitions within 24 hours allow to monitor small rivers, observe processes at small spatial scales and monitor rapid hydro-morphological changes. However, these data are provided for free only for research purposes and therefore their use for river management is still highly limited. In addition to understanding the short-term dynamics of fluvial systems, satellite information is beneficial for catching medium or long-term hydro-morphological changes, like the ones presented in Figures 30, 31 and 33. In order to detect morphological changes, there is the need to collect a relatively high number of images acquired in similar conditions of water depth. As shown in this work, the opportunity to integrate L4/5, L8 and S2 images makes it possible to extend the analysis to a relatively long-time interval (from 1986 to 2020) as well as to increase the time resolution in the period between 2015 and 2020. The joint use of the L8 and S2 provides the advantage of reducing the revisit time; for the merged dataset the average revisit was reduced to 7 days than the average time of 20 and 9 days for L8 and S2. However, if wanting to further increase the review time, to date, the only satellite data with global coverage, with moderate spatial resolution and available for free are the SAR Sentinel-1 data.

The comparison of the wet channel extracted by S2 and L8, despite the different spatial resolution, showed an excellent congruence, with an accuracy higher than 0.9. The analysis of the planimetric surface of the wet channels and hydrological characteristics showed an almost linear correlation between the planimetric surface and the water stages, while the correlation with the discharge is more than linear, as usually shown by alluvial rivers (e.g., Yalin 1992; Nones and Di Silvio 2016). Looking at Figure 29a,c (§ 5.7), it is worth noting that the angular coefficient of the linear regression line of the Boretto reach is equal to 1.397, while for the Borgoforte reach is equal to 1.099. This means that the same increase of water level gives rise to a greater increase of planimetric surface of the wet channel at Borgoforte reach than at Boretto. This difference can be explained by the local morphology, the Boretto reach has a more mono-cursal pattern, with a few secondary channels, while the morphology of the Borgoforte reach is more complex (see Figure 19). Many studies focus on the possibility of exploiting this relationship to make indirect estimates of the water level and discharge in non-instrumented rivers. This work, on the other hand, focused on a potential that is still little explored, namely the possibility of indirectly monitoring morphological changes. To do this, images acquired in days with similar water stages were compared (Figures 30, 31 and 33). As pointed out by Lanzoni et al. (2015), the Po River has not undergone any significant variations in the last 35 years, at least at the basin scale, while some local changes occurred only after extreme flooding events, characterized by 50–100 years of return periods. The quasi-equilibrium conditions at the reach scale are also confirmed by the analysis carried out in this chapter (Figures 23–27, 30-33). In Figure 33, it is possible to observe the reactivation and evolution of a secondary channel after the lowering of a wing dyke, which took place in 2013. In the same figure, the creation of an artificial wetland, on the right of the secondary channel, is recognizable. The analysis in this chapter showed that multispectral images provide excellent results and can be used to monitor the hydro-morphological evolution in fluvial environments.

As mentioned before, the SAR can be useful to overcome the cloud cover problem. Conversely, the SAR data requires a longer pre-elaboration (§2.2.4) and elaborate automatic classification methods. In §5.9, a supervised deep learning algorithm proposed by Gargiulo et al. 2020 was applied to extract the wet channel from the SAR Sentinel-1 images. The qualitative comparison (Figures 34-36) shows that the supervised deep learning algorithm provides good and encouraging results. In some areas (Figure 35, 37), it was observed that the classification does not track the wet channel with the same precision as the multispectral data. However, training with additional data can further improve the classification shown in this work.

At present the multispectral is more suitable for making long-term analyses like the one shown in this thesis, while the SAR can be very useful for observing rapid hydro-morphological changes in rainy periods.

It has been observed that co-polarised (VV) images allow to identify the presence of water and sediments. However, both polarizations allow to extract the water masks shown in Figures 34-37 and provide important information in river environments. The difference between the two polarizations allows to discriminate the sediment class from the vegetation class, and this difference can be exploited to identify sediments and vegetated bars. Future developments in classification techniques could therefore make it possible to obtain information on the three land cover classes: water, sediments and vegetation.

Additionally, SAR data are also sensitive to vegetation structure and surface roughness, and analysis of the signal response in different polarisations could be an important step forward in assessing the dynamics of vegetation as well as the size of sediments in the riverbed.

6. Wet-dry dynamics observation for hydrological regime assessment: the study case of the Non-Perennial Rivers of the Cilento (Italy)

Non-perennial rivers are characterized by periods with dry bed or chains of isolated ponds. In these environments, it is possible to identify three principal flow conditions, which represent lotic, lentic and terrestrial habitats. The duration of each flow conditions depends on the annual rainfall regime, the local hydrogeological conditions of the reaches (e.g., substrate type and permeability), width of the reaches, the characteristics of the underlying catchment, and water withdrawals. The flow conditions and their duration significantly influence the presence of water-related species. These freshwater environments represent over 50% of the length of the world river network and are characterized by a high spatial and temporal inhomogeneity and, in some cases, by rather small widths.

It follows that high spatial resolutions, high observation frequencies, and a multi-year data archive must be available to monitor their hydrological regime. Given the large amount of data required, the use of high-resolution images (0.50 m, from drones or satellites) would involve too high a cost and lower acquisition frequency. Among freely distributed multispectral images with systematic global coverage, the Sentinel-2 mission provides the highest spatial resolution and revisiting frequency. In this chapter, the potential of multispectral data distributed by the Sentinel-2 mission were employed to monitor the hydrologic regime of three non-perennial rivers in the Campania region, from 2015 to 2021. In detail, 141 Sentinel-2 free-cloud images were used to identify one of the three possible flow conditions: flowing, ponding and dry bed.

6.1 Case study: the Cilento rivers

The case studies are five reaches of the hydrographic network of the “Cilento, Vallo di Diano and Alburni” National Park, located in in the province of Salerno, in the Campania region (Southern Italy), that covers an area of 1810 km^2, stretching from the Tyrrhenian coast to the foot of the Apennines (see Figure 38), with an altitude range from sea level to the top of the Cervati Mountain, at 1898 m a.s.l. Established in 1991 to preserve its great flora and fauna biodiversity, it is one of the widest Italian National Park. It includes 29 Sites of Community Interest (SIC) and 8 Special Protection Areas (SPA), set in application of the European Habitat (92/43 / EEC) and Birds (79/409 / EEC) Directives. There are fauna species of considerable community importance, such as the otter (Lutra lutra), that is the symbol of the park, many amphibians (e.g. Bombina pachipus and Salamandrina terdigitata), odonates (Oxygastra curtisii and Coenagrion mercuriale) and fish (Lampetra planeri and Rutilus rubilio). From a geological point of view, the Park is mainly composed of carbonate and terrigenous mountain massifs, marly-clayey hills as well as alluvial and coastal plains (Santangelo et al., 2015). A system of carbonate aquifers produces a complex underground circulation and the presence of several springs. The climate is characterized by a wet season from September to May, the rainiest month is November with an average of around 90 mm, the driest month is July with an average of around 10 mm. The total annual average is around 1200 mm/anno. The warm season June-September has a maximum daily temperature above 27 °C, the cool season November-March has a maximum daily temperature below 17 °C.

Three non-perennial rivers Sciarapotamo, Mingardo and Lambro close to the Centola (Palinuro) countryside were selected as case studies (see Figure 38). In detail, five river reaches were investigated: three reaches belong to the Mingardo, one to the Lambro and one to the Sciarapotamo streams (see Figure 38).

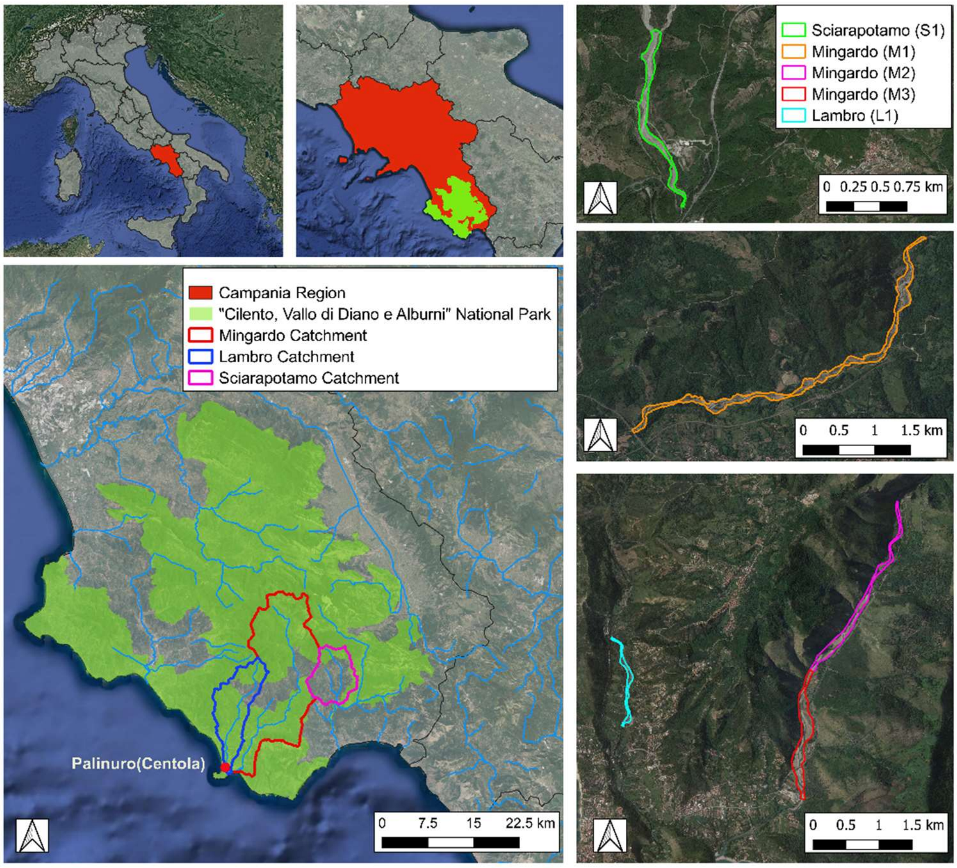

Figure 38: Geographical framework of the study area.

6.1.1 Sciarapotamo

The Sciarapotamo is a right tributary of the Bussento stream; it has a catchment area of about 54 km^2 and a length of about 11 km. The studied reach (S1) has a length of about 2 km and ends at about 500 m upstream from the confluence with the Bussento River, (Figure 38); it has a narrow channel with a wandering planform (braiding index 1.21 and sinuosity index 1.09). The River Basin Management Plan (RBMP), developed by the Southern Apennines Basin Authority (Autorità di Bacino Distrettuale dell'Appennino Merdionale) classified the

Sciarapotamo as intermittent, inventoried only one withdrawal from groundwater and assessed a high ecological status and good chemical status.

6.1.2 Mingardo

The Mingardo is the longest of the studied rivers, with a catchment of about 232 km^2 and total length of 38 km. It originates in the Gelbison mountain and flows in the Tirreno sea close to the village of Palinuro. Three reaches are investigated, the upstream wandering channel (M1) and two other consecutive reaches closer to the outlet, these are, proceeding downstream, a single-thread sinuous reach (M2) and a wandering reach (M3).

According to the RBMP, all the studied reaches of the Mingardo are perennial; there are withdrawals from groundwater and springs, and the ecological and chemical status are good for all the reaches. 500 m downstream of the end of reach M3, the main outlet of the floodplain aquifer corresponds to the stream itself.

6.1.3 Lambro

The Lambro River, with a total length of 22 km and drained catchment of about 78 km^2, originates in the Gelbison mountain and flows into the Tirreno sea about 500 meters north of the mouth of the Mingardo River. The studied reach (L1) is wandering. According to the RBMP, the Lambro is perennial, there are withdrawals from springs for both domestic use and irrigation. The ecological status is sufficient and so is the chemical status.

In Table 15, some significant characteristics of the studied reaches are reported. The drained catchments were calculated by placing the closure section at the downstream end of each reach, the average width was calculated from the ratio of the area of the active channel to the length of the center line. It can be seen that during the period of observation (2015-2021) the total annual precipitation is on average 1300 mm.

Table 15:Characteristics of the studied reaches.

Catchment	Reach	Drained catchment [km^2]	Average width [m]

Sciarapotamo	S1	54	107
Mingardo	M1	180	77
Mingardo	M2	221	62
Mingardo	M3	225	117
Lambro	L1	74	38

6.1.4 Hydrological data

Freely available hydrological data were extracted from the “Centro Funzionale Multirischi della Protezione Civile Regione Campania” website (http://centrofunzionale.regione.campania.it/) covering the period 2015-2021. Daily time series of rainfall, air temperature (maximum, medium, minimum) and water levels were used. The available gauging stations within or adjacent to the Sciarapotamo, Lambro and Mingardo catchments were respectively 6, 3 and 8 for rainfall and 3, 5 and 3 for temperature. Rainfall (R) and air maximum, mean and minimum temperature (T_MAX, T_MEAN and T_MIN) data were spatially interpolated on catchments area using the Thiessen polygons method for each studied reach. Daily water levels are available at two measuring stations, one almost 500 m downstream the L1 reach and another at around 600 m downstream the M3 reach.

6.1.5 Field surveys

To evaluate the potential of S2 images in monitoring the hydrologic regime of non-perennial rivers, field surveys were performed at the same time as the S2 acquisitions. In detail, five field surveys in various condition of river flow were performed (26th June 2020, 26th July 2020, 19th September 2020, 6th February 2021 and 13th December 2021). During the field surveys, geo-located pictures were acquired, with the width, length and depth of several water ponds being measured. In addition, a photogrammetric survey by UAV (Unmanned aerial vehicle) was carried out on 13th December 2021.

The UAV acquired images through a DJI Mavic 2 Pro, which weighs about 900g, equipped with the brand-new Hasselblad L1D-20c camera with exclusive Hasselblad Natural Colour Solution (HNCS) technology. The sensor is a 1” CMOS with 20 MP resolution (pixel size of 2.4 microns), 77° FoV and 28 mm equivalent focal length, allowing for RAW photography. The remote control has a range of 8 km.

With the DJI Mavic 2 Pro, only nadiral images were captured, organised in a flight plan with a single grid. Thus, 55 images at a height of 125 m were acquired, detecting a territorial extension of about 600 m^2 (resolution about 3 cm). The data collected in the acquisition campaigns were processed in the Agisoft Metashape environment. Particular attention was given to the optimization of the orientation of the cameras, regarding both the implementation of GNSS geo-localization data and the filtering of tie points. In addition to the field surveys, a very high-resolution satellite image (VHR) provided free of charge by the Google Earth Pro platform were used.

6.2 Spectral signature analysis and false colour images

In order to get a clearer view of the small streams from the Sentinel-2 images and therefore to better distinguish between the various macro hydro-morphological units (wet channel, sand bars, vegetated bars), the differences in the spectral signatures were exploited. Starting from the VHR images provided by Google Earth Pro and UAV, as well as from the geo-located pictures, several polygons with known land cover were extracted (water, bare sediments, grass and bushes). The spectral signatures across the S2 bands, for the different soil cover classes, were plotted using the pixels contained within their respective polygons. All the S2 bands were used except for the atmospheric bands B1, B9 and B10. In order to identify any seasonal variations of the spectral response, the spectral signatures were extracted in different seasonal flow conditions, in late spring (14th June 2019), winter (6th February 2020), and late autumn (13th December 2021). The spectral signatures were extracted by original code in GEE and are shown in Figure 39a, Figure 39b and Figure 39c. Thanks to the very high quality of the orthophoto acquired by the drone, it was possible to distinguish flooded areas with deeper water, and flooded areas with shallower water. Consequently, it was possible to extrapolate two water spectral signatures: shallower water and deeper water (Figure 39c).

Figure 39a shows how the water spectral signature of 19th June has a high reflectance value in the infrared wavelengths, presenting a completely different pattern from both that shown in literature (Figure 5) as well as the spectral signature extracted for the Po River (Figure 31, in §5.3). The water spectral signature of 14th June has a similar pattern to the shallower water spectral signature of 13th January. This means that the spectral signature of the water varies with depth, in particular as the depth decreases the reflectance values in the infrared wavelengths increase, because the spectral signature is influenced by the type of the background material. In general, during the summer period, non-perennial rivers are characterised by shallower waters and therefore the water spectral signature is similar to that shown in Figure 39a.

From the observation of the different spectral signatures, an optimal combination of three bands was selected in order to obtain a better spectral separation between the different classes considered.

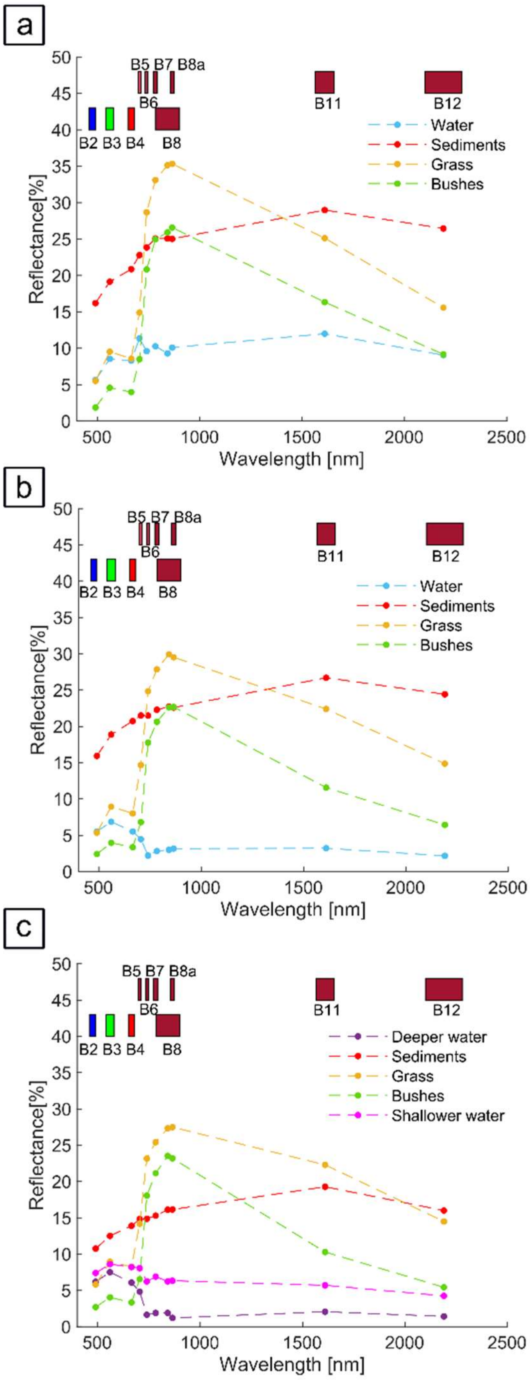

Figure 39: (a) Spectral signature of late spring condition, 14th June 2019;(b) spectral signature of winter condition, 6th February 2020; (c) Spectral signature of late autumn, 13th December 2021.

Figures 39a),b),c) show that the classes grass, bushes and water are indistinguishable in a RGB image, since red (B4), green (B3) and blue (B2) have very similar reflectance values. However, these bands allow to easily distinguish the mentioned classes from the sediments. In the NIR bands, the reflectance is more variable between different land covers. For example, in B8, the water and grass reflectance values are very different, while any sediment and bushes are still indistinguishable from each other (Figure 39a and Figure 39b). Only in autumn (Figure 39c), all the classes are distinct in B8, since the autumn sediment curve is lower than the spring (Figure 39a) and winter (Figure 39b) ones.

The literature spectral signature of the wet soil shown in Figure 5 (§ 2.2.3) has lower reflectance values than the literature spectral signature of the dry soil. It is possible that the lower reflectance values in the image acquired in autumn could be due to a higher water content in the sediments. In order to understand if the lowering of the reflectance values was due to a higher amount of water in the sediments, a control on the number of non-rainy days as well as on the number of rainfall events before the date of acquisition of the satellite was carried out. Specifically, it was observed that the June acquisition was preceded by 10 dry days, while those of February and December by only 4 and 1 dry day respectively. In addition, Figure 40 shows the rainfall pattern for the 30 days preceding the satellite acquisitions. It is also possible that the presence of more consecutive rainfall events led to a higher water content in the sediments. This observation opens up new prospects for future analysis on the possibility of distinguishing wet sediments from dry ones in multispectral images. What can currently be concluded is that as the water content increases, the sediment reflectance curve decreases, in agreement with the literature spectral signature shown in Figure 5(§ 2.2.3).

In the SWIR, both B11 and B12 allow to distinguish fairly well all the classes. Unfortunately, these two bands have a coarser spatial resolution (20 m) than the visible and B8 bands which are provided at 10m. Since the RGB images do not allow to differentiate adequately the land cover classes, it is more convenient to create false-colour images (FCI) through the composition of 3 bands to allow for a better distinction between classes. An optimal composition was obtained with the B4 band of the visible, B8 of the NIR and B11 of the SWIR. Despite the good capabilities of the SWIR bands for class separation, only one of the two were used, due to their coarser resolution. Of the two, B11 was chosen because it has a higher capability of distinguishing between vegetation (bushes and grass) and water in summer conditions. FCI can be created by SNAP tools. To facilitate a wider and easier use by non-specialized people, I created and made available a code on the platform Google Earth Engine (GEE) (https://code.earthengine.google.com/aaf0638466e4dc01cf8d61597490f2da.).

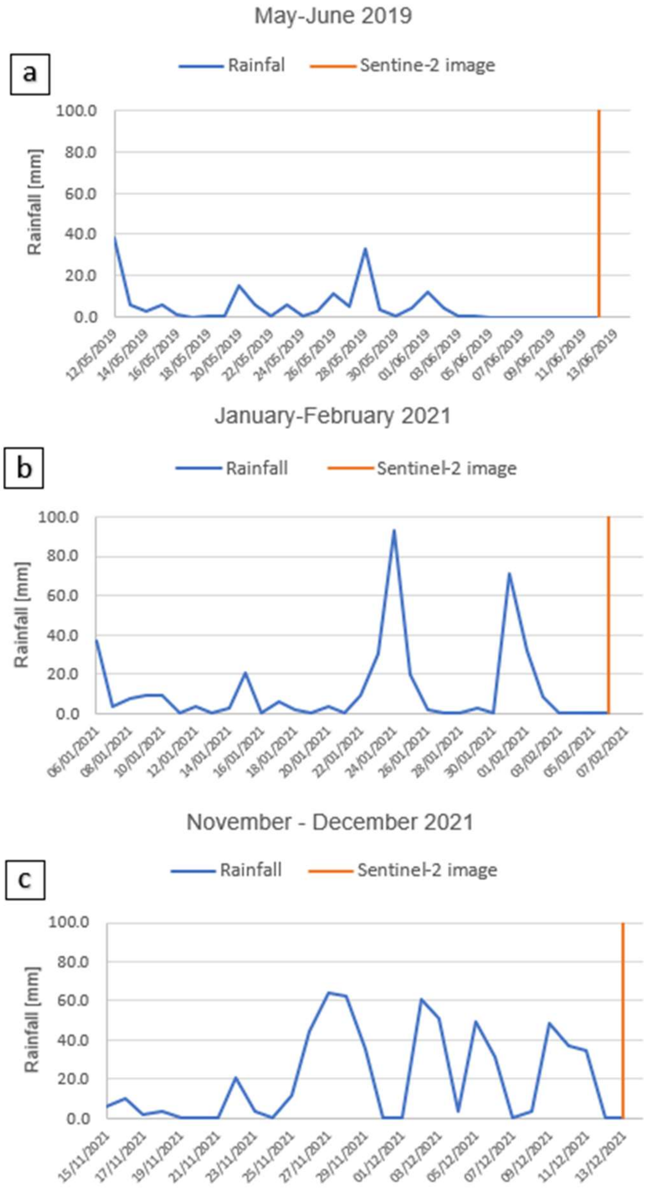

Figure 40: (a) Rainfall before of the 12th June 2019; (b)Rainfall before of the 6th February 2019; (c) Rainfall before of the 13th December 2021.

Examples of the FCI obtained by the composition of the bands 11, 8 and 4 and RGB are reported in Figure 44c and Figure 44b. In the FCI composition, the colour red was associated with B11, green with B8, and blue with B4. Consequently, the water is a black or dark blue colour, while the bushes are a green colour with decreasing intensity, in some cases almost tending to yellow, passing from thick vegetation to sparse vegetation. Grass is a yellow colour. The light pink colour, on the other hand, is associated with sediments or soil without vegetation cover. In some situations, e.g., dry or large sediments, the sediments can also take on a white colour (see Figure 44c). It can be seen that in the FCI, the presence of water can be distinguished much better than RGB (see Figure 44b and 44c).

Non-perennial rivers are characterized by patterns of zero or low flow, with dry stream beds or chains of isolated ponds of water.

Exploiting the FCI, it is possible to distinguish three different conditions: 1. “flowing” the water flow is longitudinal continuous (Figure 41a), 2. “ponding” there is no flow but only disconnected water ponds (Figure 41b), and 3. “dry” the riverbed is completely dry or the water ponds are too small to be detected (Figure 41c).

Figure 41: Flow conditions: (a)Flowing, (b)Ponding, (c) Dry Bed.

The spectral signatures in Figure 39 show the average reflectance values for each band, but to identify an automatic classification method of the land cover classes, it is advisable to evaluate the separability among the various classes in the different bands. The analysis considers the distribution of the reflectance values for all the bands and for each class.

From the analysis shown in Figure 39, the spectral signatures of spring and winter have similar mean values, so the separability analysis was carried out only in two different seasonal flow conditions: in late spring (June 2019) and late autumn

(December 2021). Figure 42 illustrates the distribution of the reflectance values for the land cover classes of June 2019 in the Sentinel-2 spectral bands.

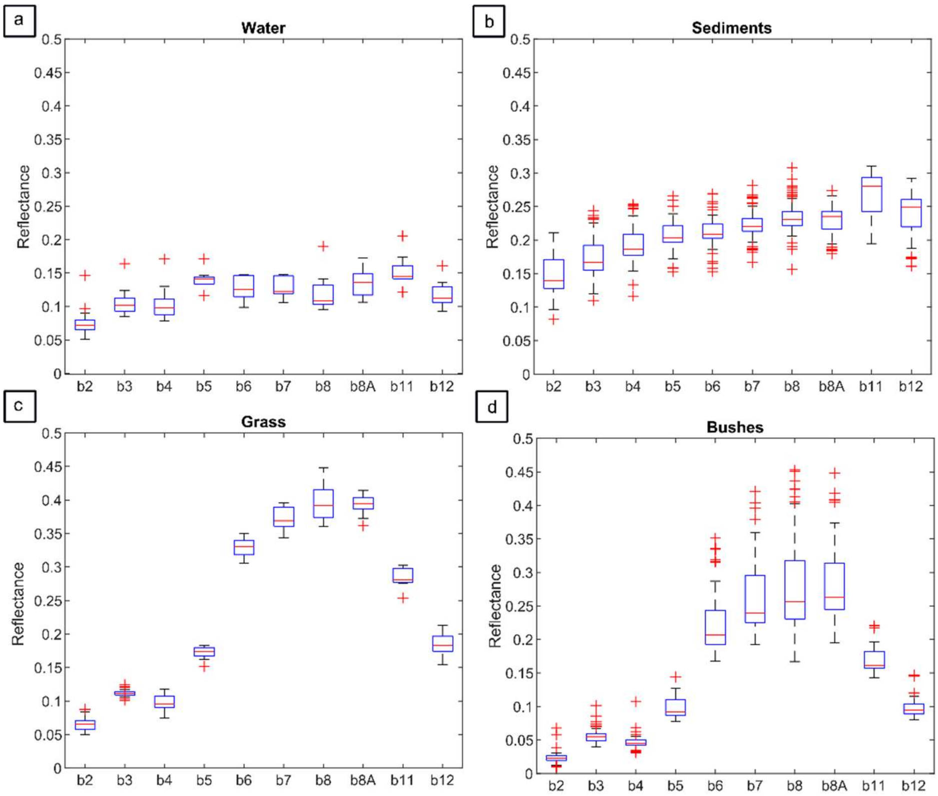

Figure 42: Distribution of land cover classes for multispectral bands, 14th June 2019.

Figure 43 illustrates the distribution of the reflectance values for the land cover classes in the Sentinel-2 spectral bands of December 2021. As mentioned before, in this case having a drone survey, which provides more detailed images, it was possible to divide the shallower and deeper water classes.

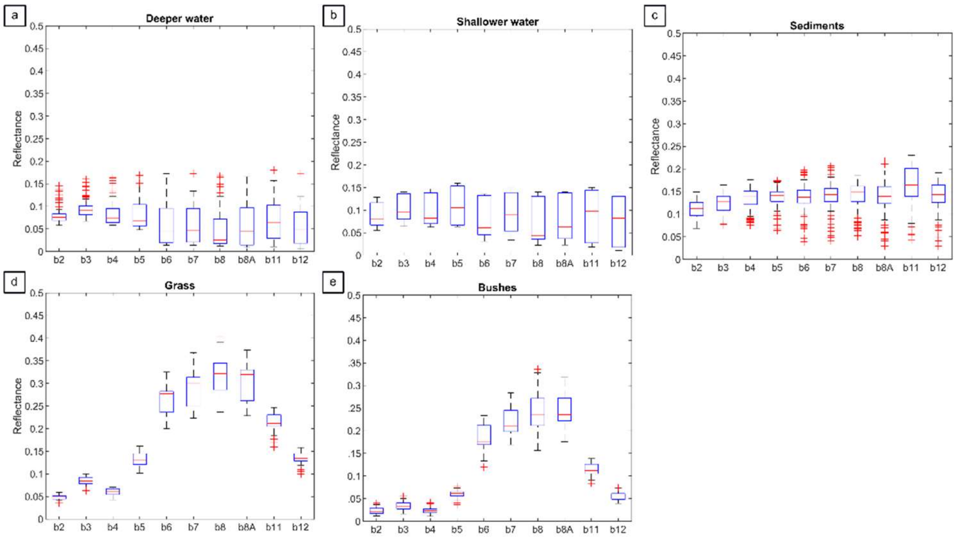

Figure 43: Distribution of land cover classes for multispectral bands, 13th December 2021.

As can be seen from Figures 42a, 43a and 43b, the water class has similar reflectance values in the different bands, making classification based on multispectral indices difficult. In these cases, it is not possible to exploit the multispectral indices to identify the presence or absence of water. In addition, the water shows a very unstable behaviour, for example in June, as already shown in Figure 39, and discussed above, the reflectance in the infrared bands is higher than the reflectance in the visible bands, but with rather low variance values. In December, in contrast, there is always a higher reflectance in the infrared wavelengths in shallower water than deeper water conditions, but in both cases, high variances are observed. Comparison with the other classes shows that the water class has a higher separability in the infrared regions, except when the sediment has a higher water content, in this case the reflectance values of the wet sediment are closer to that of the water. For the bushes and grass classes, the difference between the reflectance values in the infrared and visible bands is very marked as shown in Figure 42c-d and 43-d-e, and facilitates the implementation of multispectral indices, such as *NDVI*.

6.3 Performance estimation: FCI vs VHR images and field surveys

To assess the accuracy of the observed flow condition from the S2 derived FCI, several test comparisons were made with the ground truths introduced in § 6.1.5. The tests are summarized in Table 16. It is worth noting that the filed surveys and the orthophoto are contemporary with the S2 acquisitions, while the Google Earth Pro image was acquired two days after the coupled S2 one. Given the absence of precipitation in this short interval of time, it can be assumed that there is no significant change of the water presence. The set of ground truths used provides a fairly complete picture of the various seasonal flow conditions.

Table 16: Pairs of S2 and ground truth images

Test case	**Ground truth source**	**Ground truth date**	**Sentinel-2 date**	**Study Reach**
1	Google Earth Pro	14 June 2019	12 June 2019	M1, M2, M3, L1
2	Field survey	26 June 2020	26 June 2020	S1
3	Field survey	26 July 2020	26 July 2020	S1
4	Field survey	19 September 2020	19 September 2020	S1, M3
5	Field survey	6 February 2021	6 February 2021	M1, M3, S1
6	Drone	13 December 2021	13 December 2021	M3, S1

For the sake of brevity, only a selection of these is shown in the following. Figure 44 shows test n°1 for the M1 reach. It can be seen that the FCI is very effective in highlighting the wet channel, which is seen very clearly and in good detail. Despite the much coarser resolution of the FCI (Figure 44c) compared to the VHR (Figure

44a) the wet channel is still visible almost as clearly. The continuous flow condition "flowing" can be clearly identified.

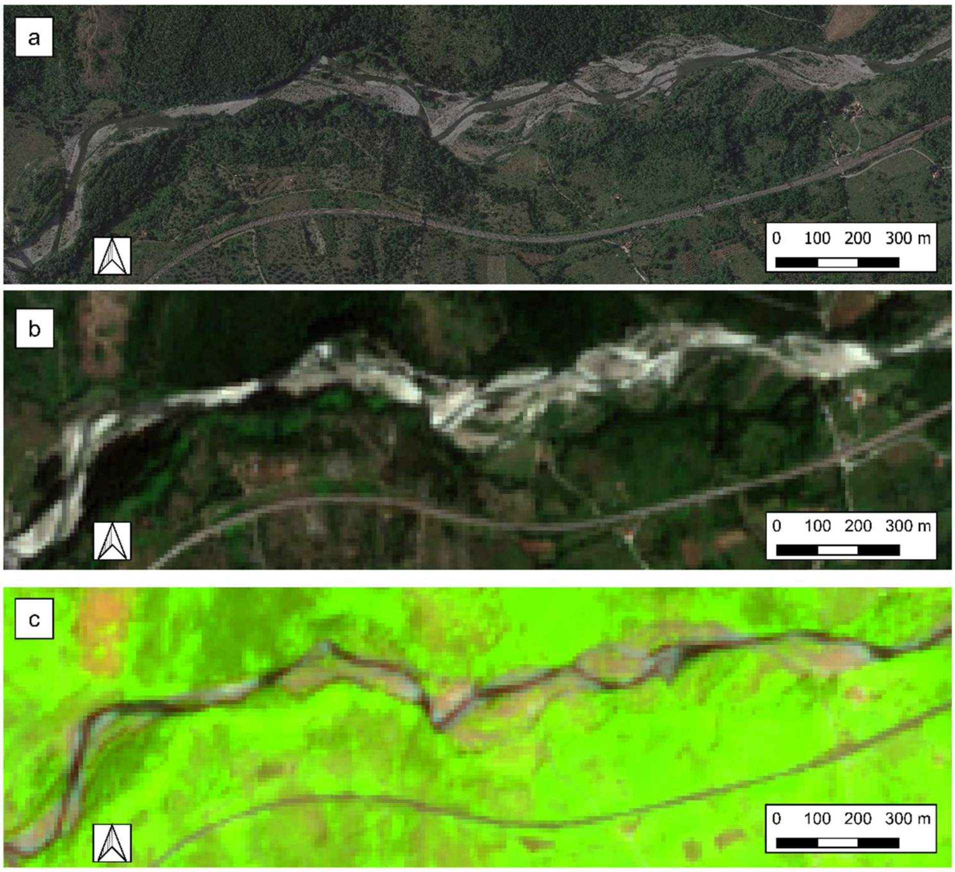

Figure 44: Test case n°1, M1 reach, (a) Google Earth Pro VHR image acquired on 14th June 2019, (b) RGB extracted by Sentinel-2 acquisition of 12th June 2019 and (c) FCI extracted by Sentinel-2 acquisition of 12th June 2019.

Figure 45 shows an example of the spatial evolution of the flow conditions, test case n° 4 is shown for the reach M3 and for a reach downstream of it. On this date, the upstream reach is completely dry as confirmed by the geo-localized picture c1. In the downstream part, in correspondence to the picture c2, it is possible to notice, both in the FCI and ground picture, an elongated pond in correspondence to the left bank of the riverbed. Immediately downstream, in the reach framed by picture c3, a wet channel can be seen in the FCI which is confirmed in the ground picture. It can be seen that the FCI allows for a clear distinction between the different flow conditions that occur along the riverbed.

A possible source of misclassification is the presence of the bridge, which in this case takes on a colour similar to water. However, the structural elements that cross rivers are well known and can be identified a priori.

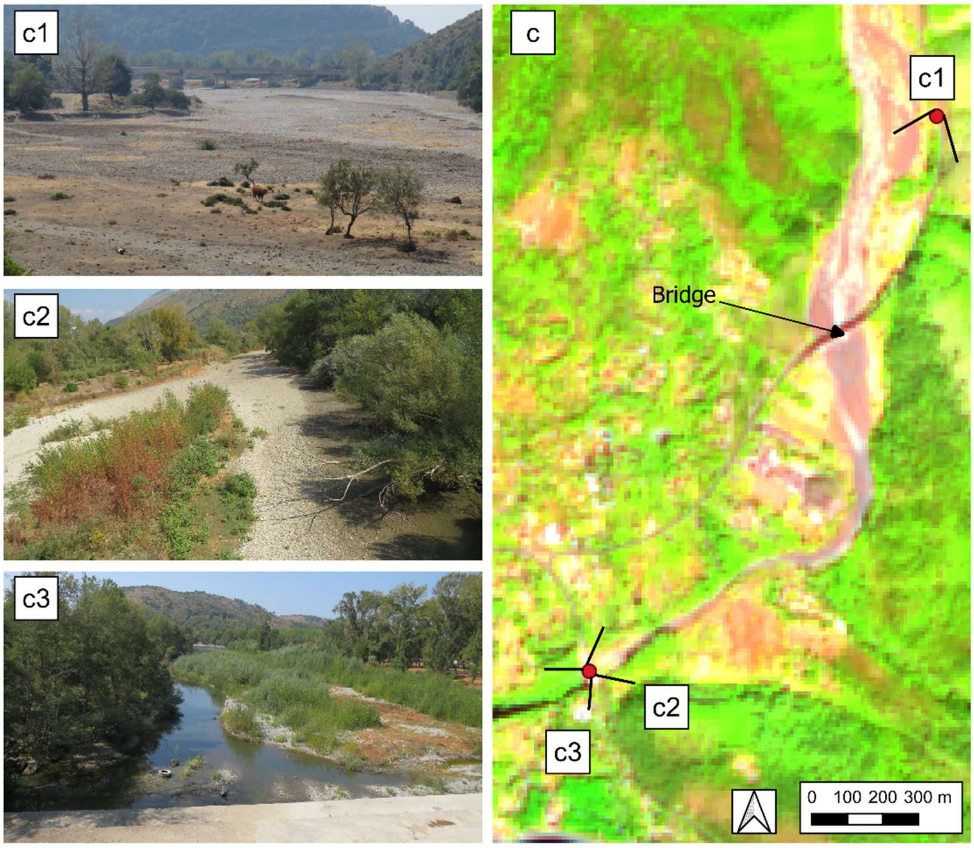

Figure 45: Tast case n° 4, M3 reach, (c) FCI extracted by Sentinel-2 image of 19th September 2020 with the geolocation points of the pictures, (c1), (c2) and (c3) geo-located pictures take on 19th September 2019.

Figure 46 shows a temporal evolution of the S1 reach, from tests 2 (26th June 2020), to 4 (19th September 2020) and 5 (6th February 2021). The FCIs of Figure 46a, b and c and the corresponding ground pictures of Figure 46d, e and f show the temporal evolution of the water presence. On 26th June 2020, the FCI shows a ponding condition which is confirmed by the ground picture. In particular, the pond visible from the picture (Figure 46d) is recognizable in the FCI (Figure 46a) despite the very small size. In September 2020, at the end of the summer dry season, the bed is completely dry (Figure 46b and e). In the February 2021 FCI (Figure 46c), we see a continuous flow line (flowing condition) confirmed by the contemporary surveys (Figure 46f). The pictures shown in Figures 46d, 46e and 46f were taken from a road adjacent to the S1 reach.

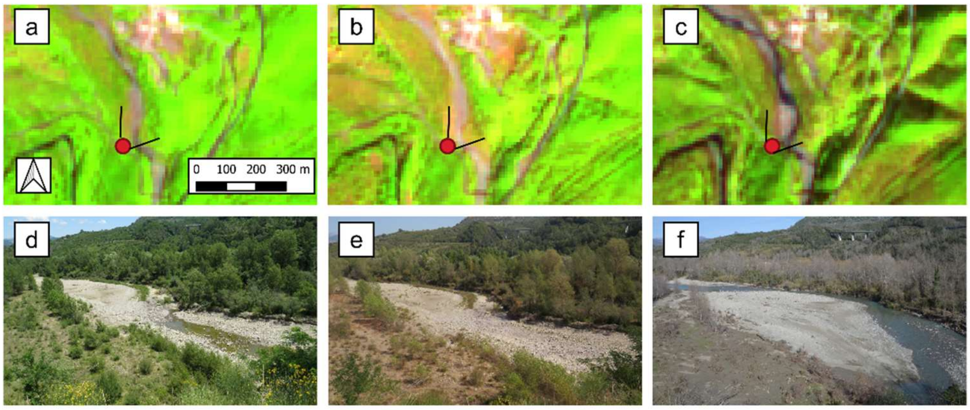

Figure 46: Test cases 2,4,5, S1 reach, a) FCI of 26th June 2020, b) FCI of 19th September 2020, c) FCI of 6th February 2021, (red point) pictures shooting location, d) picture taken on 26th June 2020, e) picture taken on 19th September 2020, and f) picture taken on 6th February 2021.

Figure 47 shows tests 2(June 2020), 3 (July 2020) and 5 (February 2021) for the S1 reach. Figure 47.a1 shows the picture taken in correspondence to a pond with a length greater than 50 m and a width less than 5 m. In the FCI, this pond is not distinguishable due to the width smaller than the pixel size (Figure 47.a). While the images 47.a2 and 47.a4 show ponds with a width greater than 10 m, which are clearly visible in the FCI of June 2020 (Figure 47.a). The images 47.b2 and b4 show the pictures taken on 26th July 2020 in correspondence to the same points of the images 47.a2 and 47.a3. In July (see Figures 47.b2 and 47.b4), the ponds were almost dry, and their size was too small to be identified in the corresponding FCI. In the interval between the two acquisition dates, the total rainfall was equal to 44.2 mm and the average temperature value was equal to about 24 ° C. This means that a total rainfall equal to 44.2 mm and an average temperature of 24 ° C did not contribute to maintaining a ponding condition, or to a reflowing condition along the reach, but resulted in a transition from a ponding condition to a dry bed condition. Figures 47.b3 and 47.c3 show the pictures taken from the same point, where picture 47.b3 shows the dry bed condition of July and the picture 47.c3 shows the flow condition of the February, both correctly identified in FCIs (Figure 47.b and 47.c). The picture in Figure 47.c5 was taken in correspondence to the wet channel with a width of 20 m, while the picture in Figure 47.c6 was taken in correspondence to the wet channel with a width of 9.4 m. Observing Figure 47c, it is possible to note that where the wet channel has a width of about 20 m (Figure 47.c5), it is possible to identify the presence of water in FCI (Figure 47.c), while, when the width of the wet channel is lower (Figure 47.c6), in this case about 9.4 m, it is not possible to clearly distinguish the presence of the wet channel in FCI (Figure 47.c).

Figure 48 shows test case 6 for the M2 reach. On this date, the flow condition is well recognised and there is a good congruence between the orthophoto and FCI. It is worth noting that in the winter period in the FCI, shadows due to the presence of bridges or trees, located in the vicinity of the riverbed, can be classified erroneously as water. However, this problem can only affect small areas and therefore the presence of shadows interferes little or nothing with the presence of water in the channel. In Figure 48, the presence of shadows does not affect the identification of the flow condition. The shadow problem could lead to misclassification issues in the summer period, because the shadow could be easily confused with a pond of water. However, it has been observed that this problem is encountered more in the winter period than in the summer period, because in the summer period, the position of the sun is higher and shadows are less frequent.

The analysis described in this paragraph has shown that the minimum width of ponds identifiable by FCI is highly variable. In some cases, it is even possible to identify ponds with widths between 6 m and 10 m. In other conditions, however, ponds or wet channels larger than 10 m and less than 15 m are not clearly identifiable. This depends on the relative position of the object with respect to the pixels.

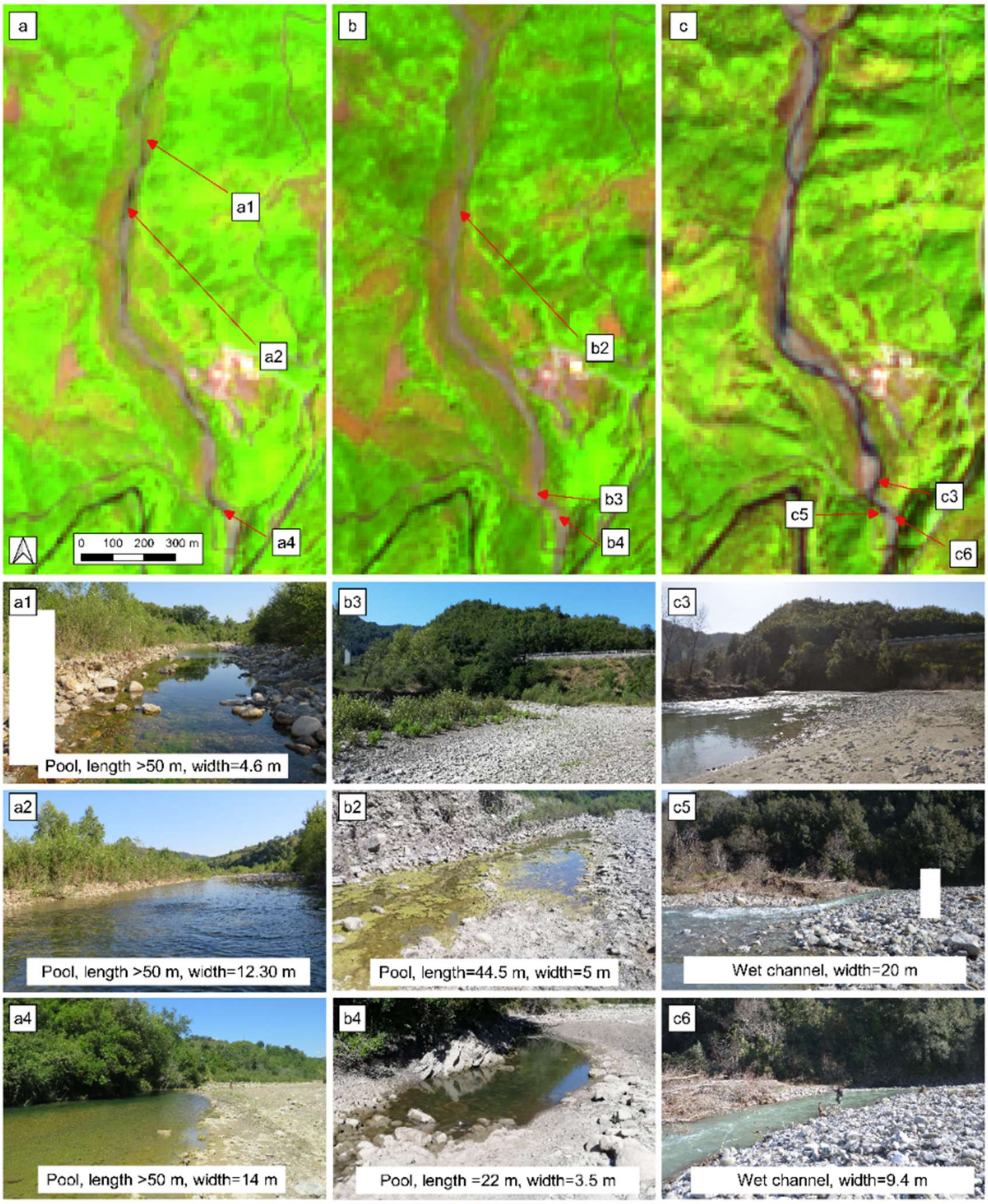

Figure 47: (a) Test cases 2,3,5, S1 reach, (a) FCI of 26th June 2020, (b) FCI of 26th July 2020, (c) FCI of 6th February 2021, (a1, a2 and a4) picture taken on 26th June 2020, (b2, b3, b4) picture taken on 26th July 2020, and (c3, c5, c6) picture taken on 6th February 2021.

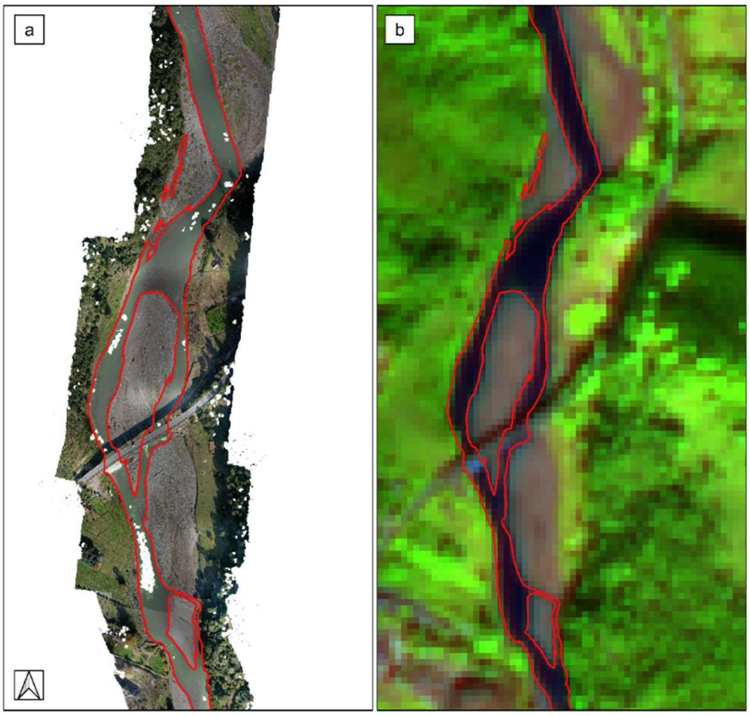

Figure 48: Test case 6, M3 reach, (a) Orthophoto acquired by UAV of 13th December 2021 and (b) FCI in same date.

6.4 Automatic classification of Land Cover Classes

To automate the flow regime classification process, it is necessary to develop an automatic classification method to extract the wet channels and ponds. Based on this mapping, an automatic algorithm could be developed capable of defining the corresponding flow condition. However, this is challenging due to the narrow width of the wet channels and water ponds. In these environments, the size of an object may be comparable to the pixel size, or the object even though larger than the spatial resolution may fall within two or many pixels and occupy only a portion of them. When many pixels contain several objects (mixed pixels), that in the case of the fluvial environment could be bed material, water and vegetation, the combination of multiple reflectance values can make the pixel appear like another type of surface and thus be misinterpreted.

As noted in the previous paragraph, identifying the presence of water is complicated even in a true colour visualization (RGB), and the automatic classification being a real challenge.

The characteristics and properties of various land cover classes can be effectively studied by measuring the spectral response in different parts of the electromagnetic spectrum. To implement an automatic classification method, it is important to investigate the different spectral bands to see which provide the best separability for the land covers classes.

Based on the analysis carried out in §6.2, two automatic classification methods were developed: Spectral Signature Minim Differences (SSMD) and threshold-based method. These classification methods were implemented in original codes in Matlab language.

Considering that the vegetation (grass and bushes) shows a marked difference between reflectance values in the visible and infrared bands, it is possible to calculate the *NDVI* index and identify the presence of vegetation by applying a threshold equal to 0.4 (Holben 1986, Rutkay et al., 2020). Once the vegetation pixel was separated, two methods were developed to distinguish water from sediment in the remaining pixels.

6.4.1 Spectral Signatures' Minimum Differences

Considering the various classes (j): sediments, deeper water and shallower water. For each pixel (i), the distance between the pixel's reflectance value and the spectral signatures shown in Figure 39 is calculated. The pixel (i) is assigned to the class j for which the difference d(x) is minimum. From the analysis, it was observed that the presence of the shallower water spectral signature during some winter dates leads to classifying the sediments as water. It has been seen that the classification improves if, during the winter period, only the spectral signature of deeper water is taken into consideration, and to consider the spectral signature of the shallower water or both water spectral signatures in the summer period. Figure 49 shows the results for all the test cases of Table 16. As can be seen from Figure 49, the classification is able to correctly identify the presence of water, sediments and vegetation for the various dates. For the winter images 50j and l, only the spectral signature for deeper water was used, otherwise the presence of both water spectral signatures would have misclassified the sediments. Sediments during some winter dates may contain more water, and the reflectance values may be lower and closer to shallower water reflectance values. Not considering the spectral signature of shallower water reflectance in the winter period allows for the correct classification of sediments and water.

This problem does not seem to be encountered in the summer period. It is possible that the high temperatures and/or the possible lowering of the water table could lead to a lower water presence in the riverbed.

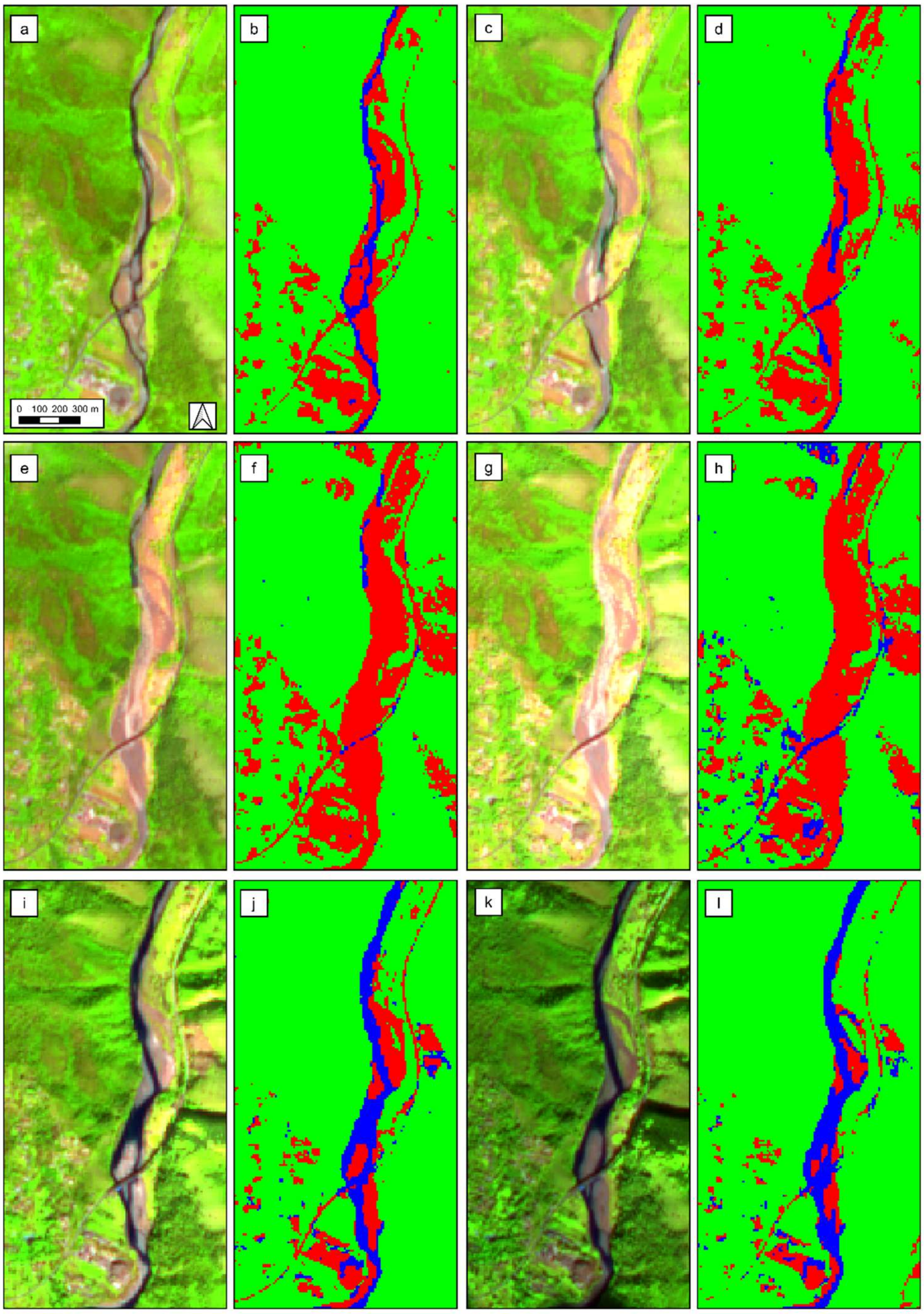

Figure 49:SSMD, (a,c,e,g,i,m) FCI images of 12 th June 2019, 26 th June2020, 26 th July 2020, 19 th September 2020, 6 th February 2021 and 13 th December 2021; (b,d,f,h,l,n) automatic classification method for the M1 reach.

6.4.2 Threshold based method

In the second method, the water and sediment classes were separated by applying a threshold on the B8 band equal to 0.21. The choice of the threshold was made based on the separability analysis shown in Figure 42.

Figure 50 shows a comparison between the land cover classification and the FCIs for all the test cases of Table 16. It can be seen that the results of the classification shown in Figure 50 b, d, h and j, are congruent with the FCI (Figure 50a, c, g and i). In Figure 50f and l, in some areas, the soil is wrongly classified as water, and in these cases, the threshold value on B8 should be lowered in order to make the classification consistent with the FCI (Figure 50 e and k). In this case, except for some dates, the classification method allows to correctly identify the presence of water, sediments and vegetation.

Both classifications could be used as starting points for the implementation of an automatic classification method for the identification of the various flow conditions. With the first method, the classification is consistent with the FCI, and the implementation of a method of automatic identification of the various flow conditions would allow their correct identification. In the second method, the classification in Figure 50f allows for the identification of the ponding phase but the classification is not perfectly consistent with the FCI.

The misclassification of sediments as water in Figure 50f would lead to think that on 26th July 2020 the sediments have a higher water content. Table 17 shows the days in the absence of rainfall that precede the acquisition dates. From this analysis, it would not appear that the threshold instability is due to the water content in the sediments. It is likely that the instability of the threshold value is due to other aspects that need to be further investigated.

Table 17: Days in the absence of rainfall preceding the satellite acquisitions.

Test case	Images	Days in the absence of rain
12 June 2019	a,b	10
26 June 2020	c,d	13

26 July 2020	e,f	8
19 September 2020	g,h	1
6 February 2021	i,j	4
13 December 2021	k,l	1

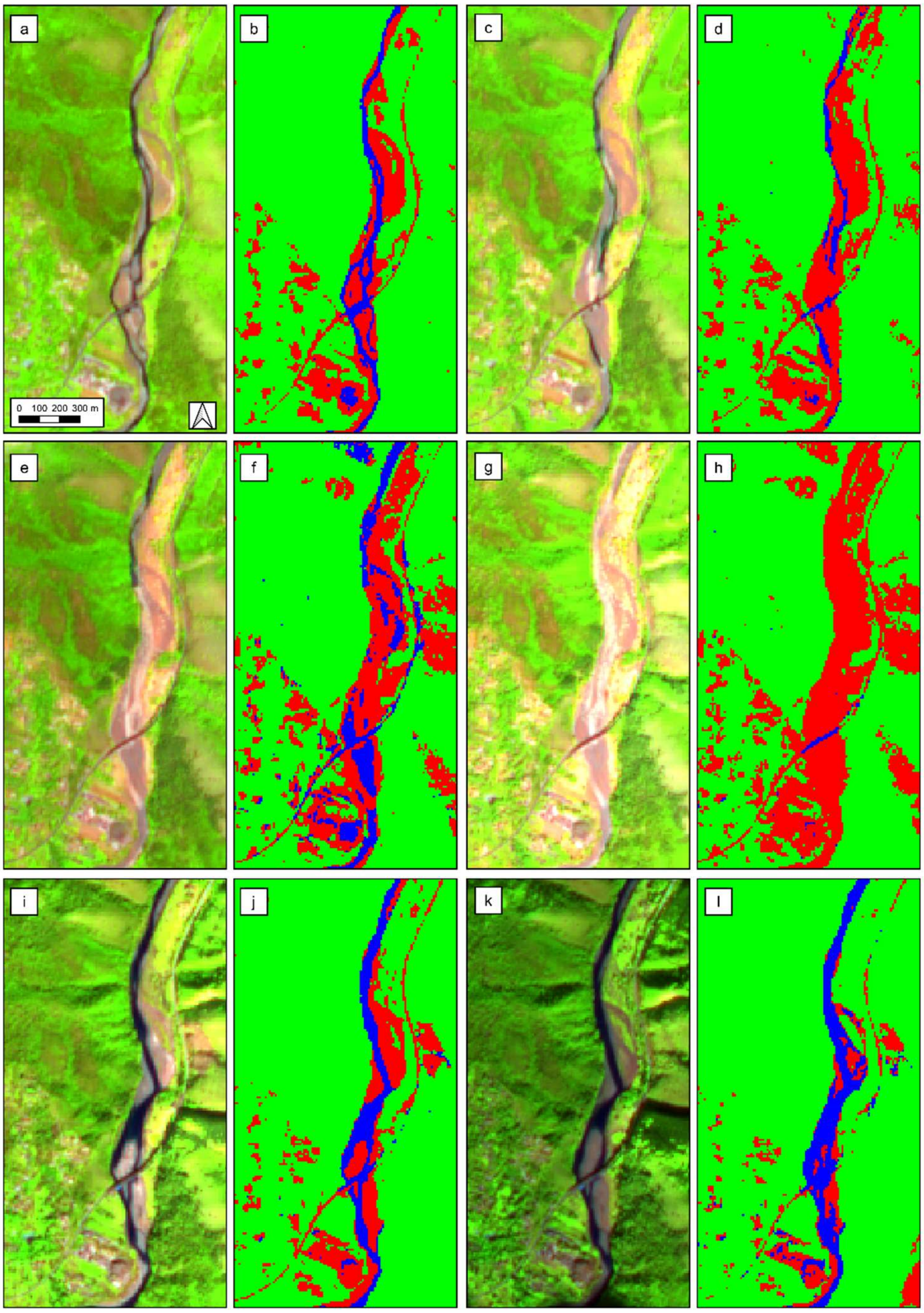

Figure 50:Threshold based method: (a,c,e,g,i,m) FCI images of 12 th June 2019, 26 th June 2020, 26 th July 2020, 19 th September 2020, 6 th February 2021 and 13 th December 2021; (b,d,f,h,l,n) automatic classification method for the M1 reach.

6.5 Flow conditions observed

The FCI was calculated for the entire S2 images archive, and the flow condition was identified for all the reaches studies. Figures 51, 52, 53, 54 and 55 show the results of the observed regime for the S1, M1, M2, M3 and L1 reaches.

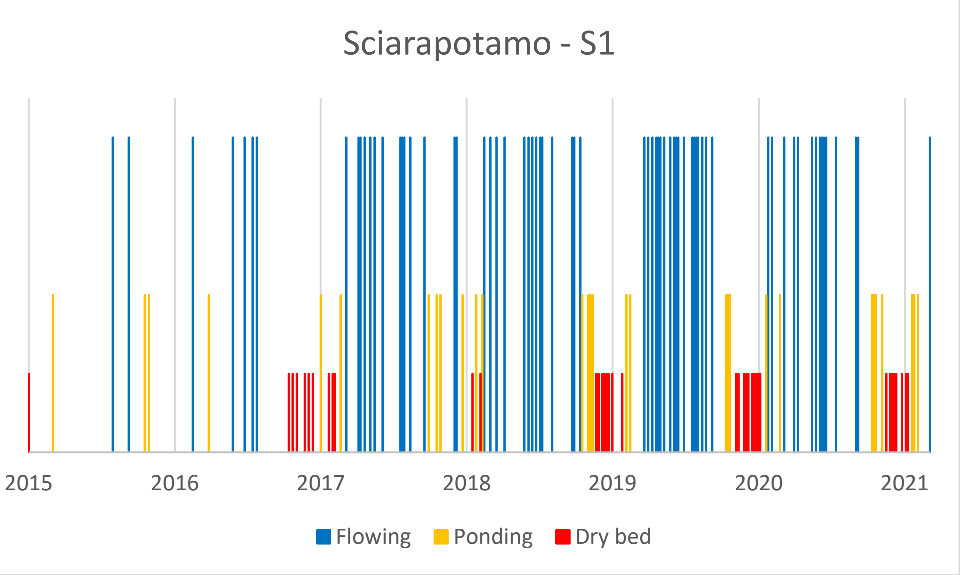

Figure 51: Flow conditions observed for the S1 reach.

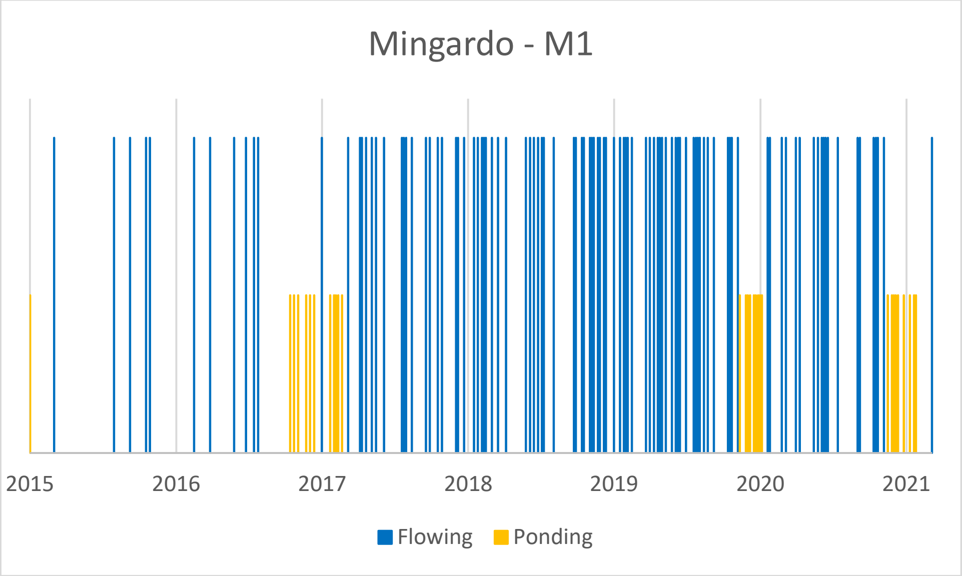

Figure 52: Flow conditions observed for the M1 reach.

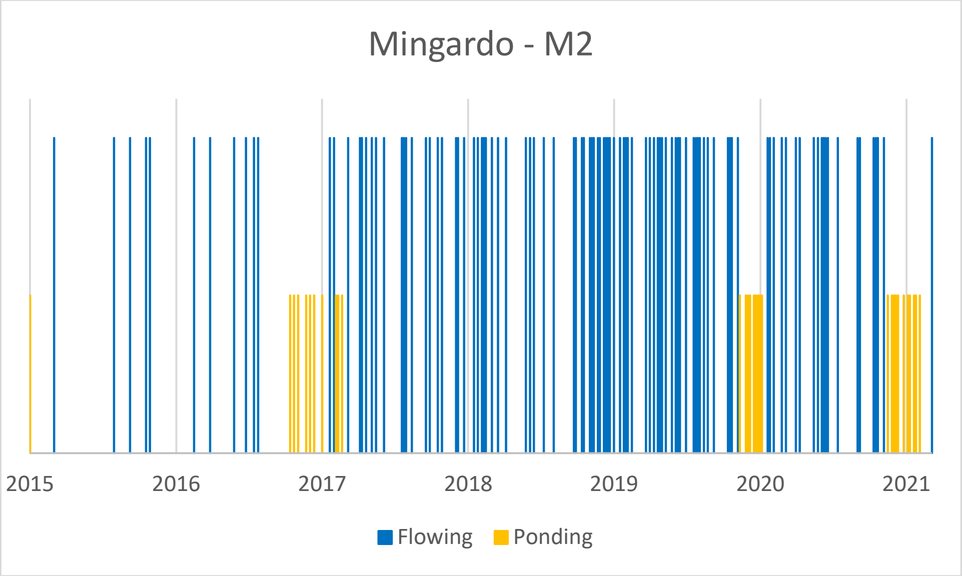

Figure 53: Flow conditions observed for the M2 reach.

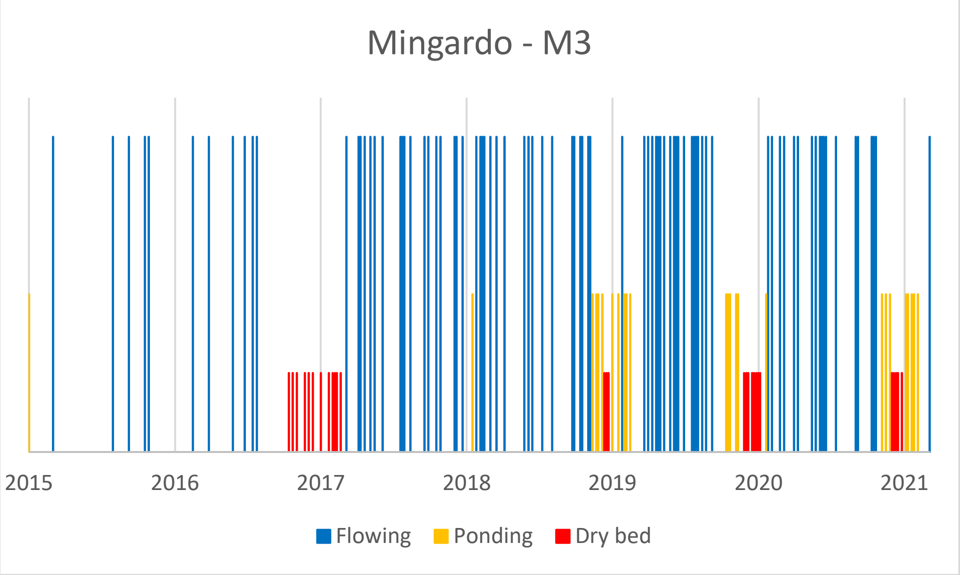

Figure 54: Flow conditions observed for the M3 reach.

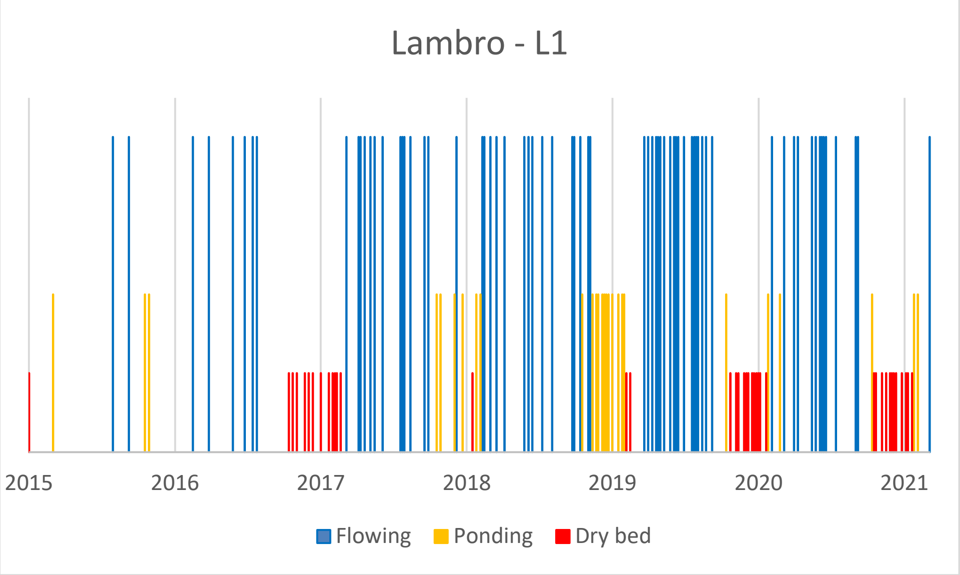

Figure 55: Flow conditions observed for the L1 reach.

Figures 51,52,53,54,55 show how the duration of the flowing and non-flowing period follows a seasonal pattern. In general, the transition from flowing to non-flowing conditions occurs in late June or the beginning of July. For the M1 and M2 reaches, a dry-bed period never occurred during the observation period, the local hydrogeological conditions are probably such as to always guarantee the presence of water inside the reaches. Although the M2 and M3 reaches are consecutive (see Figure 38 in §6.1), with very similar catchment areas, and almost similar rainfall and temperature values, the two studied reaches show very different hydrological regimes.

For the S1, M3 and L1 reaches, the dry bed period generally begins in August, except in the year 2017, for which the dry condition occurs as early as the end of June. The dry bed period generally lasts about two months and extends almost until the end of October, or, as in the case of 2017 for the L1 and M3 reaches, it can be extended until the beginning of November. In some cases, it can be observed that the dry condition changes directly to a flowing condition. Obviously, this direct transition from dry to flowing can be considered true as there may be a rain event and temperatures that result in a direct transition from a dry bed to a flowing condition; or there may be a ponding condition between the two images acquired that cannot be identified.

6.5.1 Duration of flow conditions

Given the results obtained in the previous paragraph, it is possible to determine the duration of the flowing, ponding and dry bed conditions for all the reaches, as well as for each hydrological year. Considering three consecutive days: ti-1, ti and ti+1, in which the satellite acquisitions are available and therefore the flow conditions are known, the duration of the condition observed in ti is equal to (ti-(ti-1))/2 + ti+1-ti)/2. This method can be called: "*average interval method*", to differentiate it from the one that will be presented in § 6.7. Figures 56-60 show the duration of the three flow conditions obtained from the mid interval method. Figures 56,59 and 60 show the duration of the non-flowing and dry bed period for the S1, M3 and L1 reaches, while Figures 57 and 58 show only the duration of the non-flowing phase, because, as already mentioned in the previous paragraph, a dry bed condition has never been assessed for the M1 and M2 reaches.

Given the limited number of images (only 6) in the year 2015 and early 2016, it was decided not to consider this year in the analysis of the duration obtained from the satellite images. The limited number of images in this period is attributed to an initial period of operation and settling of the S2-A satellite, launched on 23rd June 2015.

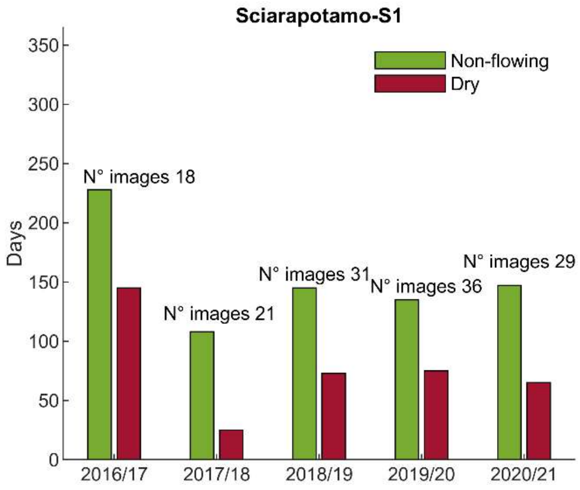

Figure 56: Number of days of non-flowing (green) and number of days of dry bed(red) extracted by mid interval method, in the S1 reach.

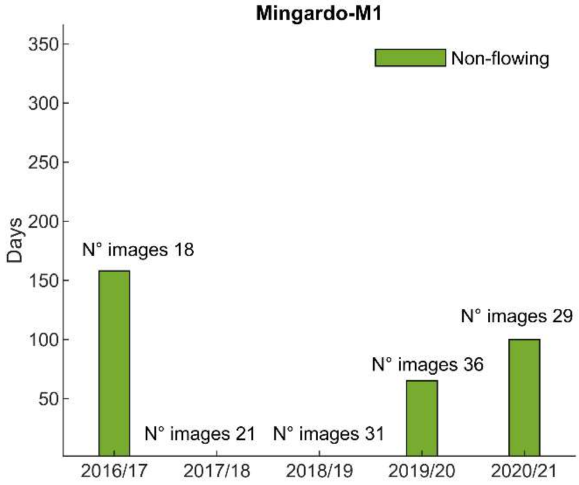

Figure 57: Number of days of non-flowing (green) extracted by mid interval method for the M1 reach.

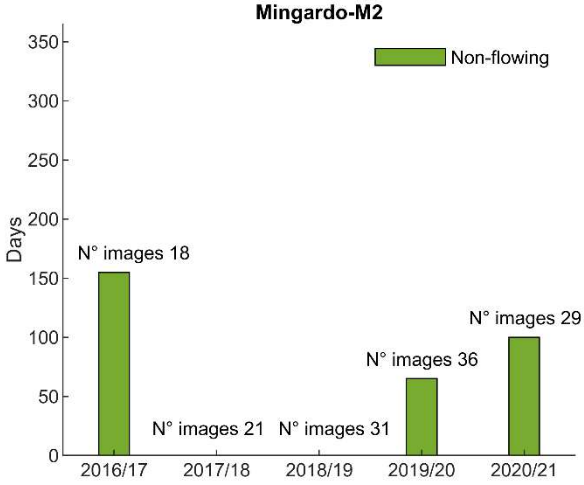

Figure 58: Number of days of non-flowing (green) extracted by mid interval method for the M2 reach.

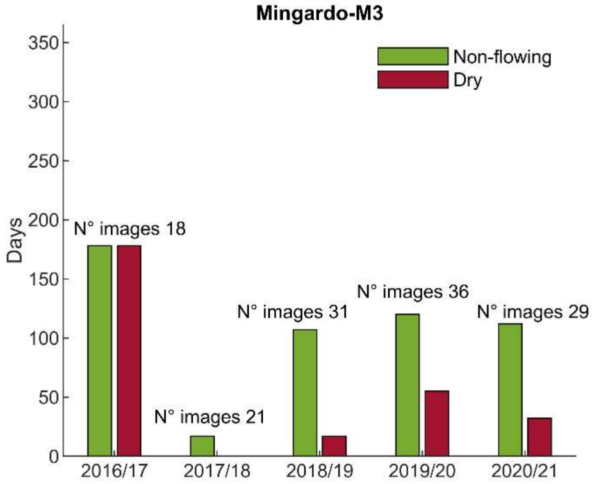

Figure 59: Number of days of non-flowing (green) and number of days of dry bed(red) extracted by mid interval method for the M3 reach.

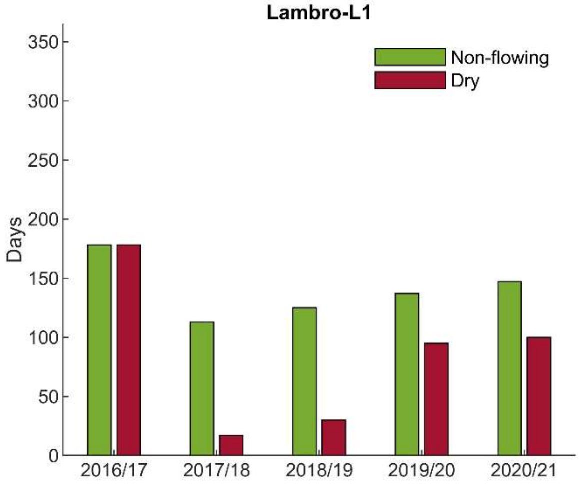

Figure 60: Number of days of non-flowing (green) and number of days of dry bed(red) extracted by mid interval method for the L1 reach.

The longest duration of the non-flowing or dry-bed periods was observed in the year 2016/2017 for all the reaches studied. This longer duration is also reflected by the drought analysis conducted in Campania by Longobardi et al., 2021, which showed that a severe drought period, in recent years, in 2017. The year with a shorter non-flowing duration is the year 2017/2018 for all the reaches studied.

6.6 Prediction of the daily flow conditions with a Random Forest model

As part of the research collaboration with the working group of the Polytechnic of Turin, and in particular with Professor Paolo Vezza and the PhD student Giovanni Negro, the results of the classification of the flow conditions shown in the previous paragraph were used to calibrate a forecast model. To predict the daily occurrence of the specific flow condition (flowing, ponding, dry bed), the dataset obtained from the Sentinel-2 images was used to train a random forest (RF) classification model using the spatially interpolated predictors of the daily time series of precipitation (R) and maximum, mean and minimum temperature (T_MAX, T_MEAN and T_MIN) introduced in §6.1.4.). For the Cilento, Vallo di Diano and Alburni National Park these data were available from 2015 to 2021, and they were spatially interpolated at the catchment scale by Thyssen polygons. Two binary classification RF models were developed to distinguish between non-flowing/flowing (NF/F) and dry/ponding (D/P) events. The RF models were developed both on a single reach (L1, S1, M1, M2 and M3) and globally (G, all the reaches together). To address the potential bias in class distribution due to the unbalanced dataset, classification models were developed using the random oversampling of the training dataset.

In the two binary RF models, the daily time series of precipitation (R) and T_MAX, T_MEAN, T_MIN, from 2015 to 2021, spatially interpolated at the catchment scale for each river reach, were considered as the predictor variables of the flow conditions. In addition, to explore different time scales, the cumulative rainfall and the average value of the T_MAX, T_MEAN, T_MIN of the previous days were considered, using 3-5-7-10-30-90 days as time intervals. Thus, a total of 28 predictor variables were included in the Random Forest classification method, using the following codes: R3, R5, R7, R10, R30 and R90, for the rainfall variables and T3_,

T5_, T7_, T10_, T30_, T90_MAX, MEAN, MIN for the temperature variables. The predictive performances of the developed RF models were evaluated by calculating the number of True Positive (*TP*), False Positive (*FP*), True Negative (*TN*) and False Negative (*FN*) and using four performance parameters, *Accuracy* (*A*), *Sensitivity* (*S*), *Specificity* (S^*) and *True Skill Statistic* (*TSS*).

$$Accuracy = \frac{TP + TN}{TP + FP + TN + FN} \tag{11}$$

$$Sensitivity = \frac{TP}{TP + FN} \tag{12}$$

$$Specificity = \frac{TN}{FN + TN} \tag{13}$$

$$True\ skill\ statistic = Sensitivity + \ Specificity - 1 \tag{14}$$

The analysis showed that the binary RF models developed can predict a specific flow condition (flowing/ponding/dry bed) occurring on a daily scale in each river reach (see Table 18). It is worth noting that since for reaches *M1* and *M2* a dry condition has never been assessed by the analysis of satellite images, only the NF/F model has been considered for these reaches.

As can be seen from the results shown in Table 18, the validation of the oversampled RF models showed very high predictive abilities. Overall, the NF/F models performed better than D/P models, with an accuracy ranging from 0.94 to 0.98 and *TSS* ranging from 0.88 to 0.95. For the D/P models, accuracy and *TSS* showed slightly lower scores ranging from 0.82 to 0.92 and 0.64 to 0.84 respectively. In general, for the NF/F models, the sensitivity (ranging from 0.94-1.0) was higher than the specificity (ranging from 0.89-0.96), except for the *S1* reach. On the other hand, for the D/P models, the sensitivity (ranging from 0.77 to 0.92) was found to be lower than the specificity (ranging from 0.86 to 0.92). In addition, the global models (*G*) were generally slightly less accurate in predicting the correct flow condition than the models calibrated at the reach scale. The global models showed the lowest scores, except for the D/P model for the *M3* reach.

Table 18: Predictive variables and performances obtained for the oversampled RF models.

Binary model	**Scale**	**Predictive variables**	***A***	***S***	***S****	***TSS***
NF/F	***G***	R90, T90_MAX, R10	0.94	0.98	0.90	0.88
	S1	T90_MEAN, R30, R10	0.95	0.94	0.96	0.90
	M1	R90, R10, T90_MAX	0.95	1.00	0.91	0.91
	M2	R90, T90_MAX, R10	0.95	1.00	0.89	0.89
	M3	R90, T90_MAX, R10	0.98	0.99	0.96	0.95
	L1	T90_MAX, R90, R10	0.96	0.99	0.94	0.93
D/P	***G***	R90, R30, T30_MAX	0.84	0.81	0.87	0.67
	S1	T90_MEAN, R90, R30	0.92	0.92	0.92	0.84
	M3	R90, T30_MAX, R30	0.82	0.77	0.86	0.64
	L1	R90, R30, T90_MAX	0.88	0.87	0.90	0.77

In Table 18, the model variables are listed in terms of decreasing importance for the classification result (from left to right). The cumulative 90-days rainfall (R90) was significant in 90% of all the models and was the most important predictor in 70% of them. The cumulative 10- and 30-days rainfall (R10 and R30) were important predictors for distinguishing between the NF/F and D/P conditions in 100% of the models, and R30 was evaluated as a significant predictor for the NF/F model of the *S1* reach. The T90_MAX showed greater importance especially considering the NF/F models where it is present in 5 out of the 6 cases. On the other hand, T90_MEAN was established as a predictor variable for both the binary models of the *S1* reach, and T30_MAX was found to be a significant predictor for the D/P models in the global (*G*) and *M3* reach.

6.7 Duration of the flow conditions

The knowledge of flow intermittence patterns is essential for many applications such as the implementation of the correct management policies and definition of the ecological status. Once the daily occurrence of each flow condition had been estimated by the RF model, it was possible to determine the duration of the non-flowing and dry bed conditions for all the reaches, as well as for each hydrological year.

Figures 61-65 show the non-flowing or dry bed days calculated from the prediction of the RF model. Figures 61,64 and 65 show the duration of the non-flowing and dry bed periods for the S1, M3 and L1 reaches, while Figures 62 and 63 show only the duration of the non-flowing condition.

Given that in the year 2021, the prediction of the RF model for the M1, M2 and M3 reaches cannot be used due to a temperature value not recorded by the station, the duration value for the year 2020/2021 is not shown in Figures 62-64.

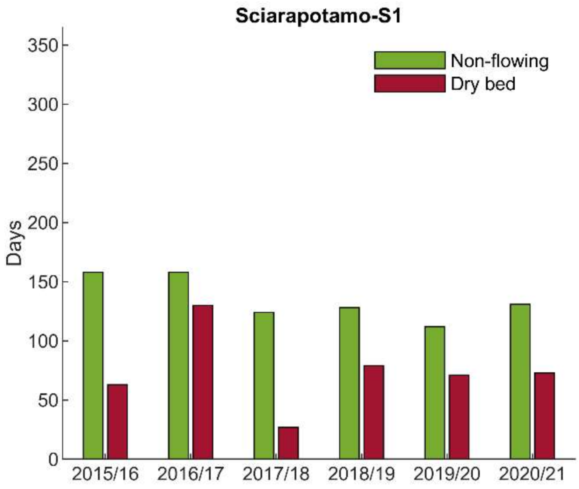

Figure 61: Number of days of non-flowing (green) and number of days of dry bed(red) extracted by RF for the S1 reach.

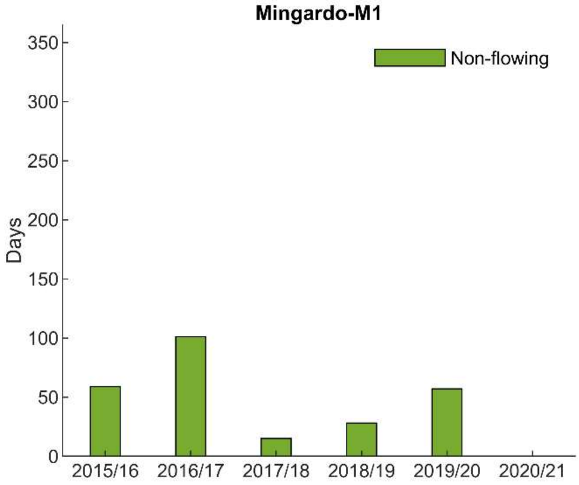

Figure 62: Number of days of non-flowing extracted by RF for the M1 reach.

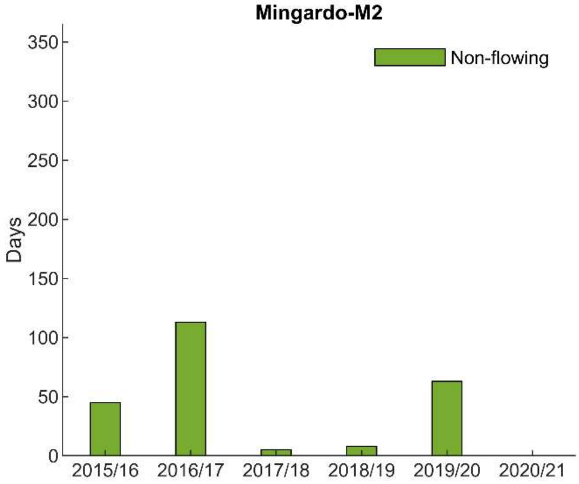

Figure 63: Number of days of non-flowing extracted by RF for the M2 reach.

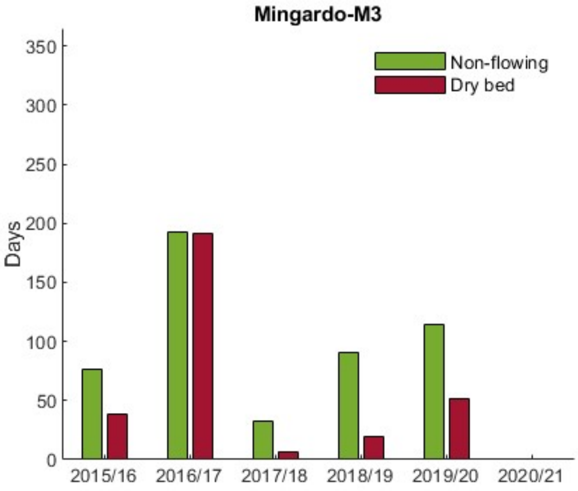

Figure 64: (a) Number of days of non-flowing (green) and number of days of dry bed(red) extracted by RF for the M3 reach.

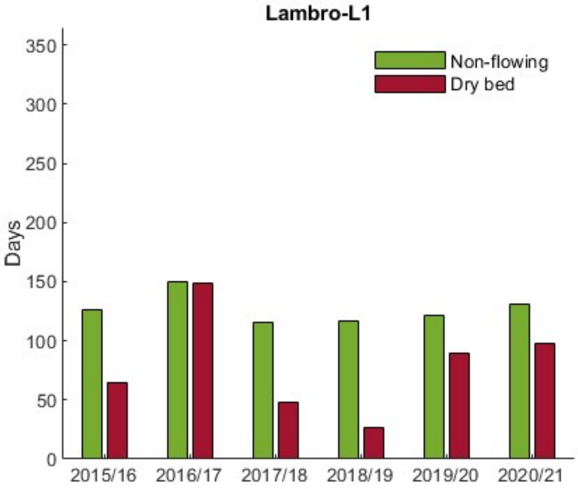

Figure 65: (a) Number of days of non-flowing (green) and number of days of dry bed(red) extracted by RF for the L1 reach.

In this analysis, the longest duration of the non-flowing or dry-bed condition was observed in the year 2016/2017 for all the reaches studied, while the shorter non-flowing duration was observed in the year 2017/2018 for the S1, M1, M2 and M3 reaches, and in the year 2018/2019 for the L1 reach. Comparing the duration values calculated from the prediction of the RF model and the duration values calculated from the mid interval method descripted in § 6.5.1, it can be observed that the trends are almost similar, and although in some cases the duration calculated from the mid interval method can overestimate or underestimate the duration of a given flow condition. In some circumstances, and especially when the number of images available is not low, it is possible to use the prediction obtained from the mid interval method for the calculation of the duration. Generally, given the typical climate of the Mediterranean regions, a limited number of images is more concentrated in the winter period than in the summer period. In the summer period, the number of images in the absence of cloud cover is higher than in the winter period, and therefore the error made in estimating the duration of the non-flowing condition is not significant.

The greatest differences between the duration values calculated by the two approaches are observed for the L1 reach. For the L1 reach, a non-conformity is observed between the trend obtained by the mid interval method (Figure 60) and that obtained from flow conditions estimated by the RF model (Figure 65). In the analysis obtained from the RF, the year with the shortest duration of dry bed period is 2018/2019, while in the analysis obtained from mid interval method, the year with the shortest duration is 2017/2018. Analyzing the cumulated rainfall values in the summer period (Table 19), it was seen that, for the L1 reach in the year 2018/2019, the cumulated rainfall value is higher than for the other years, while for other reaches the higher cumulated rainfall value occurs in the year 2017/2018.

Table 19:Cumulative summer Rainfall for the S1, M1, M2 ,M3 and L1 reaches

Years	Summer Rainfall [mm]			
	S1	M1	M2/M3	L1

2015/2016	286	305	304	325
2016/2017	228	237	215	137
2017/2018	**522**	**569**	**518**	371
2018/2019	435	463	461	**477**
2019/2020	384	353	346	328
2020/2021	257	227	224	229

The analysis conducted in this paragraph, which was also confirmed by the geolocated pictures reported in the previous paragraphs, showed that all the reaches analysed are non-perennial. The analysis conducted in this work is in contrast to what is provided in the River Basin Management Plan (RBMP) for the M1, M2, M3 and L1 reaches, which considers these reaches as perennial.

6.8 Comparison between the flow conditions and water levels

In this paragraph, a comparison between the classification obtained from the satellite images and the water level measurements will be presented for the M3 and L1 reaches. As already mentioned in § 6.1.4., the daily water levels are available only at two measuring stations, one about 500 m downstream of the L1 reach and another about 600 m downstream of the M3 reach. Figures 66 and 67 show the distribution of the water levels for the considered flow conditions (Flowing, ponding and dry bed) for the M3 and L1 reaches, using boxplots.

For the M3 reach of the Mingardo river (Figure 66), it is observed that, despite small regions of superposition, the water level measurements could be used to distinguish the flowing condition from the non-flowing one. While the ponding and dry bed conditions have similar water levels, and therefore the water levels cannot be used to distinguish the ponding condition from the dry bed condition.

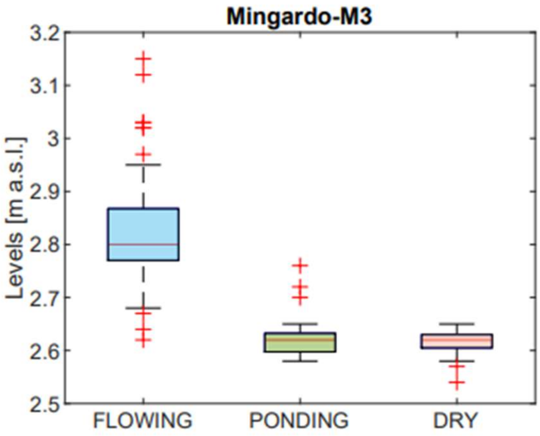

Figure 66:Distribution of water levels for considered flow conditions (Flowing, ponding and dry bed) for M3 reach.

For the L1 reach (Figure 67), on the other hand, the regions of superposition are present for all three flow conditions, and in this case, the water levels are not indicative of what happens along the L1 reach. Furthermore, in this case, compared to what is shown in Figure 66, it is observed that in the period in which the ponding and dry conditions occur, the hydrometer measured a wide range of water level values.

Knowledge of the water levels in a specific point of a river is not sufficient to describe the space-pattern of the presence/absence of water. In the presence of strong longitudinal variability in the flow regime, the measurement in one point cannot be representative of the entire watercourse. Moreover, non-perennial rivers are often characterized by long no-flow periods with the presence of water ponds. The information of a flow condition cannot be extrapolated from the point measurements.

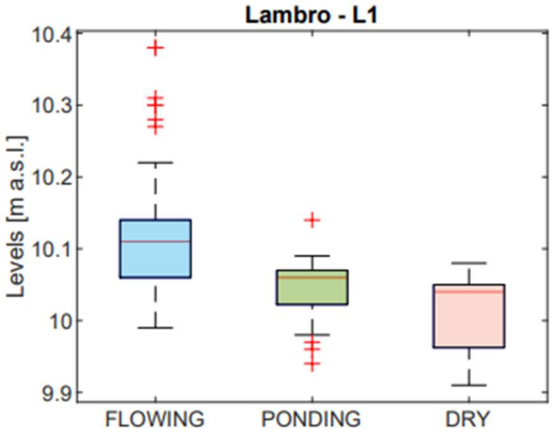

Figure 67: Distribution of water levels for considered flow conditions (Flowing, ponding and dry bed) for the L1 reach.

6.9 Monitoring Non-perennial rivers using Cosmo SkyMed data

To observe non-perennial rivers with higher spatial and temporal resolutions, the high spatial resolution Cosmo SkyMed SAR data (3 m) described in §2.1.4 were used. To this aim, a set of 18 descending Stripmap mode COSMO-SkyMed images was acquired for the year 2020.

The radar systems could lead to some important distortional effects, especially in mountainous regions, known as layover, foreshortening, and shadowing. These effects mainly depend on the relation between the terrain slope and the incident angle. The Layover effect, for example, is more severe at near range where the incidence angle is steeper. Given the orographic conformation of the study area, an angle of incidence (°26.56) as low as possible was chosen to avoid any layover effects. Despite the choice of a low angle of incidence, there were layover distortional effects all over the area, except for the M1 reach, and so the analysis with SAR data was only carried out for this reach.

In Figure 68, it is observed how the layover effect, which is white in the image, does not allow to see the river ed and water presence along the M3 reach. In the downstream part of M3 reach, the layover effect is lower, and the riverbed (grey colour) and presence of water (black colour) are clearly recognised. Unfortunately, in areas where there are high slopes, these distortional effects can occur. Considering that the geometric effects such as layover are linked to the orbit of the satellite and the sensor's line of sight, the selection of other orbits could avoid the occurrence of such geometric effects. However, with other orbits at other incidence angles, other geometric effects, like shadowing, may still occur.

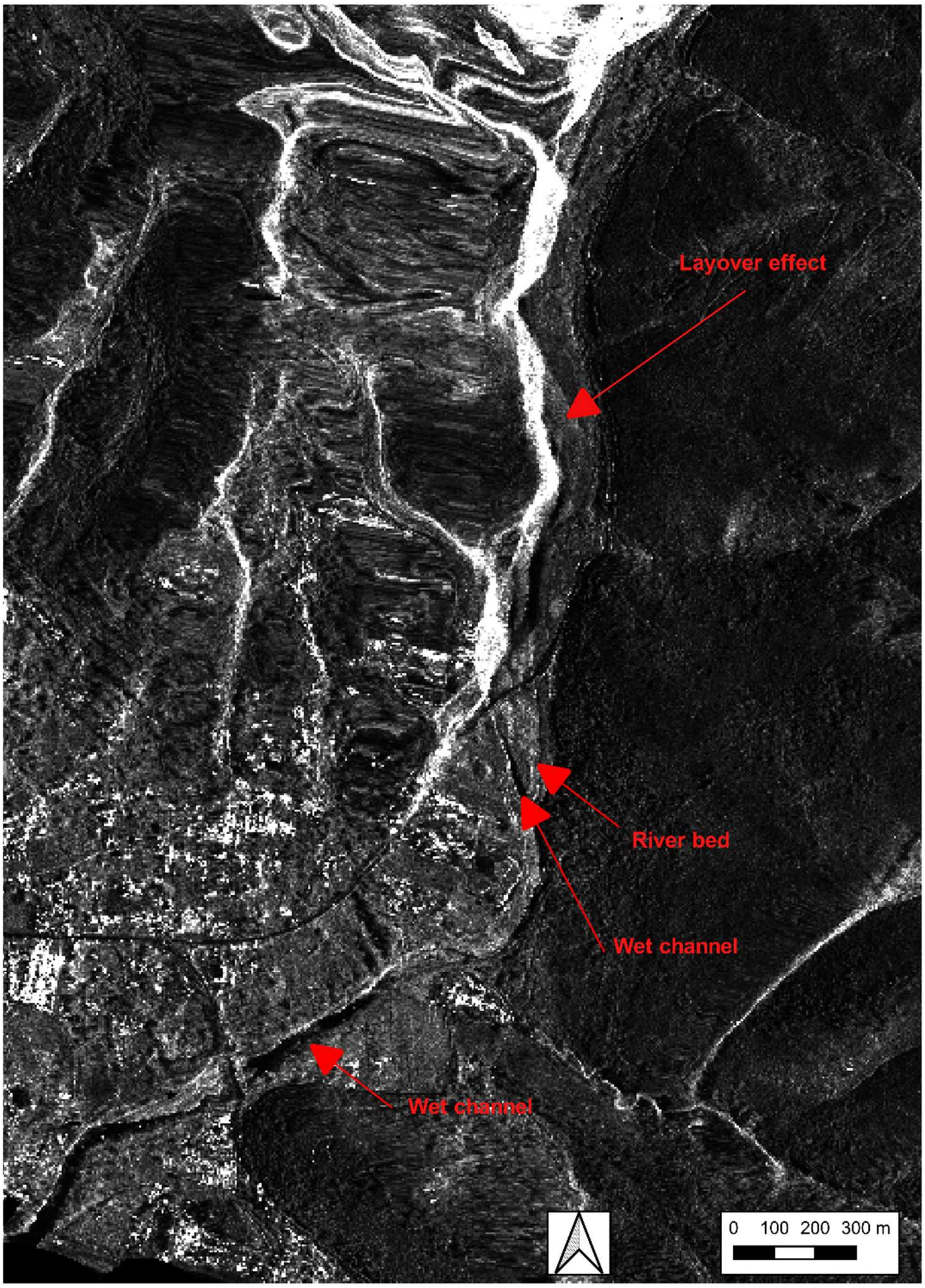

Figure 68: M3 reach, Cosmo SkyMed images of 17th January 2020, Layover effect.

The potential of Cosmo data has only been investigated along the M1 reach. To improve the visual interpretation and evaluate the effective possibility of observing the hydrological regime using SAR Cosmo SkyMed data, images acquired on different days were loaded on the red, green and blue bands in order to create a multi-temporal composite RGB. The use of RGB compositions helps to visualise time-series information as well as detect land cover changes.

In this case, the multi-temporal composite RGB were constructed as follows: in the Red channel (R) the image at the generic date was loaded, in the Green channel (G) the image with a flowing condition was loaded, and in the Blue channel (B) the image with a ponding condition was loaded. It is worth recalling that for the M1 reach only two flow conditions occur (Flowing and Ponding). In this combination, the colour black indicates that water is present in all three dates. Blue indicates that water is present in the image uploaded in the red channel. Purple indicates that there is no water in the image uploaded to the red channel.

Figures 69a and 70a show two examples of the multi-temporal RGB composite. Figure 69a was constructed in the following way: Red=18 February 2020, Green=17 January 2020, Blue=13 September 2020. The blue areas should be interpreted as regions covered by water only during the image of 18th February 2020. Figure 70a was constructed as follows: Red=28 August 2020, Green=17 January 2020, Blue=13 September 2020. In this case, the purple areas should be interpreted as regions covered by dry sediments in the image of 28th August 2020. The black colour indicates that the response is low in the three bands, pointing out the presence of persistent surface water. Based on this, the image of 18th February is representative of a flowing condition and the image of 28th August is representative of a ponding condition. Taking into account that the FCIs were validated by the comparisons reported in §6.6, Figures 69b and 70b show the FCIs extracted by Sentinel-2 acquisition of 20th February 2020 and 30th August 2020, close to the Cosmo SkyMed image acquisition dates, and Figures 69c/d (70c/d) show the FCIs extracted by Sentinel-2 acquisition of 13th January 2020 and 19th September 2020, close to the acquisition dates of the Cosmo SkyMed images uploaded to the green and blue channels.

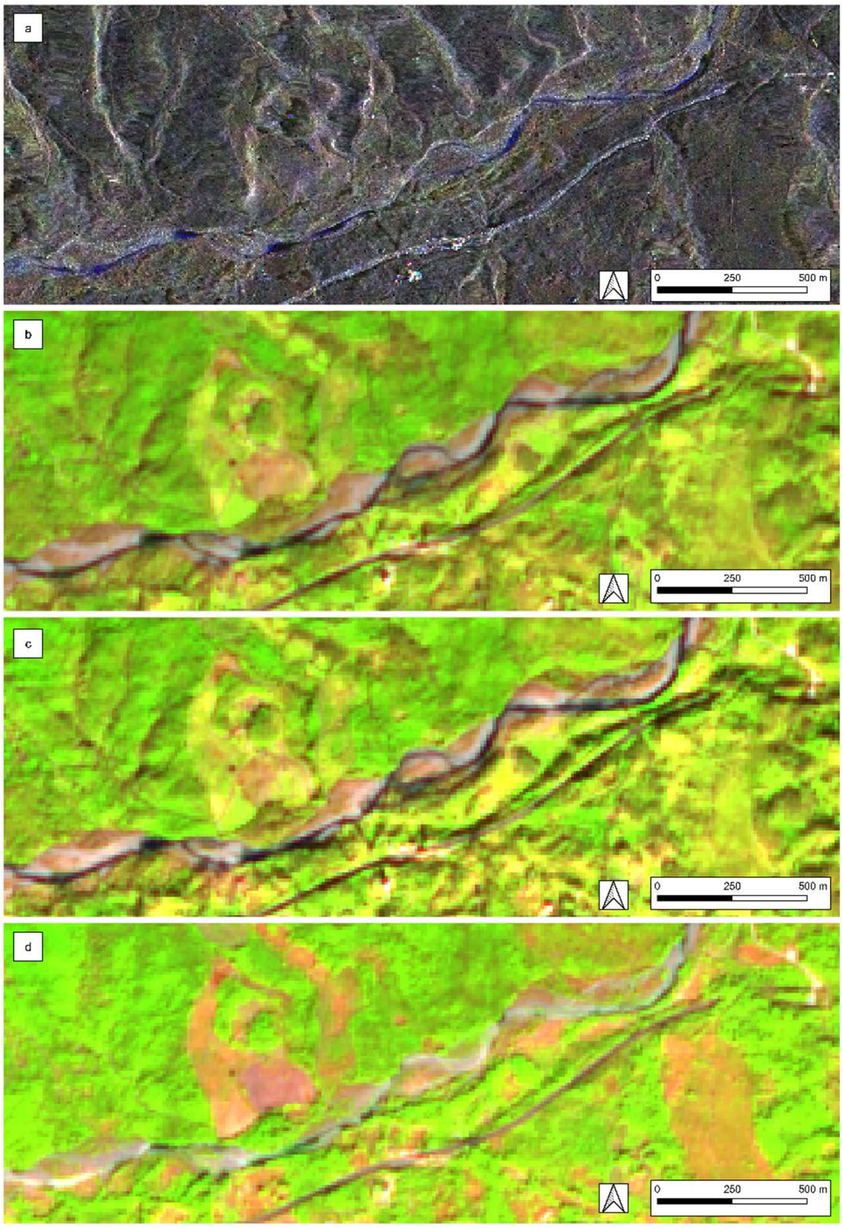

Figure 69: M1 reach, (a) Multi-temporal RGB composite with Cosmo SkyMed images (1st February 2020, 1st January 2020, 13th September 2020), (b) FCI extracted by Sentinel-2 acquisition of 20th February 2020, (c) FCI extracted by Sentinel-2 acquisition of the 13th January 2020, (d) FCI extracted by Sentinel-2 acquisition of 19th September 2020.

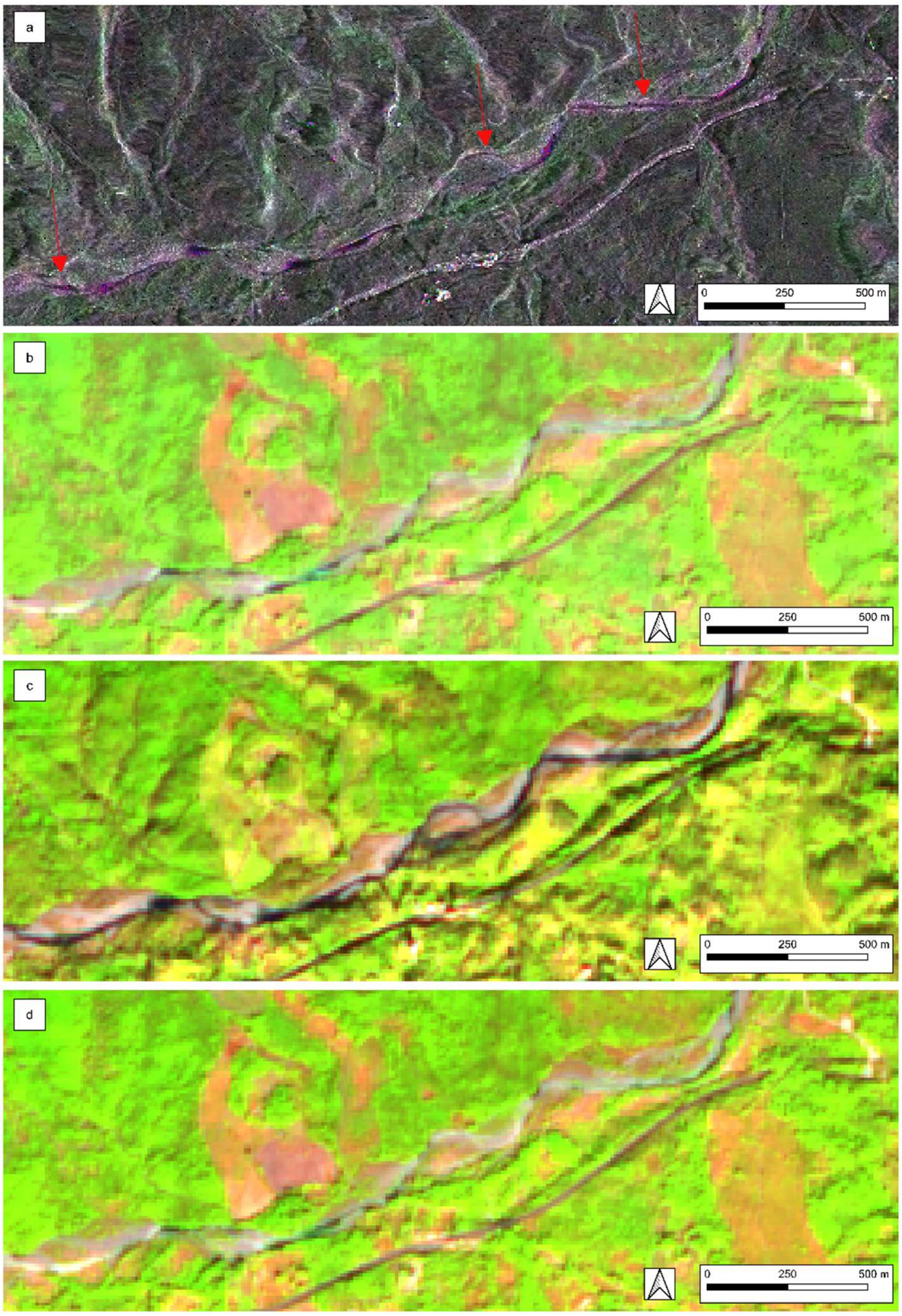

Figure 70: M1 reach (a) Multi-temporal RGB composite with Cosmo SkyMed images (28th August 2020, 17th January 2020, 13th September 2020), (b) FCI extracted by Sentinel-2 acquisition of 30th August 2020, (c) FCI extracted by Sentinel-2 acquisition of 13th January 2020, (d) FCI extracted by Sentinel-2 acquisition of 19th September 2020.

Figures 54 and 55 show that the Cosmo SkyMed SAR data provide partial information with respect to the multispectral data. As can be seen from Figure 54, the flowing condition is visible with greater clarity in the FCI image (54b) than in the RGB composite (54a); while in Figure 55a, in some areas (see red arrows), the RGB (55a) is able to recognize the presence of ponds that instead are not distinguishable in the FCI (55b).

Part of the information is lost in the process of georeferencing described in §2.2.4. It would be appropriate to use a DEM with a higher spatial resolution or at most equal to that of the satellite images, so as not to degrade the resolution. In addition, further investigations are needed to better understand how the Cosmo SkyMed SAR data can contribute to the analysis of the hydrological regime in non-perennial rivers. The simultaneous acquisition of the Sentinel-2 and Cosmo satellites, combined with a careful field survey, would allow to understand whether the combined use of the two datasets is able to provide more detailed information.

6.10 Discussion

Non-perennial rivers offer lotic, lentic and terrestrial habitats to various water-related organisms. A pond of water is one of the simplest freshwater environments but at the same time also extremely important for the development and growth of organisms; depending on the duration of the presence of water, it can offer a suitable habitat for various species, such as macroinvertebrate and plants. In addition, a dry riverbed, according to its degree of moisture, can offer a significant contribution to the maintenance of biodiversity.

Given their valuable ecological value, knowledge of the temporary hydrologic regime is very important for integrated river management and biodiversity conservation.

The main obstacle to the implementation of correct management and protection policies is constituted by the lack of information on the duration and frequency of zero-flow periods that are the primary determinants of river ecosystem processes.

Unfortunately, for this type of river system, there is very limited and little flow monitoring data. Given the scarcity of any direct measurements, many models have been proposed to simulate the hydrological regime. However, hydrological models, which are validated and calibrated on a range of data, may not take into account changes in climatic, land use and water withdrawals that may occur through time.

The spatio-temporal variations of the surface areas of ponds cannot be captured by traditional gauging systems. This issue has been demonstrated in the analysis conducted in §6.7, which showed that level measurements are not able to provide information on the flow conditions of a river reach.

Satellite data have the potential to extract more hydrological information that currently cannot be extracted using conventional gauging station records. Furthermore, the satellite data allow to continuously observe the variations in flow conditions over time, taking into account the effects induced by climate changes as well as all the variations that may occur along the reaches and in the underlying catchments.

The recent multispectral Sentinel-2 data with a spatial resolution of 10 m allow to reconstruct the effective hydrological regime along non-perennial rivers and to know the spatio-temporal variations of the surface areas of ponds.

The analysis of the spectral signatures conducted in §6.2 showed that for the water class, it is necessary to consider two spectral signatures since the reflectance of shallower water in NIR and SWIR is greater than in deeper water. It was also observed that sediments have a spectral response that varies with water content, and in particular the reflectance of sediments decreases with increasing water content.

The spectral signature shown in Figure 39 allowed to identify an optimal combination of the three bands, SWIR (B11), NIR (B8) and Red (B4), to obtain a better spectral separation among the water, sediments and vegetation classes.

Figures 37b and 37c show that the false colour combination (FCI, B11-B8-B4) allows to distinguish the presence or absence of water better than the true colour combination (RGB). This representation is necessary when the size of the wet channel is comparable to the pixel resolution, as in this combination, the water has a black or dark blue colour which makes it clearly distinguishable from the other classes. The qualitative comparisons shown in §6.3 proved that the FCI allows to distinguish the condition of continuous water flow (Flowing) from the one characterized by the presence of isolated ponds of water (Ponding) and the dry bed condition (Dry bed). The qualitative comparisons showed how the minimum width of a pond or wet channel that can be observed in the FCI is variable depending on how the object is contained within the pixel. It has been seen that it is possible to identify objects with a minimum width between 6 m and 15m. Consequently, the FCI is able to reliably identify objects with a width greater than 15m.

In this work, the term "ponds of water" is used to refer to the discontinuous presence of water along non-perennial rivers. This term, however, encompasses two flooding conditions: pools, understood as geomorphological units, characterised by water depth greater than average depths, and the presence of water characterized by lesser depths. From satellite images, it is complicated to distinguish between the two. Consideration could be given to the durations of water presence; whereby longer durations correspond to pools and shorter duration correspond to isolated ponds with shallower water conditions. Alternatively, one way of distinguishing between the two would be to combine satellite data with high-resolution DEM.

Future development of this work is in the direction of implementing an original code capable of automatically identifying the three flow conditions using binary water masks. Satellite data have not been fully explored for mapping the presence of water along non-perennial rivers. Seaton et al., (2021) explored the potential of *NDWI*, *MNDWI*, *NDVI*, Automated Water Extraction Index for shadowed (AWEIsh), non-shadowed regions (AWEInsh), and the Multi-Band Water Index (MBWI) to map and monitor pools along non perennial river using the Landsat-8 and Sentinel-2 datasets. To my knowledge, this is the only work in current literature that has used satellite data to map the presence of water along non-perennial rivers. The separability analysis described in §6.2 showed similar reflectance values in the various bands for water classes. For these study cases, it is impossible to use multispectral indices to identify the presence of water along river reaches. The reflectance values of vegetation classes (bushes and grass) show a marked difference between the visible and infrared bands and these classes can be identified by the *NDVI*. To distinguish water from sediment, two unsupervised automatic pixel-based classification methods were developed: SSMD and Threshold based method.

The qualitative comparison between the predicted land cover and FCI (Figure 49-50) shows good results. Both classification methods can recognise the presence of water, sediment and vegetation. However, the second method was found to be slightly less accurate in distinguishing between water and sediments compared to the first method.

Despite the good results, further improvements can be achieved. It would be useful to carry out new drone surveys at various times of the year to better understand the behaviour of water and sediments, as well as to obtain a more detailed separability analysis, which could provide the basis for the implementation of a new classification method. Furthermore, as suggested by Gilver et al., 2016 in the case of multispectral imagery, before implementing a classification algorithm, the problems of mixed pixels could be met using mixture modelling to estimate the proportion of each spectral 'end-member' present within a pixel (Mertes et al. 1993; Bryant 1996).

The FCI combination was extracted from 141 Sentinel-2 images, providing a classification of flow conditions on average every 15 days over the entire hydrological year, and on average every 10 days in the summer period. Based on this information, applying the average interval method, it was possible to estimate the durations of non-flowing and dry bed periods. The estimation of the durations can be further improved through the implementation of a Random Forest model (RF) able to predict the daily occurrence of a specific flow condition using as predictors spatially interpolated rainfall and air temperature data. Two binary classification RF models were developed to distinguish between non-flowing/flowing (NF/F) and the dry/ponding (D/P) events. The results indicated that the overall accuracy was very high for both binary models (ranging from 0.94 to 0.98 for NF/F and 0.82 to 0.92 for P/D). The true skill statistic (TSS) values performed better for the NF/F model than the D/P model, ranging from 0.82 to 0.92 and from 0.64 to 0.84 respectively.

The RF models were developed both at the local (individual reach, S1, M1, M2, M3 and L1) and globally scale (all the reaches together, G). The locally calibrated models were found to be slightly more accurate in predicting the correct flow condition compared to global models. Although the global model provides good results, it is preferable to use the local model, since the flow conditions depend on the characteristics of the underlying catchments and the reaches analysed. Among the predictive variables, it was observed that the cumulative 90-days rainfall (R90) resulted relevant in 90% of all the models.

The Random Forest model allows for the flow condition of a river reach to be predicted with good accuracy as a function of hydro-climatological variables.

Consequently, once the Random Forest model has been calibrated and validated in the period in which satellite images are available, it is possible to extend the analysis of the hydrological regime of rivers to the entire time series of precipitation and temperature.

The series of daily flow conditions were used to calculate the duration of non-flowing and dry bed periods, showing similar results to those obtained with the average interval method. This analysis showed that for the analysis period, and for all the reaches studied, there was a non-flowing period of varying duration depending on the year. The year with the longest period of non-flowing and dry bed was the year 2016/17, while the shortest period occurred in the years 2017/18 and 2018/19. Cosmo imagery can provide more information at more detailed spatial scales, and on longer time scales, as it has been available since 2007. In addition, the revisit time stated by ASI is equal to about 5 days although it may be higher in particular local contexts and at certain times, contributing to an increase in the revisit time. However, this aspect is not extremely important in this analysis, Sentinel-2 data already provide an excellent revisit time, especially in the summer period, which is the period of greatest interest in the analysis of the hydrological regime of temporary rivers in the Mediterranean region. The qualitative comparisons in Figures 69-70 show that despite the high spatial resolution of the Cosmo Sky Med SAR data, in the flowing condition, it provides less information than the FCI, while it seems to provide more information for the ponding condition (Figure 70). However, the contribution of the Cosmo SkyMed data is not fundamental in identifying the flowing condition, which is well identified in the FCI obtained from Sentinel-2 images, but in identifying ponds of dimensions smaller than those that can be recognized by the multispectral data. In the SAR data, the loss of information of the flowing condition may be due to the presence of possible ripples of the water surface or in the presence of geomorphic units such as riffles, cascades. The ponding condition, on the other hand, is a still water condition, which could be identified from high spatial resolution SAR data. Unfortunately, this analysis was not further investigated due to an absence of field surveys on the same days of acquisition of the SAR data. Field surveys are therefore necessary to understand if and to what extent the SAR data can provide a contribution to map and monitor ponds of water along non-perennial rivers.

7. Conclusions

This work explored the potential of multitemporal series of satellite data for the mapping and monitoring of freshwater environments. The potential of multispectral and Synthetic Aperture Radar (SAR) datasets distributed free of charge on the web or made available at no charge for research purposes, were analyzed. For the interpretation of the satellite images, very simple tools were developed that can be used by water authorities and decision-makers even if the professionals involved do not have experience in the processing and classification of satellite images. The simplicity of the methodologies and the gratuity of the data are the essential requirements to ensure a wide use of the proposed methodologies in applications related to the management of aquatic environments and the protection of the ecosystem services they provide.

Three different case studies were developed: a wetland, reaches of a perennial river of the main network and reaches of non-perennial rivers of the minor network.

Artificial wetlands play a key role in the strategies to limit the decline of freshwater biodiversity. The timing, duration and extension of periodical flooding are crucial for the survival of many freshwater species. For this reason, continuous monitoring is essential to optimize water resources and quantify habitat availability for water-related organisms. In the case study of the Albufera wetland, remote sensing Landsat-8 and Sentinel-2 multispectral images were exploited to monitor the winter evolution of flooding and land cover.

Three multispectral indices, *NDWI*, *MNDWI* and *NDVI*, were combined in an unsupervised, rule-based method for the automatic classification of four land cover classes: open water (*W*), mosaic of water, mud and vegetation (*M*), bare soil (*S*) and vegetated soil (*V*). A particularly relevant result for the applications is the possibility of distinguishing the *W* open water class form the *M* class, characterized by shallow water depths or by patches of water, mud and/or vegetation. The comparison with ground truth data, obtained through the integration of very high-resolution images and field survey, showed overall good agreement (overall accuracy equal to 0.985 for S2 and 0.965 for L8). The implemented method allowed to monitor the flooding dynamics of the wetland from 2013 to the 2020.

The flooding duration analyses showed that both the maximum extent of the flooding and its timing and duration were different from year to year. It was also observed that the overall presence of water (*M* plus *W* classes) last longer than the open water condition (*W* class). In particular, the *W* class is present in the highlands, on average, for less than 20 days, and the *Tancats* are in this class for between 60 and 80 days. The overall presence of water (*M* plus *W* land cover classes) lasted, on average, around 40 days in the highlands and for a period between roughly 90 and 110 days in the *Tancats*. Given the short duration of open water class, the duration of the time interval in which there are shallow waters or isolated pools (*M* class) is crucial for habitat availability.

Knowledge of the spatial distribution of submerged areas and their evolution over time is an essential element for the assessment of habitat availability for water related species.

Further developments of the study are in the direction of extending monitoring to the summer period, when water hidden under rice plants cannot be detected by multispectral sensors. In this case, the potential of L-band SAR data to monitor flooding dynamics under the vegetation could be investigated.

The case study of rivers has shown how satellite sensors have a great potential to monitor hydro-morphological variations at both the reach and the macro morphological units' scales. Landsat 4/5, Landsat-8 e Sentinel-2 images were used to map the wet channel of the two reaches of the Po River, to analyse its hydro-morphological changes from 1986 to 2020, as well as to monitor the effects of a river restoration work. A very simple classification method based on *MNDWI* was employed with extremely good results. The overall accuracy, obtained through multitemporal controls with very high-resolution images, was always greater than 0.90 for all the missions, showing that the classification accuracy remains consistent through time and space. To extend the analysis over an extended time interval and increasing the revisit time, it was necessary to integrate different datasets. The direct comparison of the wet channel, derived from Sentinel-2 and Landsat-8 acquisitions taken on the same days, showed a satisfying coherence (overall accuracy higher than 0.936). The multitemporal analysis confirmed that, during the last 35 years, the Po River between Boretto and Borgoforte has a more or less stable morphology. It was also demonstrated that the lowering of a wing dyke contributed to reactivating a secondary channel involving possible positive impacts on biodiversity.

For both the Albufera wetland and the Po River, it was observed that the *MNDWI* index estimates the presence of water more accurately than the *NDWI*. For the Albufera case study, not taking the *MNDWI* into consideration could lead to underestimating the presence of water and therefore the availability of habitat within the rice fields. In the study case of the Po River, on the other hand, the *MNDWI* is more stable over time than the *NDWI*, which on some dates does not allow the wet channel to be correctly classified.

For both case studies, the joint use of the two multispectral datasets provided an average revisit time of around 7 days. However, especially in rainy periods, the observation frequency may not be sufficient to capture the dynamics of the process intended to be observed. In these cases, SAR sensors can be useful as they can acquire information about the earth's surface under any light or weather conditions. For example, the Sentinel-1 mission acquires regularly every six days, ensuring observation even in cloudy conditions as is often the case during periods of peak flows and flooding.

On the other hand, SAR data are more complex to interpret and process than multispectral data.

Evaluating the potential of the Sentinel-1 data, the analysis showed how both polarimetric data (VV and VH) are useful in identifying the macro river units, sand bars and vegetated bars. A deep learning algorithm was implemented that, on some dates, is able to trace the wet channel with an accuracy almost comparable to that obtained with multispectral data, while on other dates, the results are somewhat less accurate.

The spatio-temporal variations of flows and ponds along non-perennial rivers have a notable influence on the ecosystems. The potential of Sentinel-2 images was explored to detect and monitor water surface changes along three non-perennial rivers during the period of operation of the mission, from 2015 to 2021. Automatic classification methods based on widespread used multispectral indices have proven to be useless in these contexts, due to the similar reflectance values of water in the different bands. The difficulty in identifying the presence of water is also due to the small width of the wet channels and ponds compared to the pixel size and the low separability of the water class from other classes.

From the study of the spectral response in the different bands, it was found that water has a characteristic spectral signature with very low intensities in correspondence with the Red, NIR, SWIR bands compared to the other components of the river corridors, and a false colour image (FCI), obtained from the composition of the SWIR, NIR and Red bands, which allows the presence of water to be more clearly distinguished.

The comparison with local surveys and very high-resolution images showed how the FCI allows to identify one of the three possible flow conditions: Flowing, Ponding and Dry bed, for all the reaches studied. In addition to the visual inspection of the FCI, two novel automatic classification methods were developed, with both providing good results. The codes for the processing of the Sentinel-2 data were made available on the Google Earth Engine platform to allow for a wide use by professionals and technicians of the basin authorities.

Further research developments will concern the implementation of a classification algorithm capable of automatically distinguishing the three flow conditions once the water masks are known.

The potential to exploit Cosmo SkyMed SAR higher spatial resolution data (3 m), with higher revisit times (about 5 days) and longer archives (available since 2007), was also investigated. Despite the higher spatial resolution, the detail of the information that can be extracted resulted to be not superior to that obtained with

Sentinel-2 especially in conditions of flowing. This is due to the high backscatter of the ripples of water surfaces. Given the higher ability to observe still water, the monitoring of the progressive decrease of the pools' size seems more promising.

The series of Sentinel-2 derived flow conditions were used for the calibration of binary Random Forest (RF) models capable of predicting non-flowing/flowing (NF/F) and dry/ponding (D/P) phases from precipitation and air temperature data. The RF models performed well in terms of accuracy (ranging from 84% to 98%) and true skill statistics (ranging from 0.67 to 0.95).

The proposed methodology for hydrological regime classification is therefore based on four steps: (i) identification of the flow conditions from Sentinel-2 images for the years 2015 to 2021. (ii) Calibration of the Random Forest model based on the dataset of known flow conditions (iii) application of the Random Forest model to the whole available historical series of temperature and precipitation and estimation of the hydrological regime.

The methodology can be used effectively to fill knowledge gaps about the regime of non-perennial streams. Its ease of use, free satellite source data and code, made available in the framework of the thesis, make it easily incorporated into assessment and management procedures such as the estimation of minimum ecological flow and the assessments of the river ecological status (Water Framework Directive 2000/60/EC).

References

Adam, E.; Mutanga, O.; Rugege, D. (2010). *Multispectral and hyperspectral remote sensing for identification and mapping of wetland vegetation:* A review. Wetl. Ecol. Manag. 18, 281–296.

AdBPo, (2008). Autorità di Bacino Fiume Po, Parma. Programma generale di gestione dei sedimenti alluvionali dell'alveo del fiume Po. In Italian.

Alexakis, D.D., Agapiou, A., Hadjimitsis, D.G., & Retalis, A. (2012). Optimizing statistical classification accuracy of satellite remotely sensed imagery for supporting fast flood hydrological analysis. *Acta Geophysica*, 60(3), 959-984.

Amani, M.; Salehi, B.; Mahdavi, S.; Brisco, B. (2018). *Spectral analysis of wetlands using multi-source optical satellite imagery.* ISPRS J. Photogramm. Remote Sens., 144, 119–136.

Aventino, K. (2021). *A global agenda for advancing freshwater biodiversity research.*

Ashraf, M., Shakir, A.S. (2018). Prediction of river bank erosion and protection works in a reach of Chenab River, Pakistan. Arabian Journal of Geosciences, 11(7), 1-11.

Baki, A. B. M., & Gan, T. Y., (2012). Riverbank migration and island dynamics of the braided Jamuna River of the Ganges–Brahmaputra basin using multi-temporal Landsat images. *Quaternary International*, *263*, 148-161.

Balcombe, C.K.; Anderson, J.T.; Fortney, R.H.; Kordek, W.S. (2005). *Aquatic macroinvertebrate assemblages in mitigated and natural wetlands*. Hydrobiologia , 541, 175–188.

Baumgartner, D.; Mörtl, M.; Rothhaupt, K.-O. (2008). *Effects of water-depth and water-level fluctuations on the macroinvertebrate community structure in the littoral zone of Lake Constance. I*n Ecological Effects of Water-Level Fluctuations in Lakes; Springer: Dordrecht, The Netherlands: pp. 97–107.

Bellio, M.; Kingsford, R.; Kotagama, S. (2009). *Natural versus artificial-wetlands and their waterbirds in Sri Lanka.* Biol. Conserv., 142, 3076–3085.

Billah, M. M. (2018). *Mapping and monitoring erosion-accretion in an alluvial river using satellite imagery–the river bank changes of the Padma river in Bangladesh.* Quaestiones Geographicae, 37(3), 87-95.

Bizzi, S., Demarchi, L., Grabowski, R.C., Weissteiner, C.J., Van de Bund, W.,(2016). *The use of remote sensing to characterise hydromorphological properties of European rivers*. Aquatic Sciences, 78(1), 57-70.

Boothroyd, R., Nones, M., Guerrero, M., (2021a). *Deriving planform morphology and vegetation coverage from remote sensing to support river management applications.* Frontiers in Environmental Science, 9, 657354.

Boothroyd, R.J., Williams, R.D., Hoey, T. B., Barrett, B., & Prasojo, O.A., (2021b). *Applications of Google Earth Engine in fluvial geomorphology for detecting river channel change*. Wiley Interdisciplinary Reviews: Water, 8(1), e21496.

Brierley, G. J., Fryirs, K. A., (2013). *Geomorphology and river management: applications of the river styles framework*. Eds. John Wiley & Sons.

Brisco, B. (2015). *Mapping and monitoring surface water and wetlands with synthetic aperture radar*. Remote Sensing of Wetlands: Applications and Advances, 119-136.

Buijse, A.D., Coops, H., Staras, M., Jans, L.H., Van Geest, G.J., Grift, R.E., ..., Roozen, F.C.,2002. *Restoration strategies for river floodplains along large lowland rivers in Europe*. Freshwater Biology, 47(4), 889-907.

Bujakowski, F., Falkowski, T., (2019). *Hydrogeological analysis supported by remote sensing methods as a tool for assessing the safety of embankments (case study from Vistula River Valley, Poland).* Water, 11(2), 266.

Burger, M.; Van Vuren, J.H.J.; De Wet, L.; Nel, A. (2018). *A comparison of water quality and macroinvertebrate community structure in endorheic depression wetlands and a salt pan in the Gauteng province, South Africa*. Environ. Monit. Assess. 2018, 191, 14.

Carbonneau, P. E., Belletti, B., Micotti, M., Lastoria, B., Casaioli, M., Mariani, S., ... & Bizzi, S. (2020). *UAV-based training for fully fuzzy classification of Sentinel-2 fluvial scenes.* Earth Surface Processes and Landforms, 45(13), 3120-3140.

Carbonneau, P., & Piégay, H. (Eds.). (2012). *Fluvial remote sensing for science and management*. John Wiley & Sons.

Carrasco, L.; O'Neil, A.W.; Morton, R.D.; Rowland, C.S. (2019). *Evaluating Combinations of Temporally Aggregated Sentinel-1, Sentinel-2 and Landsat 8 for Land Cover Mapping with Google Earth Engine*. Remote Sens.11, 288.

Casado, M.R., Gonzalez, R.B., Kriechbaumer, T., & Veal, A., (2015). *Automated identification of river hydromorphological features using UAV high resolution aerial imagery.* Sensors, 15(11),27969-27989.

Castellarin, A., Di Baldassarre, G., Brath, A. (2011). *Floodplain management strategies for flood attenuation in the river Po.* River Res. Applic., 27, 1037-1047.

Castiglioni, G.B., Biancotti, A., Bondesan, M., Cortemiglia, G.C., Elmi, C., Favero, V., Gasperi, G., Marchetti, G., Orombelli, G., Pellegrini, G.B., Tellini, C., (1999). *Geomorphological map of the Po Plain, Italy, at a scale of 1: 250 000*. Earth Surface Processes and Landforms, 24(12), 1115–1120.

Cavallo, C., Papa, M. N., Gargiulo, M., Palau-Salvador, G., Vezza, P., & Ruello, G. (2021). *Continuous Monitoring of the Flooding Dynamics in the Albufera Wetland (Spain) by Landsat-8 and Sentinel-2 Datasets.* Remote Sensing, 13(17), 3525.

Cavallo, C., Nones, M., Papa, M. N., Gargiulo, M., & Ruello, G. (2021). *Monitoring the morphological evolution of a reach of the Italian Po River using multispectral satellite imagery and stage data*. Geocarto International, 1-23.

Church, M. (1996). *Space, time and the mountain–how do we order what we see.* The scientific nature of geomorphology, 147-170.

Curran, A., De Bruijn, K., Domeneghetti, A., Bianchi, F., Kok, M., Vorogushyn, S., Castellarin, A., 2020. *Large-scale stochastic flood hazard analysis applied to the Po River.* Natural Hazards, 104(3), 2027-2049.

Curran, P.J. (1983). *Multispectral remote sensing for the estimation of green leaf area index. In Philosophical Transactions of the Royal Society of London*. Series A, Mathematical and Physical Sciences; Royal Society: London, UK, Volume 309, pp. 257–270.

Datry, Thibault, et al. (2017)."*Science and management of intermittent rivers and ephemeral streams* (SMIRES).

Davranche, A.; Poulin, B.; Lefebvre, G. (2013). *Mapping flooding regimes in Camargue wetlands using seasonal multispectral data.* Remote Sens. Environ., 138, 165–171.

De Grandi, G.F., Leysen, M., Lee, J.S., Schuler, D., (1997). *Radar reflectivity estimation using multiple SAR scenes of the same target: Technique and applications.* In: International Geoscience and Remote Sensing Symposium (IGARSS). pp. 1047–1050

Dewan, A., Corner, R., Saleem, A., Rahman, M. M., Haider, M. R., Rahman, M. M., & Sarker, M. H. (2017). *Assessing channel changes of the Ganges-Padma River system in Bangladesh using Landsat and hydrological data*. Geomorphology, 276, 257-279.

Dona, C.; Chang, N.-B.; Caselles, V.; Sánchez, J.M.; (2015). Camacho, A.; Delegido, J.; Vannah, B.W. Integrated satellite data fusion and mining for monitoring lake water quality status of the Albufera de Valencia in Spain. J. Environ. Manag., 151, 416–426.

Downing, J. A., Cole, J. J., Duarte, C. M., Middelburg, J. J., Melack, J. M., Prairie, Y. T., ... & Tranvik, L. J. (2012). Global abundance and size distribution of streams and rivers. Inland waters, 2(4), 229-236.

Elphick, C.S. (2000). *Functional Equivalency between Rice Fields and Seminatural Wetland Habitats*. Conserv. Biol. 14, 181–191.

Filipponi, F. (2019). *Sentinel-1 GRD preprocessing workflow.* In Multidisciplinary digital publishing institute proceedings (Vol. 18, No. 1, p. 11).

Gallant, A. L. (2015). *The challenges of remote monitoring of wetlands*. Remote Sensing, 7(8), 10938-10950.

Gelautz, M., Frick, H., Raggam, J., Burgstaller, J., & Leberl, F. (1998). *SAR image simulation and analysis of alpine terrain. ISPRS Journal of Photogrammetry and Remote Sensing*, 53(1), 17-38.

Gezie, A.; Anteneh, W.; Dejen, E.; Mereta, S.T. (2017) *Effects of human-induced environmental changes on benthic macroinvertebrate assemblages of wetlands in Lake Tana Watershed, Northwest Ethiopia*. Environ. Monit. Assess., 189, 152.

Gorelick, N., Hancher, M., Dixon, M., Ilyushchenko, S., Thau, D., & Moore, R. (2017). *Google Earth Engine: Planetary-scale geospatial analysis for everyone*. Remote sensing of Environment, 202, 18-27.

Grizzetti, B., Pistocchi, A., Liquete, C., Udias, A., Bouraoui, F., & Van De Bund, W. (2017). *Human pressures and ecological status of European rivers.* Scientific reports, 7(1), 1-11.

Guo, M.; Li, J.; Sheng, C.; Xu, J.; Wu, L. (2017). *A Review of Wetland Remote Sensing*. Sensors, 17, 777.

Dewan, A., Corner, R., Saleem, A., Rahman, M. M., Haider, M. R., Rahman, M. M., & Sarker, M. H., 2017. *Assessing channel changes of the Ganges-Padma River system in Bangladesh using Landsat and hydrological data*. Geomorphology, 276, 257-279.

Díaz, S., Settele, J., Brondízio, E.S., Ngo, H.T., Guèze, M., Agard, J., Arneth, A., Balvanera, P., Brauman, K.A., Butchart, S.H.M., Chan, K.M.A., Garibaldi, L.A., Ichii, K., Liu, J., Subramanian, S.M., Midgley, G.F., Miloslavich, P., Molnár, Z., Obura, D., Pfaff, A., Polasky, S., Purvis, A., Razzaque, J., Reyers, B., Roy Chowdhury, R., Shin, Y.J., Visseren-Hamakers, I.J., Willis, K.J. & Zayas, C.N., Eds.). Bonn, Germany: Secretariat of the Intergovernmental Platform for Biodiversity and Ecosystem Services. IPBES. (2019). *Summary for policymakers of the global assessment report of the intergovernmental science-policy platform on biodiversity and ecosystem services*

Djamai, N.; Fernandes, R.; Weiss, M.; McNairn, H.; Goïta, K. (2019). Validation of the Sentinel Simplified Level 2 Product Prototype Processor (SL2P) for mapping cropland biophysical variables using Sentinel-2/MSI and Landsat-8/OLI data. Remote Sens. Environ., 225, 416–430.

Dechka, J.A.; Franklin, S.E.; Watmough, M.D.; Bennett, R.P.; Ingstrup, D.W. (2002). *Classification of wetland habitat and vegetation communities using multi-temporal Ikonos imagery in southern Saskatchewan. Can.* J. Remote Sens., 28, 679–685.

Domeneghetti, A., Carisi, F., Castellarin, A., Brath, A., 2015. *Evolution of flood risk over large areas: Quantitative assessment for the Po River*. Journal of Hydrology,527, 809–823.

Dronova, I.; Gong, P.; Wang, L. (2011). *Object-based analysis and change detection of major wetland cover types and their classification uncertainty during the low water period at Poyang Lake, China*. Remote Sens. Environ., 115, 3220–3236.

Drusch, M., Del Bello, U., Carlier, S., Colin, O., Fernandez, V., Gascon, F., ... & Bargellini, P., (2012). *Sentinel-2: ESA's optical high-resolution mission for GMES operational services*. Remote sensing of Environment, 120, 25-36.

England, J., Skinner, K.S., Carter, M.G. (2008). *Monitoring, river restoration and the Water Framework Directive.* Water and Environment Journal, 22(4), 227-234.

European Commission, 2000. Directive 2000/60/EC of the European Parliament and of the Council of 23 October 2000 establishing a framework for Community action in the field of water policy. Off. J. Eur. Communities, L327, 1-7

Forkuor, G.; Hounkpatin, O.K.L.; Welp, G.; Thiel, M. (2017). *High Resolution Mapping of Soil Properties Using Remote Sensing Variables in South-Western Burkina Faso: A Comparison of Machine Learning and Multiple Linear Regression Models*. PLoS ONE, 12, e0170478.

Garcia, X. F., Schnauder, I., & Pusch, M. T., 2012. Complex hydromorphology of meanders can support benthic invertebrate diversity in rivers. Hydrobiologia, 685(1), 49-68.

Gilvear, D.J., & Bryant, R., (2016). *Analysis of remotely sensed data for fluvial geomorphology and river science*. In M. Kondolf & H. Piégay (Eds.), Tools in fluvial geomorphology (pp. 103–132). Chichester, England: John Wiley & Sons.

Gilvear, D. J., Davids, C., & Tyler, A. N., (2004). *The use of remotely sensed data to detect channel hydromorphology; River Tummel, Scotland*. River Research and Applications, 20(7), 795-811.

Guerrero, M., Di Federico, V., Lamberti, A.,2013. *Calibration of a 2-D morphodynamic model using water-sediment flux maps derived from an ADCP recording.* Journal of Hydroinformatics, 15(3), 813-828.

Gurnell, A. M., del Tánago, M. G., Rinaldi, M., Grabowski, R., Henshaw, A., O'Hare, M., ... & Buijse, A. D., (2015). *Development and application of a multi-scale process-based framework for the hydromorphological assessment of European rivers.* In Engineering Geology for Society and Territory, 3, 339-342, Springer, Cham.

Halabisky, M., Moskal, L. M., Gillespie, A., & Hannam, M. (2016). *Reconstructing semi-arid wetland surface water dynamics through spectral mixture analysis of a time series of Landsat satellite images (1984–2011).* Remote sensing of environment, 177, 171-183.

Henshaw, A. J., Gurnell, A. M., Bertoldi, W., & Drake, N. A. (2013). *An assessment of the degree to which Landsat TM data can support the assessment of fluvial dynamics, as revealed by changes in vegetation extent and channel position, along a large river*. Geomorphology, 202, 74-85.

Henshaw, A. J., Sekarsari, P. W., Zolezzi, G., & Gurnell, A. M. (2020*). Google Earth as a data source for investigating river forms and processes: Discriminating river types using form-based process indicators.* Earth Surface Processes and Landforms, 45(2), 331-344.

Holben, B.N. (1986). Characteristics of maximum-value composite images from temporal AVHRR data. Int. J. Remote Sens., 7, 1417–1434.

Inglada, J.; Arias, M.; Tardy, B.; Hagolle, O.; Valero, S.; Morin, D.; Dedieu, G.; Sepulcre, G.; Bontemps, S.; Defourny, P.; et al. (2015). *Assessment of an Operational System for Crop Type Map Production Using High Temporal and Spatial Resolution Satellite Optical Imagery*. Remote Sens. 7, 12356–12379.

Jarchow, C. J., Didan, K., Barreto-Muñoz, A., Nagler, P. L., & Glenn, E. P., (2018). *Application and comparison of the MODIS-derived enhanced vegetation index to VIIRS, landsat 5 TM and landsat 8 OLI platforms: A case study in the arid Colorado river delta, Mexico*. *Sensors*, 18(5), 1546.

Jensen, J. R. (2009). *Remote sensing of the environment: An earth resource perspective 2/e*. Pearson Education India.

Jiang, H., Feng, M., Zhu, Y., Lu, N., Huang, J., & Xiao, T., (2014). *An automated method for extracting rivers and lakes from Landsat imagery.* Remote Sensing, 6(6), 5067-5089.

Kaplan, G., & Avdan, U. (2017). Mapping and monitoring wetlands using Sentinel-2 satellite imagery.

Kim, D.-K.; Jo, H.; Park, K.; Kwak, I.-S. (2019). *Assessing Spatial Distribution of Benthic Macroinvertebrate Communities Associated with Surrounding Land Cover and Water Quality*. Appl. Sci., 9, 5162.

Kryniecka, K., & Magnuszewski, A., (2021). *Application of Satellite Sentinel-2 Images to Study Alternate Sandbars Movement at Lower Vistula River (Poland).* Remote Sensing, 13(8), 1505.

Lanzoni, S., Luchi, R., Bolla Pittaluga, M. (2015). *Modeling the morphodynamic equilibrium of an intermediate reach of the Po River (Italy).* Advances in Water Resources 2015, 81, 92-102.

Lamberti, A., Schippa, L. (1994). Studio dell'abbassamento del fiume Po: Previsioni trentennali di abbassamento a Cremona. Supplemento a Navigazione Interna, rassegna trimestrale di studi e informazioni 1994, 3/4. Eds. Azienda Regionale per i porti di Cremona e Mantova, Cremona, Italy. in Italian

Latrubesse, E. M. (2015). *Large rivers, megafans and other Quaternary avulsive fluvial systems: A potential "who's who" in the geological record.* Earth-Science Reviews, 146, 1-30.

Lawler, S.P. (2001). *Rice Fields as Temporary Wetlands: A Review*. Isr. J. Zool. 47, 513–528.

Legleiter, C. J., & Fonstad, M. A., (2012). *An introduction to the physical basis for deriving river information by optical remote sensing*. Fluvial remote sensing for science and management, 43-69.

Leopold, L.B., (1994). A View of the River. Harvard University Press.

Li, W.; Du, Z.; Ling, F.; Zhou, D.; Wang, H.; Gui, Y.; Sun, B.; Zhang, X. A (2013). Comparison of Land Surface Water Mapping Using the Normalized Difference Water Index from TM, ETM+ and ALI. Remote Sens. 5, 5530–5549.

Li, L.; Vrieling, A.; Skidmore, A.; Wang, T.; Muñoz, A.-R.; Turak, E. (2015). Evaluation of MODIS Spectral Indices for Monitoring Hydrological Dynamics of a Small, Seasonally-Flooded Wetland in Southern Spain. Wetlands, 35, 851–864.

Longobardi, A., Boulariah, O., & Villani, P. (2021). *Assessment of centennial (1918–2019) drought features in the Campania region by historical in situ measurements (southern Italy).* Natural Hazards and Earth System Sciences, 21(7), 2181-2196.

Lopez-Garcia, M.J.; Caselles, V. (1987). *Use of Thematic Mapper data to assess water quality in Albufera Lagoon of Valencia (Spain).* In Proceedings of the 13th Annual Conference of the Remote Sensing Society, Nottingham, UK, 7–11 September; pp. 510–519.

Loveland, T. R., & Irons, J. R., (2016). *Landsat 8: The plans, the reality, and the legacy.* Remote Sensing of Environment, 185, 1-6.

Ma, S.; Zhou, Y.; Gowda, P.H.; Dong, J.; Zhang, G.; Kakani, V.G.; Wagle, P.; Chen, L.; Flynn, K.C.; Jiang, W. (2019). *Application of the water-related spectral reflectance indices: A review*. Ecol. Indic., 98, 68–79.

Ma, Z.; Li, B.; Zhao, B.; Jing, K.; Tang, S.; Chen, J. (2004). *Are artificial wetlands good alternatives to natural wetlands for waterbirds? A case study on Chongming Island, China*. Biodivers. Conserv. 13, 333–350.

Machado, I.; Maltchik, L. (2009). *Can management practices in rice fields contribute to amphibian conservation in southern Brazilian wetlands?* Aquat. Conserv. Mar. Freshw. Ecosyst.20, 39–46.

Mahdavi, S., Salehi, B., Granger, J., Amani, M., Brisco, B., & Huang, W. (2018). *Remote sensing for wetland classification: A comprehensive review*. GIScience & Remote Sensing, 55(5), 623-658.

Malinowski, R.; Groom, G.; Schwanghart, W.; Heckrath, G. (2015*). Detection and Delineation of Localized Flooding from WorldView-2 Multispectral Data*. Remote Sens., 7, 14853–14875.

Mandanici, E.; Bitelli, G. (2016). *Preliminary Comparison of Sentinel-2 and Landsat 8 Imagery for a Combined Use*. Remote Sens., 8, 1014.

Marchetti, M., (2002). *Environmental changes in the central Po Plain (northern Italy) due to fluvial modifications and anthropogenic activities.* Geomorphology, 44(3-4), 361-373.

Marcus, WA, & Fontad, MA., (2010). *Telerilevamento dei fiumi: l'emergere di una sottodisciplina nelle scienze fluviali.* Processi e morfologie della superficie terrestre, 35 (15), 1867-1872.

Marcus WA, Legleiter CJ, Aspinall RJ et al., (2003). *High spatial resolution hyper spectral mapping of in-stream habitats, depths, and woody debris in mountain streams*. Geomorphology, 55:363–380

Martinez, J. M., & Le Toan, T. (2007). *Mapping of flood dynamics and spatial distribution of vegetation in the Amazon floodplain using multitemporal SAR data*. Remote sensing of Environment, 108(3), 209-223.

Maselli, V., Normandeau, A., Nones, M., Tesi, T., Langone, L., Trincardi, F., Bohacs, K.M., 2020. *Tidal modulation of river-flood deposits: How low can you go?*. Geology, 48(7), 663–667.

Maselli, V., Pellegrini, C., Del Bianco, F., Mercorella, A., Nones, M.,Crose, L., Guerrero, M., Nittrouer, J.A.,2018. *River Morphodynamic Evolution Under Dam-Induced Backwater: An Example from the Po River (Italy)*. Journal of Sedimentary Research, 88 (10), 1190–1204.

Matthews, G.V.T. (1993). The *Ramsar Convention on Wetlands: Its History and Development*; Ramsar Convention Bureau: Gland, Switzerland.

McFeeters, S.K. (1996). *The use of the Normalized Difference Water Index (NDWI) in the delineation of open water features*. Int. J. Remote Sens., 17, 1425–1432.

Messager, M. L., Lehner, B., Cockburn, C., Lamouroux, N., Pella, H., Snelder, T., ... & Datry, T. (2021). *Global prevalence of non-perennial rivers and streams. Nature,* 594(7863), 391-397.

Montanari, A., (2012). *Hydrology of the Po River: Looking for changing patterns in river discharge.* Hydrology and Earth System Sciences, 16(10), 3739-3747.

Munyati, C. (2000). *Wetland change detection on the Kafue Flats, Zambia, by classification of a multitemporal remote sensing image dataset.* Int. J. Remote Sens., 21, 1787–1806.

Nones, M., (2021). *Remote sensing and GIS techniques to monitor morphological changes along the middle-lower Vistula River, Poland*. Int. Journal of River Basin Management, 19 (3), 345-357.

Nones, M., (2016). *River restoration: The need for a better monitoring agenda. In Proceedings of the 13th International Symposium on River Sedimentatio*n, Stuttgart, Germany, 19-22.

Nones, M., & Di Silvio, G., (2016). *Modeling of river width variations based on hydrological, morphological, and biological dynamics.* Journal of Hydraulic Engineering, 142(7), 04016012.

Nones, M., Gerstgraser, C., & Wharton, G., (2017). *Consideration of hydromorphology and sediment in the implementation of the EU water framework and floods directives: a comparative analysis of selected EU member states.* Water and Environment Journal 2017, 31(3), 324-329.

Ozesmi, S.L.; Bauer, M.E. (2002). Satellite remote sensing of wetlands. Wetl. Ecol. Manag., 10, 381–402.

Pahlevan, N., Chittimalli, S. K., Balasubramanian, S. V., & Vellucci, V., (2019). *Sentinel-2/Landsat-8 product consistency and implications for monitoring aquatic systems*. Remote sensing of Environment, 220, 19-29.

Paillex, A., Dolédec, S.,Castella, E., Mérigoux, S., (2009). *Large river floodplain restoration: predicting species richness and trait responses to the restoration of hydrological connectivity.* Journal of Applied Ecology, 46(1), 250-258.

Palamuleni, L. G., Annegarn, H. J., & Landmann, T., (2010). *Land cover mapping in the Upper Shire River catchment in Malawi using Landsat satellite data.* Geocarto International, 25(7), 503-523.

Perennou, C.; Beltrame, C.; Guelmami, A.; Vives, P.T.; Caessteker, P. (2012). *Existing areas and past changes of wetland extent in the Mediterranean region: An overview*. Ecol. Mediterr.38, 53–66.

Pernollet, C.A.; Guelmami, A.; Green, A.J.; Masip, A.C.; Dies, B.; Bogliani, G.; Tesio, F.; Brogi, A.; Gauthier-Clerc, M.; Guillemain, M. (2015). *A comparison of wintering duck numbers among European rice production areas with contrasting flooding regimes*. Biol. Conserv. 186, 214–224.

Pires, M.M.; Kotzian, C.B.; Spies, M.R.; Baptista, V.D.A. (2016). *Comparative assessment of aquatic macroinvertebrate diversity in irrigated rice fields and wetlands through different spatial scales: An additive partitioning approach.* Mar. Freshw. Res. 67, 368–379.

Preston, T.M.; Borgreen, M.J.; Ray, A.M. (2018). *Effects of brine contamination from energy development on wetland macroinvertebrate community structure in the Prairie Pothole Region*. Environ. Pollut. 239, 722–732.

Rahman, M. R., & Thakur, P. K. (2018). *Detecting, mapping and analysing of flood water propagation using synthetic aperture radar (SAR) satellite data and GIS: A case study from the Kendrapara District of Orissa State of India.* The Egyptian Journal of Remote Sensing and Space Science, 21, S37-S41.

Rashid, M.B., Habib, M.A., Khan, R., & Islam, A.R.M.T. (2021). *Land transform and its consequences due to the route change of the Brahmaputra River in Bangladesh.* International Journal of River Basin Management, in press, 1-38.

Rebelo, L.-M.; Finlayson, C.; Nagabhatla, N. (2009). Remote sensing and GIS for wetland inventory, mapping and change analysis. J. Environ. Manag., 90, 2144–2153.

Revenga, C.; Brunner, J.; Henninger, N.; Kassem, K.; Payne, R. (2000). *Freshwater Systems*; World Resources Institute: Washington DC, USA.

SAR Basics with the Sentinel-1 Toolbox in SNAP Tutorial. Available online: http://step.esa.int/main/doc/tutorials/ (accessed on 22 May 2017).

Rinaldi, M., Belletti, B., Bussettini, M., Comiti, F., Golfieri, B., Lastoria, B., ... & Surian, N., (2017). *New tools for the hydromorphological assessment and monitoring of European streams*. Journal of Environmental Management, 202, 363-378.

Rutkay, A.T.U.N.; Kalkan, K.; Gürsoy, Ö. (2020). *Determining the forest fire risk with sentinel 2 images*. Turk. J. Geosci., 1, 22–26.

Schad, A.N.; Kennedy, J.H.; Dick, G.O.; Dodd, L. (2020). *Aquatic macroinvertebrate richness and diversity associated with native submerged aquatic vegetation plantings increases in longer-managed and wetland-channeled effluent constructed urban wetlands*. Wetl. Ecol. Manag. 28, 461–477.

Schropp, M.H.I., (1995). *Principles of designing secondary channels along the River Rhine for the benefit of ecological restoration.* Water Science and Technology, 31(8), 379-382.

Seaton, D., Dube, T., & Mazvimavi, D., (2020). *Use of multi-temporal satellite data for monitoring pool surface areas occurring in non-perennial rivers in semi-arid environments of the Western Cape, South Africa.* ISPRS Journal of Photogrammetry and Remote Sensing, 167, 375-384.

Sinha, R., & Ghosh, S., (2012). *Understanding dynamics of large rivers aided by satellite remote sensing: a case study from Lower Ganga plains, India*. Geocarto International, 27(3), 207-219.

Skoulikidis, N. T., Sabater, S., Datry, T., Morais, M. M., Buffagni, A., Dörflinger, G., ... & Tockner, K. (2017). *Non-perennial Mediterranean rivers in Europe: status, pressures, and challenges for research and management.* Science of the Total Environment, 577, 1-18.

Shanafield, M., Bourke, S. A., Zimmer, M. A., & Costigan, K. H. (2021*). An overview of the hydrology of non-perennial rivers and streams.* Wiley Interdisciplinary Reviews: Water, 8(2), e1504.

Soria, J.; Vera-Herrera, L.; Calvo, S.; Romo, S.; Vicente, E.; Sahuquillo, M.; Sòria-Perpinyà, X. (2021). *Residence Time Analysis in the Albufera of Valencia, a Mediterranean Coastal Lagoon, Spain*. Hydrology, 8, 37.

Sòria-Perpinyà, X.; Vicente, E.; Urrego, P.; Pereira-Sandoval, M.; Ruíz-Verdú, A.; Delegido, J.; Soria, J.; Moreno, J. (2020). *Remote sensing of cyanobacterial blooms in a hypertrophic lagoon (Albufera of València, Eastern Iberian Peninsula) using multitemporal Sentinel-2 images*. Sci. Total Environ., 698, 134305.

Stenert, C.; Bacca, R.C.; Maltchik, L.; Rocha, O. (2009). *Can hydrologic management practices of rice fields contribute to macroinvertebrate conservation in southern Brazil wetlands?* Hydrobiologia, 635, 339–350.

Story, M.; Congalton, R.G. (1986). *Accuracy assessment: A user's perspective. Photogramm*. Eng. Remote Sens., 52, 397–399.

Strozzi, T., Wiesmann, A., Kääb, A., Joshi, S., & Mool, P. (2012). *Glacial lake mapping with very high-resolution satellite SAR data.* Natural Hazards and Earth System Sciences, 12(8), 2487-2498.

Surian, N., & Rinaldi, M., 2003. *Morphological response to river engineering and management in alluvial channels in Italy*. Geomorphology, 50(4), 307-326.

Tajiri, H.; Ohkawara, K. (2013). *The Effects of Flooding and Plowing on Foraging Site Selection by Wintering Dabbling Ducks in Rice Fields*. Ornithol. Sci., 12, 127–136.

Tapete, D., & Cigna, F. (2019). *COSMO-SkyMed SAR for detection and monitoring of archaeological and cultural heritage sites.* Remote Sensing, 11(11), 1326.

Themistocleous, K., Papoutsa, C., Michaelides, S., Hadjimitsis, D., (2020). *Investigating Detection of Floating Plastic Litter from Space Using Sentinel-2 Imagery*. Remote Sensing, 12(16), 2648.

Thibault Datry, Scott T. Larned, Klement Tockner. (2014). *Intermittent Rivers: A Challenge for Freshwater Ecology*. BioScience, Volume 64, Issue 3, 229–235.

Tomsett, C., & Leyland, J., (2019). *Remote sensing of river corridors: A review of current trends and future directions.* River Research and Applications, 35(7).

Tourenq, C.; Bennetts, R.E.; Kowalski, H.; Vialet, E.; Lucchesi, J.-L.; Kayser, Y.; Isenmann, P. (2001). *Are ricefields a good alternative to natural marshes for waterbird communities in the Camargue, southern France?* Biol. Conserv. 100, 335–343.

Vera-Herrera, L., Soria, J., Pérez, J., & Romo, S. (2021). *Long-Term Hydrological Regime Monitoring of a Mediterranean Agro-Ecological Wetland Using Landsat Imagery: Correlation with the Water Renewal Rate of a Shallow Lake*. Hydrology, 8(4), 172.

Vermote, E.; Justice, C.; Claverie, M.; Franch, B. *Preliminary analysis of the performance of the Landsat 8/OLI land surface reflectance product*. Remote Sens. Environ. 2016, 185, 46–56.

Wan, W., Xiao, P., Feng, X., Li, H., Ma, R., Duan, H., & Zhao, L. (2014). *Monitoring lake changes of Qinghai-Tibetan Plateau over the past 30 years using satellite remote sensing data*. Chinese Science Bulletin, 59(10), 1021-1035.

Wang, Q.; Blackburn, G.A.; Onojeghuo, A.O.; Dash, J.; Zhou, L.; Zhang, Y.; Atkinson, P. (2017). *Fusion of Landsat 8 OLI and Sentinel-2 MSI Data*. IEEE Trans. Geosci. Remote Sens., 55, 3885–3899.

Wang, Z., Liu, J., Li, J., Meng, Y., Pokhrel, Y., & Zhang, H., 2021. *Basin-scale high-resolution extraction of drainage networks using 10-m Sentinel-2 imagery.* Remote Sensing of Environment, 255, 112281.

White, L., Brisco, B., Dabboor, M., Schmitt, A., & Pratt, A. (2015). *A collection of SAR methodologies for monitoring wetlands*. Remote sensing, 7(6), 7615-7645.

White, E.D.; Reed, D.J.; Meselhe, E.A. (2019). *Modeled Sediment Availability, Deposition, and Decadal Land Change in Coastal Louisiana Marshes under Future Relative Sea Level Rise Scenarios.* Wetlands, 39, 1233–1248.

Woodget, A. S., Austrums, R., Maddock, I. P., & Habit, E., 2017. *Drones and digital photogrammetry: from classifications to continuums for monitoring river habitat and hydromorphology.* Wiley Interdisciplinary Reviews: Water, 4(4), e1222.

Wu, M., Zhang, W., Wang, X., & Luo, D. (2009). *Application of MODIS satellite data in monitoring water quality parameters of Chaohu Lake in China*. Environmental monitoring and assessment, 148(1), 255-264.

Xu, H. (2006). *Modification of normalised difference water index (NDWI) to enhance open water features in remotely sensed imagery.* Int. J. Remote Sens., 27, 3025–3033.

Yalin, M. S., (1992). River mechanics, Pergamon Press, Oxford, U.K.

Yang, X.; Liu, Z. (2005). *Using satellite imagery and GIS for land-use and land-cover change mapping in an estuarine watershed.* Int. J. Remote Sens.26, 5275–5296.

Zanchettin, D., Traverso, P., Tomasino, M., (2008). *Po River discharges: a preliminary analysis of a 200-year time series.* Climatic Change, 89(3-4), 411-433.

Acknowledgements

At the end of this Ph.D, I would like to express my deep gratitude to my supervisor Maria Nicolina Papa. She has been my reference point in everything. I could not have imagined having a better mentor for my Ph.D course.

Then I would like to thank the people with whom I have had the opportunity to collaborate in these three years, who have given me the opportunity grow and improve myself professionally. Thank to Massimiliano Gargiulo and Giuseppe Ruello of Department of Information Technology and Electrical Engineering, University of Napoli "Federico II", Napoli, to Guillermo Palau Salvador of INGENIO CSIC-UPV, Universitat Politècnica de València, València, Spain, to Michael Nones of Institute of Geophysics, Polish Academy of Sciences, Warsaw, Poland, and to Paolo Vezza and Giovanni Negro of Department of Environment, Land and Infrastructure Engineering, Polytechnic University of Torino.
I am really grateful to Guillermo Palau Salvador for hosting me at the "Universitat Politècnica de València" and give me to opportunity to join with his research team.

Thanks also to the reviewers of the present dissertation Professor Guido Zolezzi and Professor Pau Miró Martínez for their comments and advises.

All my gratefulness to the most important person of my life, Mamy and Silvio, for their continuous support and infinite patience. Thank you for putting up with my constant anxieties and absences.

I would especially like to thank Professor Paolo Villani, who encouraged me three years ago to undertake my PhD and allowed me to meet and work with Professor Maria Nicolina Papa. Thanks to both of them for always believing in me.

Finally, I would thank the European Space Agency (ESA) and the Italian Space Agency (ASI) for providing the satellite images used in this study.